QUANTITATIVE MEASUREMENTS OF SPIN-TRANSFER-TORQUE-INDUCED DYNAMICS IN NANOMAGNETS

A Dissertation

Presented to the Faculty of the Graduate School

of Cornell University

in Partial Fulfillment of the Requirements for the Degree of

Doctor of Philosophy

by

Lin Xue

August 2013

QUANTITATIVE MEASUREMENTS OF
SPIN-TRANSFER-TORQUE-INDUCED DYNAMICS IN NANOMAGNETS

Lin Xue, Ph.D.
Cornell University 2013

Spin transfer torque is a torque exerted on a magnet by transferring spin angular momentum from a current to the magnet. It enables efficient manipulation of nanomagnets using current and can enable important applications. This dissertation focuses on doing measurements of magnetic dynamics using spin-torque-driven ferromagnetic resonance (ST-FMR), a technique that gives quantitative information about device parameters. This technique not only leads to deeper understanding of spin torque devices but can also provide an improved way to characterize devices for applications.

In a spin torque device such as a magnetic tunnel junction, a microwave current can drive small magnetic oscillations, which yields an oscillating resistance. If a DC current is applied at the same time, an oscillating voltage will be generated by Ohm's Law. The first project in this dissertation makes use of this RF frequency oscillating voltage to perform a quantitative measurement of spin torque and magnetic damping of the device. The second project discusses the possibility of making this voltage larger than the input voltage and thus producing a microwave amplifier.

The same type of magnetic dynamics can be excited using nonlocal spin torque from a pure spin current. In this dissertation, I also discuss how to quantitatively measure the nonlocal spin torque in a 3-terminal device by adapting the DC-detected ST-FMR technique.

Apart from being detected by electrical measurement, the same magnetic dynamics can be directly imaged using X-ray Magnetic Circular Dichroism. I will use a chapter in this dissertation to discuss our progress in doing so and studying magnetic normal modes, the fundamentals of magnetic dynamics.

Last but not the least, in addition to measure conventional metal devices, I will talk about our effort in fabricating and measuring spin torque switching in ferromagnetic semiconductor devices.

BIOGRAPHICAL SKETCH

Lin Xue was born on February 5th, 1985 in Jinan, China. His hometown is a populated city in east China about 4 hours drive south of Beijing. His father worked as a faculty member in Shandong Normal University, and he was raised up in the neighborhood of the university campus. His parents, like many parents in China, considered providing good education to their child as their most important responsibility, and they tried their best in doing that. For example, they chose to live in a smaller apartment than they could get just because the smaller apartment was within walking distance to a very good primary school. Lin also benefited from excellent instructions and generous support from his teachers and mentors through his consecutive 22 years at school.

In his primary and middle schools, Lin was interested in extracurricular mathematics problems. He took part in local competitions and won awards. He went to Shandong Experimental High School, where he became interested and received good training in high school physics. He participated in high school Olympic competitions that won him the direct entrance into college.

Lin attended Nanjing University by the Yangtze River about 4 hours west of Shanghai. He received very good college training in physics by taking well prepared courses by very talented professors and intensive labs. He worked with Prof. Jun Wang and Prof. Wei Wang on simulating biological networks and got exposed to real physics research and techniques including modeling a physical system and data analysis.

In summer 2007, Lin graduated from college and started his graduate school at Cornell University. He continued to pursue his interest in physics at Cornell by working with Prof. Michelle Wang for a semester using optical tweezers to mechanically study the interaction between protein and DNA. Since summer

2008, Lin has been working in Prof. Dan Ralph's group on spin torque devices. He was exposed a variety of techniques to grow magnetic thin films and fabricate nanoscale devices. He developed techniques to quantitatively measure spin torque in different types of devices, which is the main part of the thesis. His experience in the Ralph group led to his career path after graduate school. He will start working on emerging memory technologies as a senior process engineer at Applied Materials in Santa Clara, CA.

To my parents, for their love and support.

ACKNOWLEDGEMENTS

The work presented in this dissertation would not have been possible without the encouragement and support from many people. I would like to take the opportunity to extend my sincere gratitude and appreciation to all those who helped me accomplish this study.

First and foremost, I would like to acknowledge my advisor, Prof. Dan Ralph, for introducing me to this exciting field of physics and for his dedicated advice, inspiration, and continuous support throughout my dissertation research. Dan has set an excellent example as a scientist through his critical thinking, attention to detail, and willingness to communicate. During my years in the Ralph group, I have learnt extensively from him, not only how to design an experiment and analyze data, but also ways to present results at conferences and in publications. I enjoyed working in the group because Dan gave us students freedom to choose and manage our own projects and treated each one of us as an independent researcher. Dan's easy going personality and sense of humor made the time spent with him a great joy.

I would like to thank Prof. Bob Buhrman for his helpful discussions and suggestions to my work presented here. The collaboration with Buhrman group has been an incredible resource for my research. I am also very grateful to Bob's support for my job applications and spending time with me on career advice. His experience and ardent to science opened my eyes and help shape me as a researcher.

I would like to acknowledge Prof. Erich Mueller for serving in my committee, and for his helpful discussion in the modeling of my work on the three-terminal device. I would like to thank Prof. Michelle Wang for providing me the opportunity in her lab during my first semester at Cornell. The training and

experience I got from working with her will benefit me through my career. I also would like to acknowledge the help from other professors at Cornell, including Albert Sievers, Chris Henley, Greg Fuchs, Jeevak Parpia, and Ritchie Patterson.

I want to thank all my labmates in the Ralph group and the Buhrman group, especially those who worked closely with me on spin torque projects. They are Kiran Thadani, Yongtao Cui, Chen Wang, Luqiao Liu, Oukjae Lee, and Takahiro Moriyama. Kiran taught me the nanopillar fabrication process when I joined the group. Her passion and focus on work impressed me along with her sense of humor. Yongtao was one of the labmates that I spent the most time with. He helped me with trouble shooting the problems in my fabrication and measurements. We worked together on the x-ray project in Berkeley Lab that involved lots of travels to the west coast and long hours at the beamline. I also enjoyed the time with Yongtao outside of the lab when we went for photo shooting. Chen showed me the tricks in the measurements, and he was always eager to discuss with me about my projects. I appreciate his help and contribution to many of projects discussed in this dissertation. Luqiao knew a lot about device design and fabrication, and he helped me a lot with my projects on fabrication and modeling. I worked with Oukjae on maintaining the ion-beam deposition tool for a few years. I enjoyed working and listening Korean popular songs with him. I spent lots of time in the lab with Taka, and we travelled together to conferences. I appreciate his help on my research and on my job search.

I also would like to thank Sufei Shi, Wan Li, Eugenia Tam, Josh Parks, Ted Gudmundsen and Alex Mellnik for their help and support. I often call Sufei 'Big Brother', and indeed he knows everything and would like to offer help. Wan came in Cornell in the same year as me. She is very kind and willing to take care of people. When I had difficulties, she always encouraged me and tried to help

me out. I had a good time studying and working with her in the past six years, and I wish her good luck for her future career. I enjoyed sharing office with Eugenia, Josh and Ted over the years, and I still remember our happy conversations and get-togethers. I enjoyed working with Alex and having interesting discussion with him about shooting pictures.

I would like to thank other members in the Cornell groups for their help and support. They are Colin Heikes, Jen Grab, Dave MacNeill, Greg Stiehl, Colin Jermain, Saikat Ghosh, Jonathan Gibbons, Neal Reynolds, Peter Mintun, Zach Anderson, Hsin-wei Tseng, Yun Li, Praveen Gowtham, Junbo Park, Chi-feng Pai, Pinshane Huang, Luis Leão, Graham Rowlands, Yongxi Ou, Vlad Pribiag, John Read, and Pat Braganca.

I want to give my thanks to my collaborators outside of Cornell. They are Jordan Katine, Jonathan Sun, Prof. Nitin Samarth, Dave Rench, Mark Wilson, Partha Mitra, Giovanni Finocchio, Mario Carpentieri, Peter Fischer, Mi-Young Im, and Tolek Tyliszczak.

I would like to acknowledge the support from the CNF staff members on process design and development for some of the devices I studied, including Noah Clay, Alan Bleier, and Rob Ilic. I also would like to thank Jon Shu and Steve Kriske for their support of CNS/CCMR equipment, and Nathan Ellis for teaching me to use the machine shop. The research centers at Cornell provided me access to excellent facilities and benefited my research.

I would like to give my thanks to my friends at Cornell, who accompanied me through the cold winters and sunny summers: Xin Shi, Jing Jin, Zhipan Li, Bo Xiang, Yang Xie, Yao Weng, Joanna Tan, Yi Jiang, Qingyun Mao, Huolin Xin, Heng Li, Yong Chen, Yi Xie, Yang Zhang, Xiaodong Xu, Meng Wang, Qi Wang, Hao Shen, and Lu Huang. I also enjoyed my time with my friends at

the Cornell Chinese Students and Scholar Association and Cornell Photo Club. I also have many other friends inside and outside of Cornell that I could not mention within the limit of the acknowledgement. I appreciate them all for their help and support.

Last but not the least, I would like to thank my family for raising me and supporting my work at Cornell.

TABLE OF CONTENTS

LIST OF TABLES

LIST OF FIGURES

CHAPTER 1

INTRODUCTION

1.1 Spin Transfer Torque

Spintronics research explores the interplay between the spin and charge of electrons in solid-state devices, which can improve efficiency and add new functionalities for electronic devices with memory and logic applications. It not only leads to important technological applications, but also opens a new field to study quantum physics and related new materials.

Spintronics covers a broad range of research from single localized spins to spin transport in devices at the mesoscopic scale. In this dissertation, I would like to focus on the spin transfer torque (or spin torque for short) effect in spin transport devices. It describes the interaction between spin currents and magnetic moments, no matter whether the spin current is generated by spin filtering[1], spin-orbital coupling[2], or thermal gradients[3].

In this chapter, I will briefly introduce the research progress on spin transfer torque, including the fundamental physics, application, and characterization of spin transfer torque. I will also mention some recent discoveries about spin torque devices that are of both scientific and technological interest.

1.1.1 Giant Magnetoresistance Effect and Tunneling Magnetoresistance Effect

The Giant Magnetoresistance (GMR) effect comes from the concept of spin filtering. Spin filtering is observed when a current flows through a magnetic layer. Here we use a simple physical picture to understand it. If the spin of an electron is parallel to the magnetization of that layer, it experiences a small scattering through the layer. If the spin is antiparallel to the magnetization, it experiences a large scattering through the layer, and it is likely to be reflected back (Figure 1.1 (a)).

In magnetic multilayers, due to spin filtering, when the magnetizations of the neighboring magnetic layers are parallel, the resistance is at its minimum (R_{P}); when they are antiparallel, the resistance is at its maximum (R_{AP}). This is the GMR effect [4, 5] (Figure 1.1 (b)). A GMR spin valve device consists of two ferromagnets separated by a normal metal spacer. Its magnetoresistance (MR) ratio

$$MR = \frac{R_{\mathrm{AP}} - R_{\mathrm{P}}}{R_{\mathrm{P}}} \times 100\%, \tag{1.1}$$

is typically a few 10's of percent. The 2007 Nobel physics prize was awarded to Albert Fert and Peter Grünberg for the discovery of this effect [6] that now led to the first widely used spintronic device in industry, the GMR read head in hard disk drives.

If the spacer in the spin valve is replaced by a thin insulator as a tunnel barrier, the device becomes a magnetic tunnel junction (MTJ). The counterpart to GMR in a MTJ is the Tunnel Magnetoresistance (TMR) effect, which is a quantum mechanical phenomenon. The MR ratio of a TMR device can be in the range

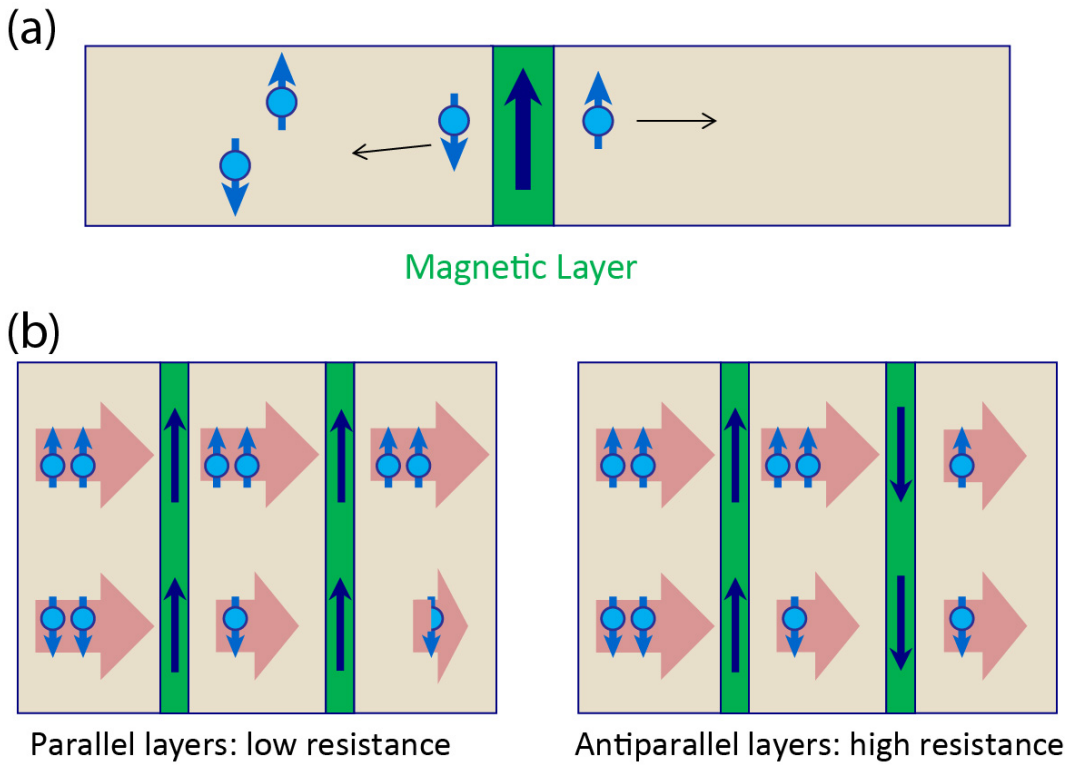

Figure 1.1: GMR effect: a simple picture. (a) Spin filtering effect. (b) GMR effect.

of a few tens to hundreds of percent. The recent development of MTJs with a MgO tunnel barrier [7–9] significantly enhanced the TMR ratio. MTJ devices have been adopted for the current read head technology in hard drives.

The origins of the GMR and TMR effects come from the density of states near the Fermi level of the ferromagnetic metal, where due to the energy splitting of the 3d band, spin up has more filled states than spin down, while near the Fermi surface, spin up has smaller density of states than spin down (Figure 1.2 (a)). The electron transport in those devices can be divided into spin up and spin down channels. For spin valves, it can be solved using the Valet-Fert model [11] with an effective circuit picture (Figure 1.2 (b)). For a MTJ, the tunnel conductance dominates the conductance of the device (Figure 1.2 (c)). The TMR can

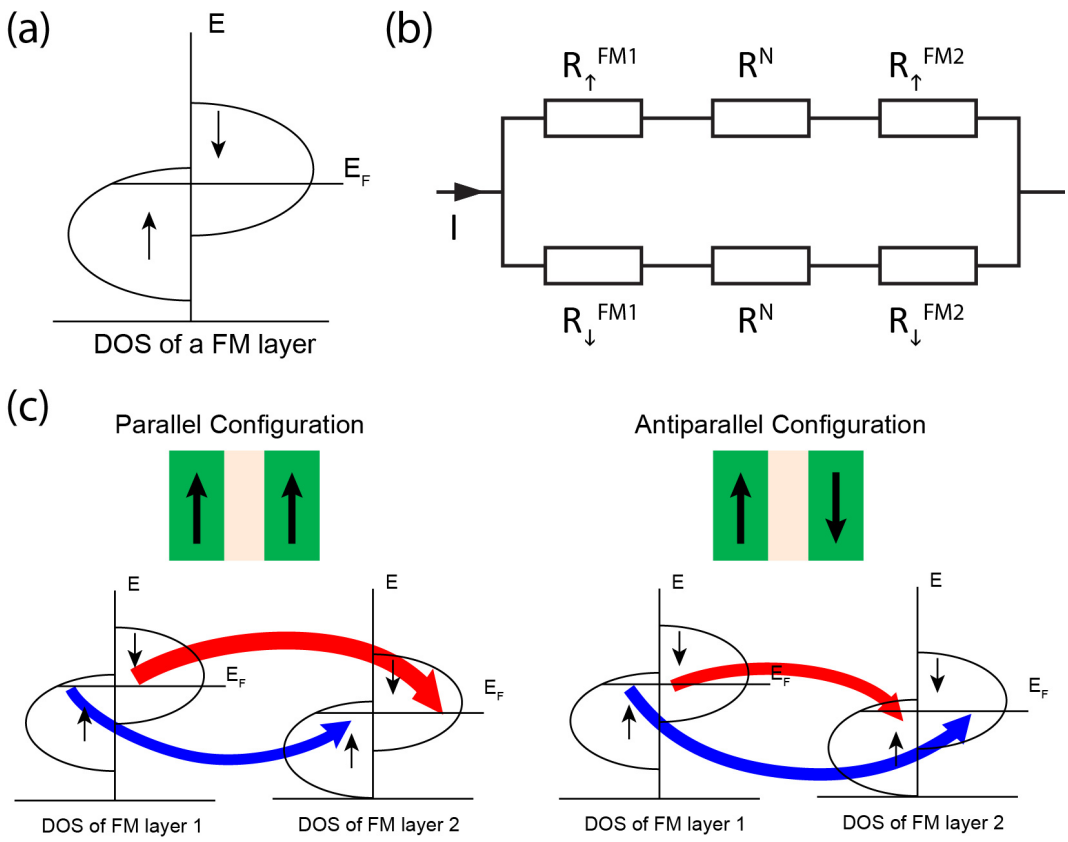

Figure 1.2: Origin of the GMR and TMR effects. (a) Density of states (DOS) near the Fermi level for spin up (↑) and spin down (↓) in a ferromagnetic (FM) layer. (b) Effective circuit for a spin valve device with two ferromagnetic layers. $R_{\uparrow}^{\mathrm{FM1}}$, $R_{\downarrow}^{\mathrm{FM1}}$, $R_{\uparrow}^{\mathrm{FM2}}$, $R_{\downarrow}^{\mathrm{FM2}}$ and R^{N} are the spin-dependent resistances for ferromagnetic layer 1 (FM1), ferromagnetic layer 2 (FM2), and the normal metal spacer N. (C) Spin dependent tunneling across the barrier in a TMR device. Modified from Reference [10].

be understood qualitatively using the simple Jullière model [12]. For a certain spin channel combination, the tunnel conductance is proportional to the density of states of the spin channel on both sides of the tunnel barrier. Thus, the magnetization orientations of the ferromagnetic electrodes have a larger effect on the MR, which makes the TMR typically much larger than the GMR.

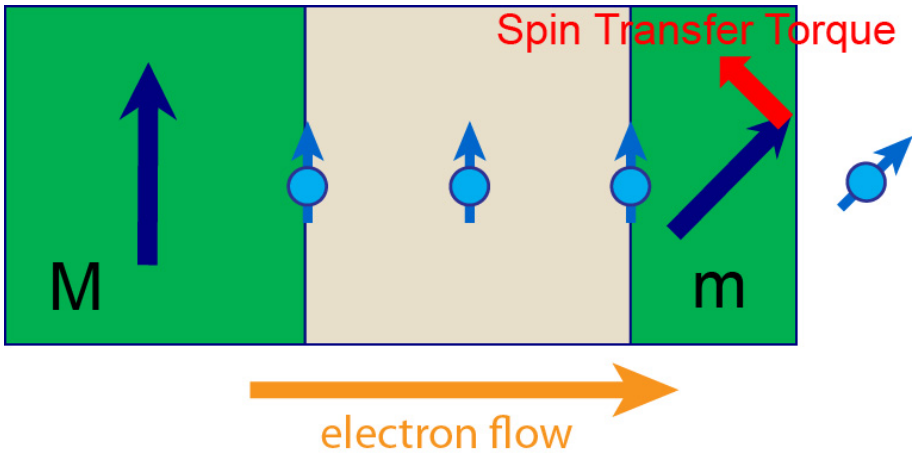

Figure 1.3: Spin transfer torque. The current becomes spin polarized when passing through the fixed layer with magnetization $\vec{M}$. Spin polarized current exerts the spin torque on the free layer to make it precess. Each blue circle with an arrow stands for an electron, and the arrow shows the spin orientation of the electron.

1.1.2 Spin Transfer Torque Effects

Spin transfer torque is the reverse effect of the spin filtering effect, where instead of the magnet acting on the current, the current is exerting a torque on the magnet. As shown in Figure 1.3, the magnetic film has two ferromagnetic layers, the thick fixed layer with magnetization $\vec{M}$ and the thin free layer with magnetization $\vec{m}$. The current first becomes spin polarized when it goes through the fixed layer. Then the spin polarized current exerts the spin torque on the free layer to make it precess.[13–15] The precession driven by spin torque can be described by the Landau-Lifshitz-Gilbert-Slonczewski (LLGS) equation eq. (1.2) (Figure 1.4).

$$\frac{d\hat{m}}{dt} = -\gamma \hat{m} \times \vec{H}_{\text{eff}} + \alpha \hat{m} \times \frac{d\hat{m}}{dt} + \gamma \vec{\tau}. \tag{1.2}$$

Here γ is the absolute value of the gyromagnetic ratio; $\vec{H}_{\text{eff}}$ is the effective field acting on the free layer including the applied, demagnetization [16], and ex-

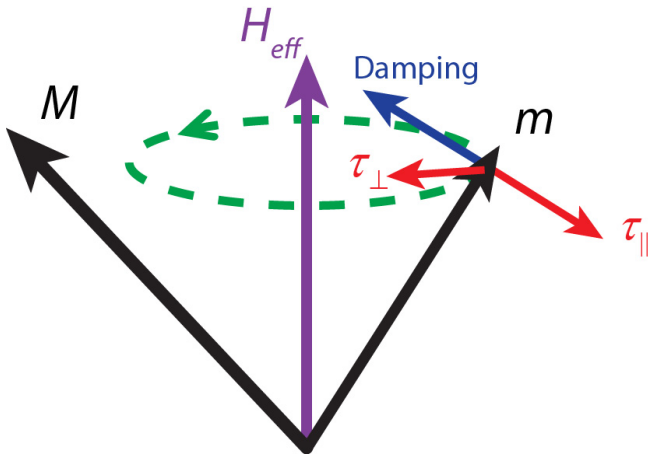

Figure 1.4: Directions of spin transfer torque and magnetic damping torque in a MTJ device as described in the LLGS equation.

change fields; α is the Gilbert damping parameter; τ is the spin torque. The first term on the right-hand side of the equation is the precession term, the second term is the damping term, and the third term is the spin torque term. For a spin valve, the spin torque lies in the sample plane and orthogonal to the magnetization. For a MTJ, the spin torque has both in-plane and perpendicular components (Figure 1.4).

Spin torque enables the manipulation of nanomagnets using current. As shown in Figure 1.4, spin torque can drive magnetic precession of the free layer. For in-plane magnetized samples, the precession is strongly elliptical due to the large demagnetization field. If the spin torque is large enough, it can either switch the magnetization (Figure 1.5 (a)) or drive it into large angle precession (Figure 1.5 (b)) depending on the magnetic configuration and applied field. I will talk about the applications arising from both types of dynamics.

The threshold for a spin torque excitation is determined by the current density through the cross section of the device ($\propto I/r^2$), while the one for a Oersted

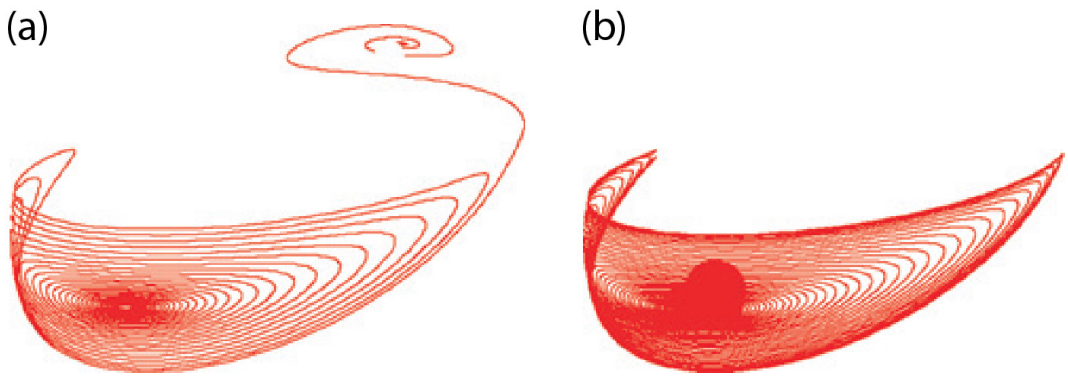

Figure 1.5: Spin torque manipulation of nanomagnets. The figure shows trajectories of the magnetization vector in spin-torque-driven dynamics for (a) magnetic switching. (b) magnetic precession. Adapted from Reference [15].

field induced reorientation is approximately determined by the current divided by the radius of the cross section ($\propto I/r$). In order to make a good use of the spin torque, the devices have to be made below 250 nm in diameter, in which range the spin torque is a stronger effect than the Oersted field. The typical critical current density for spin torque magnetic switching is 10^6 – 10^7 A/cm^2.

1.2 New Types of Spin Torque and Device Features

1.2.1 Spin Hall Effect

The spin Hall effect is the generation of opposite spin accumulations on the lateral surfaces of an applied charge current [17, 18] (Figure 1.6). The directions of the charge current, spin current, and the spin polarization of the spin current are all orthogonal to each other. The spin Hall effect comes from spin-orbital coupling. The mechanism of the spin-orbital coupling can be explained by either intrinsic band structure theory [19] or extrinsic scattering theory [20].

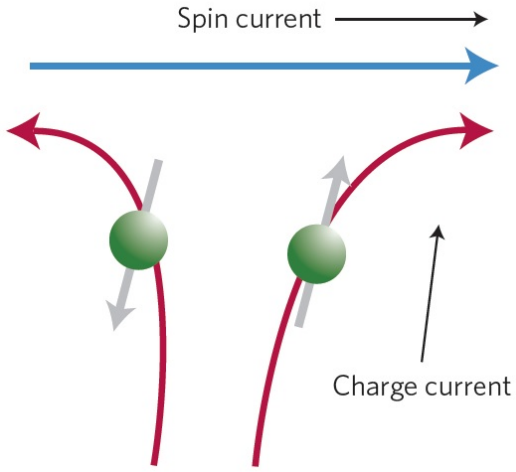

Figure 1.6: Spin Hall effect. A charge current composed of electrons with up and down spins flows through a spin Hall metal. Due to the spin-orbital coupling interactions, electrons with opposite spins are scattered in opposite directions forming a spin current perpendicular to the charge current. Then opposite spin accumulations are built up on the lateral surfaces of the charge current. Adapted from Reference [17].

The strength of the spin Hall effect can be parameterized by the spin Hall angle, defined as the ratio of the spin current density to the applied charge current density $\theta_{SH} = J_s/J_e$. Large spin Hall angle values are found in heavy metals (Pt: 0.07 [21], Ta: 0.12-0.15 [22], W: 0.3 [23]) and alloys (CuBi: 0.24 [24]).

The spin Hall effect can be used to apply spin torque to an adjacent magnet (Figure 1.7 (a)). That torque is often called spin Hall torque, and it can also switch the magnetization (Figure 1.7 (b)) or drive magnetic precession [25]. Novel spintronics devices can be made using spin Hall torque that may have interesting applications.

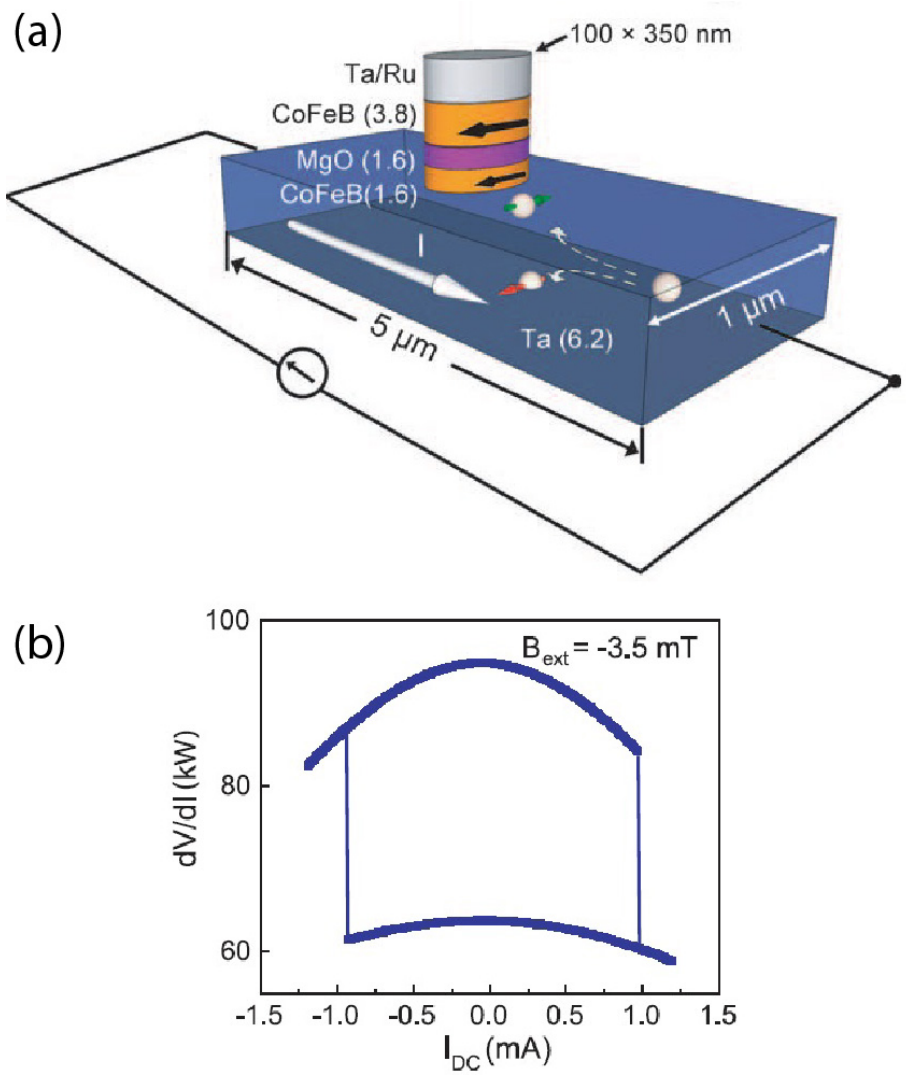

Figure 1.7: Spin Hall torque switching. (a) A three-terminal device designed for spin Hall torque switching. The three terminals are for contacting the two ends of the spin Hall metal and the top of the MTJ. The charge current flows laterally through the spin Hall metal. It generates a spin current that applies a spin Hall torque on the free layer of the MTJ. The resistance is measured between the top of the MTJ and one end of the spin Hall metal. (b) Differential resistance measurement when scanning DC current through the spin Hall metal layer showing clear magnetic switching. Adapted from Reference [22].

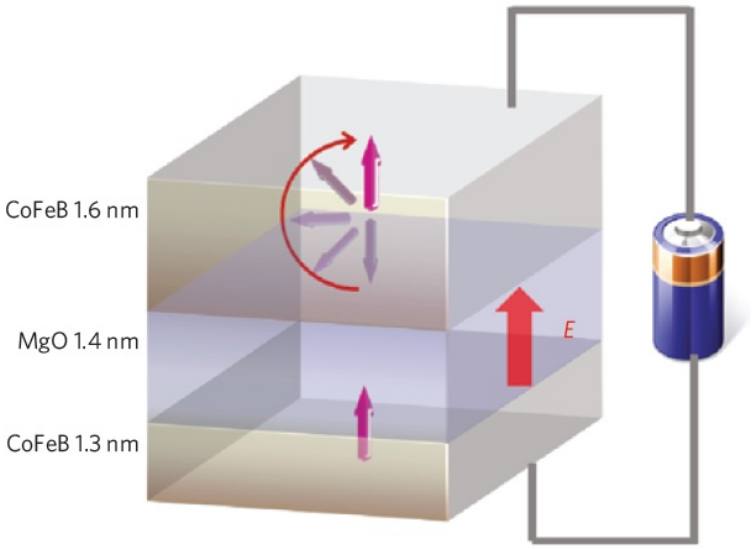

Figure 1.8: Magnetic switching induced by voltage controlled magnetic anisotropy. Adapted from Reference [26].

1.2.2 Voltage Controlled Magnetic Anisotropy

A voltage applied across an insulator in contact with a magnet, which produces an electrical field at the insulator/magnet interface, can change the anisotropy of the magnet. This is called voltage controlled magnetic anisotropy (VCMA). It was first discovered in ferromagnetic semiconductors [27] and multiferroic materials [28], and electrical field induced magnetic switching has been achieved. More recently VCMA at the CoFeB/MgO interface of a MTJ was discovered [26, 29] (Figure 1.8), which directly incorporates VCMA with spin torque devices such as a MTJ.

VCMA at the CoFeB/MgO interface maybe be explained by the change in the relative occupancy of the 3d-orbitals of Fe atoms at the interface [28]. The current density for magnetic switching using VCMA can be as low as 1.2×10^2 A/cm^2 [26] compared with $10^6 - 10^7$ A/cm^2 for spin torque switching [30]. It

might enable more efficient electrical control of magnetic devices.

1.2.3 Spin Caloritronics

Spin caloritronics studies the interaction of spins with heat currents [33]. For example, Figure 1.9 (a) shows thermal spin injection (spin-dependent Seebeck effect) achieved by flowing a heat current from the injector magnet and detecting the spin accumulation with a small magnetic detector. Figure 1.9 (b) shows a reverse effect of (a). A heat current is induced by injecting a spin accumulation into a ferromagnet, which is called spin-dependent Peltier effect. The spin Seebeck effect (Figure 1.10) is the generation of spin voltage from a metallic magnet in a temperature gradient [34].

Spin caloritronics research might lead to the development of spin based heat engines, motors, heaters, and coolers. However, so far the effects are small and will need future material and device engineering to improve the device performance [32].

1.3 Applications of Spin Torque Devices

1.3.1 Spin Transfer Torque Magnetic Random Access Memory

The application of Magnetic Random Access Memory (MRAM) uses a magnetic tunnel junction (MTJ) as a memory cell, and the low and high resistance states of the MTJ record the bit information ”1” and ”0”. It is a non-volatile memory

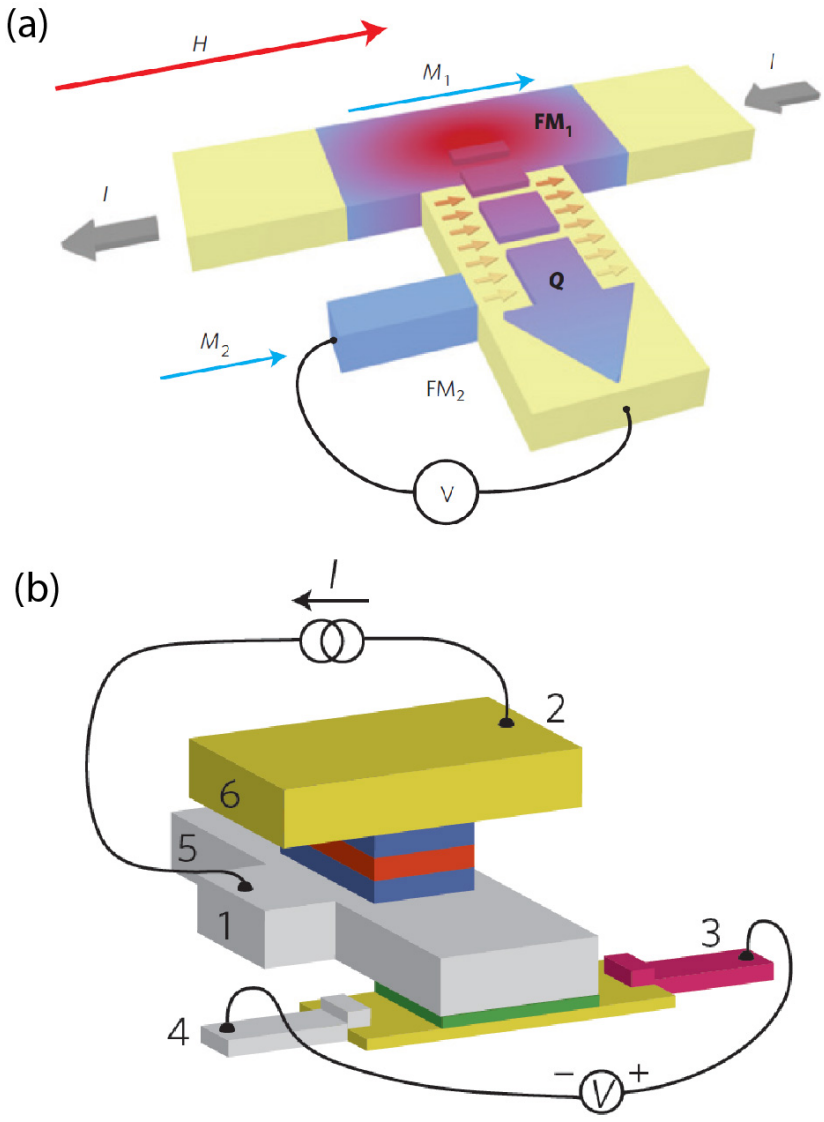

Figure 1.9: Spin-dependent Seebeck effect and Peltier effect. (a) Spin-dependent Seebeck effect. A charge current I flows through the ferromagnet, FM1, and heats it up. The normal metal contacts (yellow) are highly thermally conductive and act as heat sinks. The heat current Q inject spins into the normal metal and build up spin accumulation there. The spin accumulation is detected by measuring the voltage V on the ferromagnetic detector, FM2. Magnetic field H is used to manipulate the magnetizations of FM1 and FM2, M_1 and M_2. Adapted from Reference [31]. (b) Spin-dependent Peltier effect. Current I is sent through contacts 1 and 2 to inject spin accumulation into the bottom ferromagnet (blue). The spin-dependent Peltier signal is detected by measuring the voltage V between contacts 3 and 4 across the thermocouple. Adapted from Reference [32].

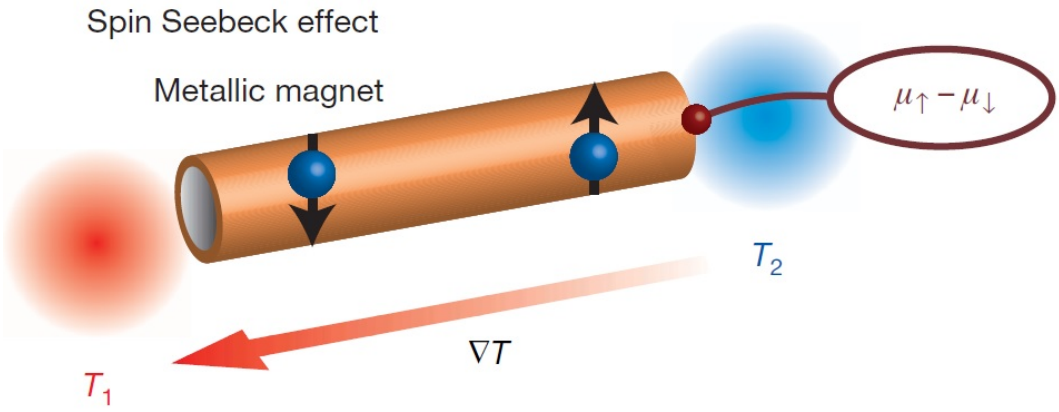

Figure 1.10: Spin Seebeck effect. In a metallic magnet, spin up and spin down conduction electrons have different Seebeck coefficients. If the magnet is placed in a temperature gradient, spin up and spin down will have different accumulations resulting in a spin voltage $\mu_\uparrow - \mu_\downarrow$. Adapted from Reference [34].

technology that has the potential to replace SRAM, DRAM and NAND and become the "universal memory" [36]. The first generation of MRAM employs the Oersted field from an additional wire to write the information on a MTJ (Figure 1.11 (a)).[37] However, the involvement of the write wire makes the MRAM cell difficult to scale down. Spin transfer torque switching of the magnetic free layer makes it possible to write the MRAM bit directly with current. Spin transfer torque MRAM (STT-MRAM) greatly simplifies the memory bit structure and makes it scalable to future technology nodes (Figure 1.11 (b)).[35, 38]

The magnetic part of the memory cell for STT-MRAM is a MTJ. Compared with other prototypical memory technologies, STT-MRAM has the advantage of long endurance and high write speed and a good potential to scale down to sub 10 nm scale.[39]

The magnetic layers of the MTJ were originally magnetized in-plane (Figure 1.12 (a)). In this case, the shape anisotropy of the free layer with an elliptical cross section keeps its magnetization in one of the directions along the long

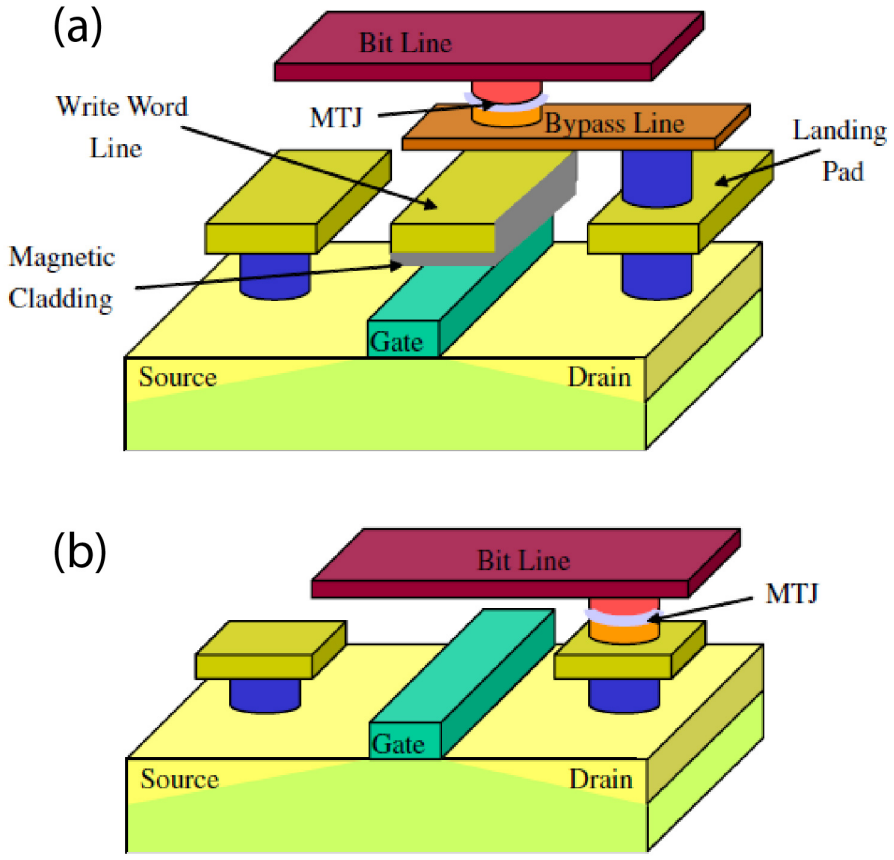

Figure 1.11: Memory cell architectures for two generations of MRAMs. (a) Field switched MRAM. The writing of the memory cell is achieved by flowing currents through both the bit line and the write word line, which allows the selection of the memory cell at the cross point of the two lines. The reading of the memory cell is done by flowing a small current through and measuring the voltage across the MTJ. (b) STT-MRAM. STT-MRAM uses a large current through the MTJ to write the memory cell by spin torque switching. The reading mechanism is the same as the field switched MRAM. Adapted from Reference [35].

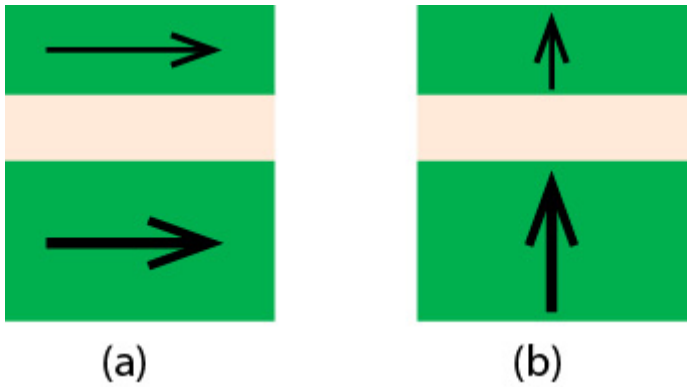

Figure 1.12: Magnetic configurations of STT-MRAM cells. (a) In-plane magnetized configuration. (b) Out-of-plane magnetized configuration using PMA.

axis. However, as the size of the device scales down, it is difficult to maintain a good cross-sectional aspect ratio. Instead, perpendicular magnetic anisotropy (PMA) will likely be used to pin the magnetization out of plane (1.12 (b))), so that a well controlled elliptical cross section is no longer needed. To make PMA for MTJs, people have tried Co/Pt multilayers[40], $L1_0$-FePt[41], and CoFeB-MgO[30]. More complicated designs of the MTJ are also being developed to pursue improved device performance. For example, the addition of a orthogonal polarizer can provide a large spin torque at the beginning of switching process [42]. A three-terminal device structure uses a spin valve for the writing and protects the MTJ from degrading [43].

To increase the area density of devices to replace DRAM, MTJs have to be made smaller than 30 nm while maintaining good switching performance. This is a major challenge in developing STT-MRAM products. The energy barrier between the two stable states has a lower limit in order for a good data retention, which requires a certain amount of the switching current, while the available current from a transistor reduces linearly with the gate width [44]. The magnetic properties such as magnetic damping may also be affected. As the device size

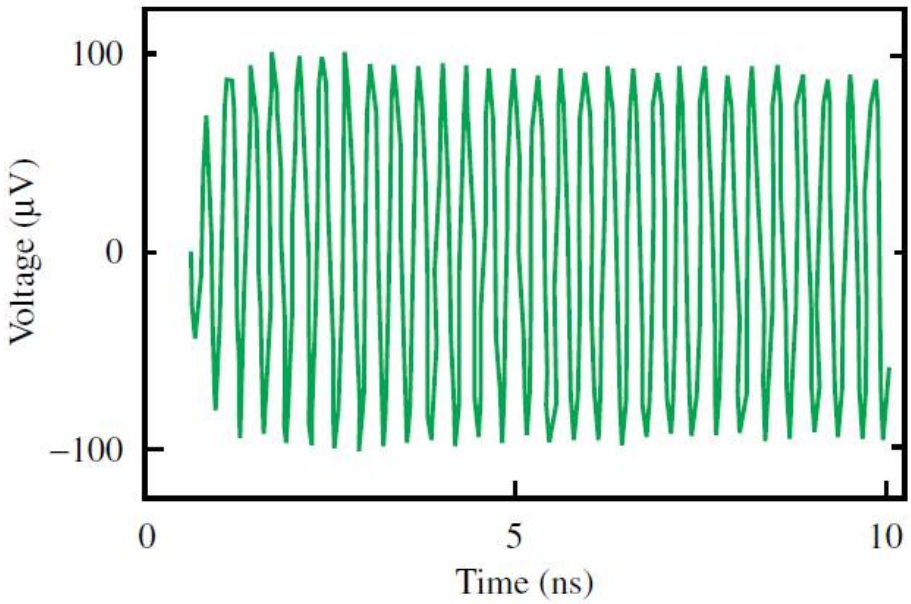

Figure 1.13: Microwave oscillation driven by a DC current in a spin valve. Adapted from Reference [45].

shrinks, the aspect ratio increases, and more atoms are along the side wall of the MTJ pillar that are susceptible to etching damage and non-uniform local field, which may effect the magnetic properties.

1.3.2 Microwave Oscillators

As discussed in earlier sections, spin torque can drive a magnet to precess persistently, which produces an oscillating resistance at GHz frequencies. By Ohm's law, the oscillating resistance in the presence of a DC current produces a microwave voltage (Figure 1.13) [45–47]. In addition to single domain type of devices such as a spin valve or a MTJ, magnetic vortex devices can also generate microwave oscillations [48, 49].

Spin torque oscillators have good frequency tunability in about the 1-20 GHz

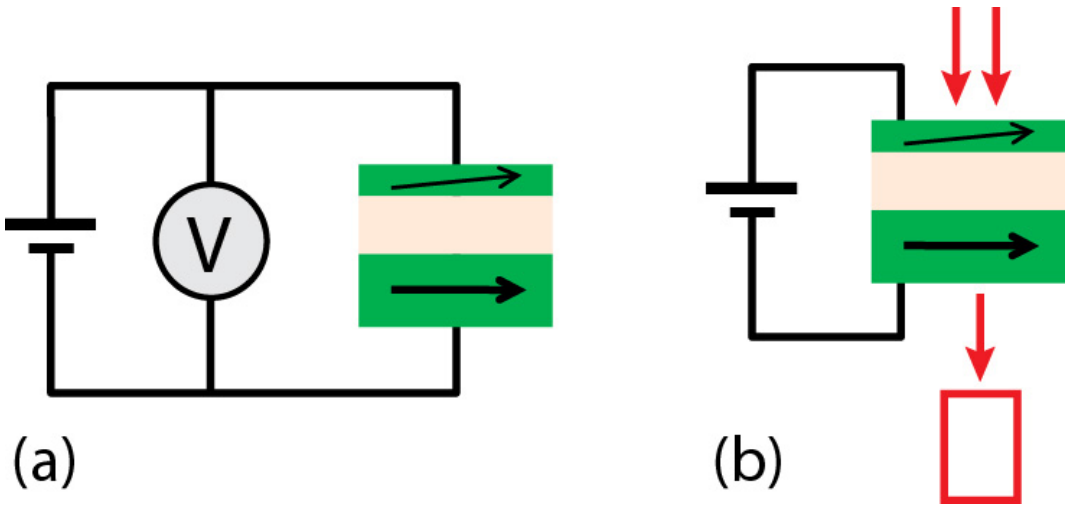

Figure 1.14: Methods to characterize spin torque devices. Magnetic dynamics is excited by spin torque and detected using (a) electrical testing or (b) optical/x-ray imaging.

range, but their linewidths in the microwave spectrum are large, and their emitted power is low. The linewidth and power can be improved by making use of the local dipole field to synchronize different parts of the same device [48] or spin waves to couple a few devices to produce coherent oscillations [49, 50].

Spin torque driven microwave oscillators can not only serve as microwave sources, but also as a magnetic field detectors at the nanoscale. For example, they might be applied to make the read head sensor in hard drives [51].

1.4 Characterization of Spin Torque Devices

Since spin torque devices have interesting applications, it is important to characterize those devices to understand the device physics and make good use of them. The major methods are electrical testing and optical/x-ray imaging. There is also some effort using magnetic force measurement.[52]

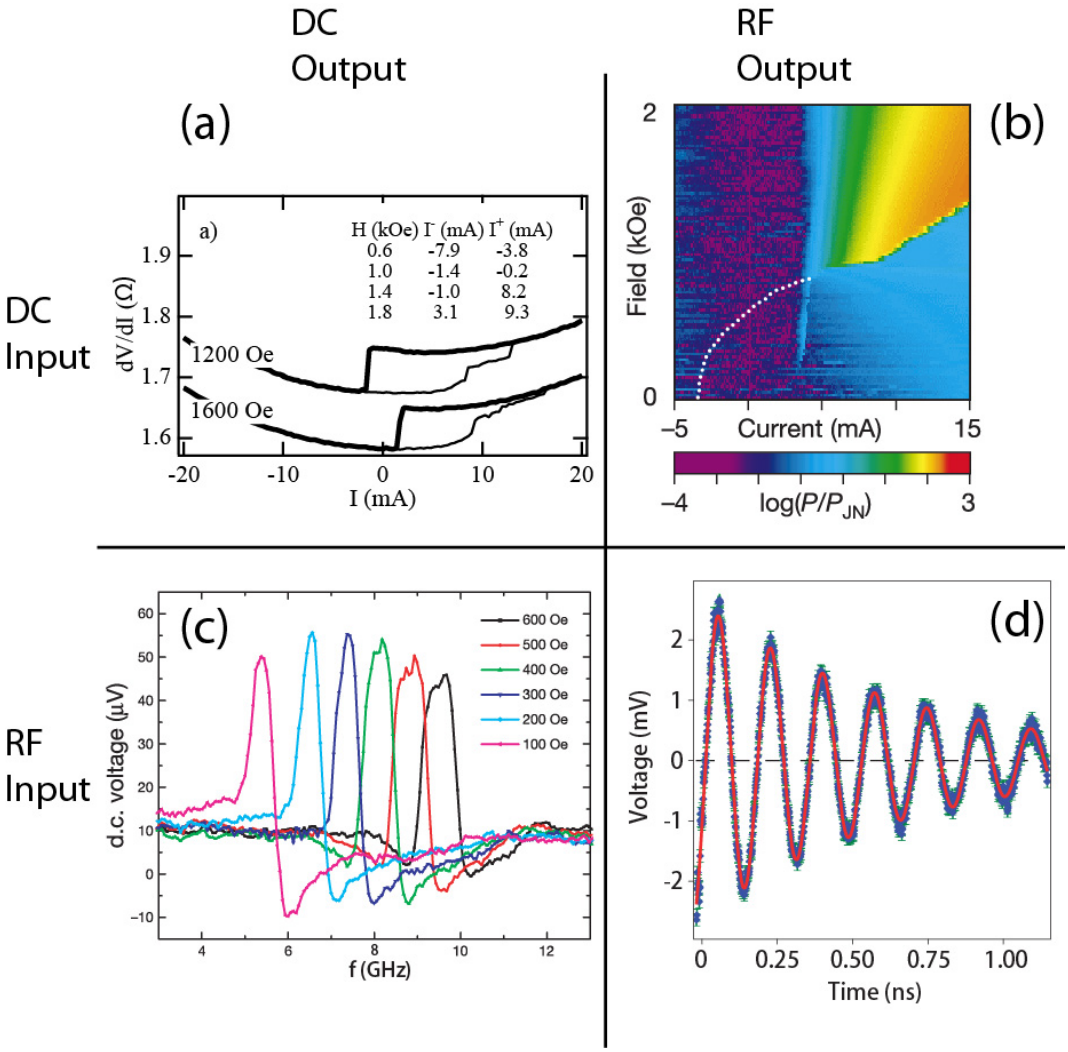

Figure 1.15: Electrical test of spin torque devices. (a) Current induced magnetic switching in a spin valve device. Adapted from Reference [53]. (b) Microwave oscillation driven by a DC current in a spin valve device. Adapted from Reference [46]. (c) Spin torque ferromagnetic resonance (ST-FMR) in a MTJ device. Adapted from Reference [54]. (d) Time-resolved ST-FMR in a MTJ device. Adapted from Reference [55].

1.4.1 Electrical Testing

The most common way to characterize spin torque devices is electrical testing, as shown in Figure 1.14 (a). An electrical current is sent into the device to exert a spin torque on the free layer of the device, and electrical signals originating from the magnetoresistance effect are detected. Electrical testing can be summarized with four categories of measurements in terms of the frequency of the input and output signals as shown in Figure 1.15. With a DC input and a DC output (Figure 1.15 (a)), people have been doing DC current scans while measuring the resistance, in order to study the current induced switching of the device.[53, 56] With a DC input and a RF output (Figure 1.15 (b)), the DC current and the external field are set to a regime where the current drives persistent magnetic dynamics. The oscillating resistance and the DC current produce a RF voltage output, which will help us undertand the persistent magnetic dynamics.[46, 57] With a RF input and a DC output (Figure 1.15 (c)), the RF current will drive the magnetization to do small angle oscillation and produce an oscillating resistance. This resistance mixes with the RF input current and produces a DC component in the output signal to be measured. This is the type of measurement named spin torque ferromagnetic resonance (ST-FMR). It can provide information including the strength of the spin torque and the magnetic damping of the device.[54, 58] With a RF input and a RF output (Figure 1.15 (d)), small magnetic oscillation is driven by the RF input and produce an oscillating resistance. If a DC current is also applied, by Ohm's Law, a RF voltage can be produced and transmitted out of the device. By measuring that RF output, an time-resolved version of ST-FMR can be made.[55]

Although the electrical testing has been developed since the first generation

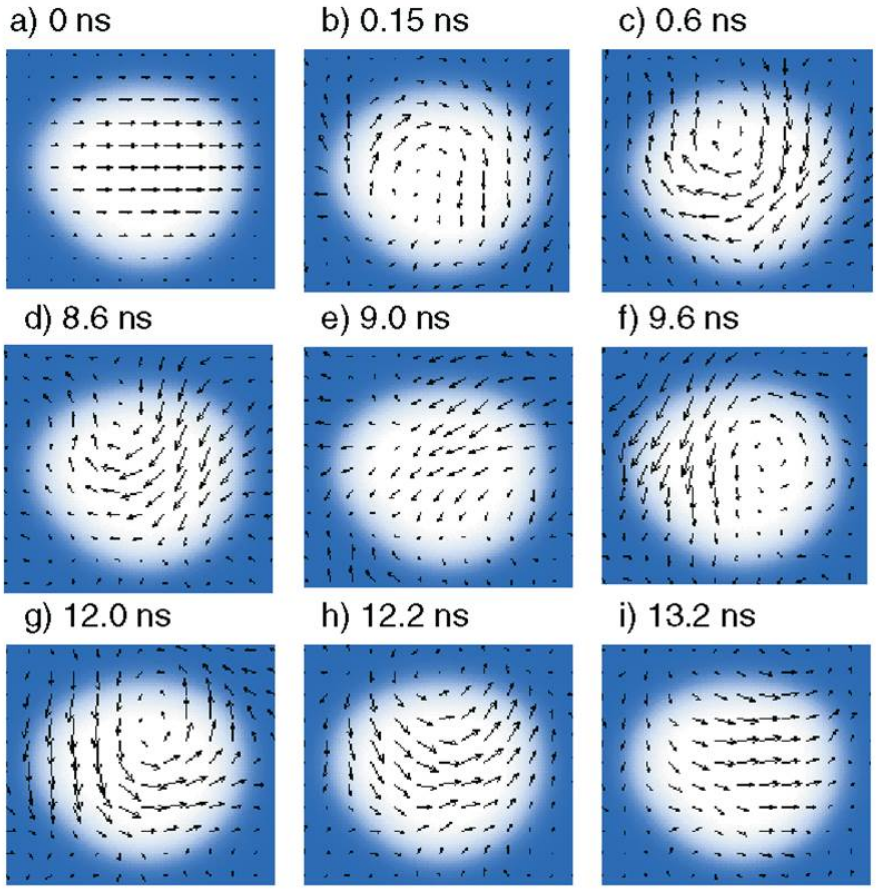

Figure 1.16: X-ray imaging of the DC-pulse-driven magnetic switching in a spin valve device. The panels show evolution of the magnetization during the pulse sequence for spin torque switching. The magnetization is interpreted from the x-ray transmission data. Adapted from Reference [59].

of spin torque devices, making quantitative measurements of the spin torque as a function of bias and doing it in an efficient way remain challenging. I will address those challenges and talk about work on the last two categories of measurement (RF in DC out, RF in RF out) in detail in the following chapters.

1.4.2 Optical/X-Ray Imaging

An additional way to characterize spin torque devices is to make use of the interaction between light and the magnetic element and directly image the magnetic dynamics with spatial and time resolution (Figure 1.14 (b)). The Magneto-Optical Kerr effect (MOKE) can be used to image domain-wall motion driven by the spin torque from a current flowing laterally.[60] For nanopillar devices, X-ray Magnetic Circular Dichroism can be used to image the magnetic dynamics driven by a current perpendicular to plane (Figure 1.16).[59] Since x-rays have a short wavelength, and high penetration through materials, they provide high spatial resolution, and they are able to image layers through the sample thickness.

Magnetic dynamics driven by DC pulses has been imaged using those methods. However, in order to understand the magnetic dynamics better, individual dynamical modes have to be identified and studied. I will discuss the work following that line in a following chapter.

CHAPTER 2

NETWORK ANALYZER MEASUREMENTS OF SPIN TRANSFER TORQUES IN MAGNETIC TUNNEL JUNCTIONS

In this chapter, we first review the methods to quantitatively measure spin transfer torque. We then focus on demonstrating a simple network-analyzer technique to make quantitative measurements of the bias dependence of spin torque in a magnetic tunnel junction. We apply a microwave current to exert an oscillating spin torque near the ferromagnetic resonance frequency of the tunnel junctions free layer. This produces an oscillating resistance that, together with an applied direct current, generates a microwave signal that we measure with the network analyzer. An analysis of the resonant response yields the strength and direction of the spin torque at non-zero bias. We compare to measurements of the spin torque vector by time-domain spin-torque ferromagnetic resonance. The work discussed in this chapter was published in Reference [61].

2.1 Review of the Methods to Quantitatively Measure Spin Transfer Torque

Spin transfer torque provides the possibility of efficiently manipulating the magnetic moment in a nanoscale magnetic device using applied current.[13–15] Understanding the strength of the spin torque, and particularly its bias dependence, is important for applications that include spin torque magnetic random access memory and frequency-tunable microwave oscillators.[35] Several different techniques have been developed to measure the voltage bias dependence of the spin torque vector in magnetic tunnel junctions (MTJs), with results that

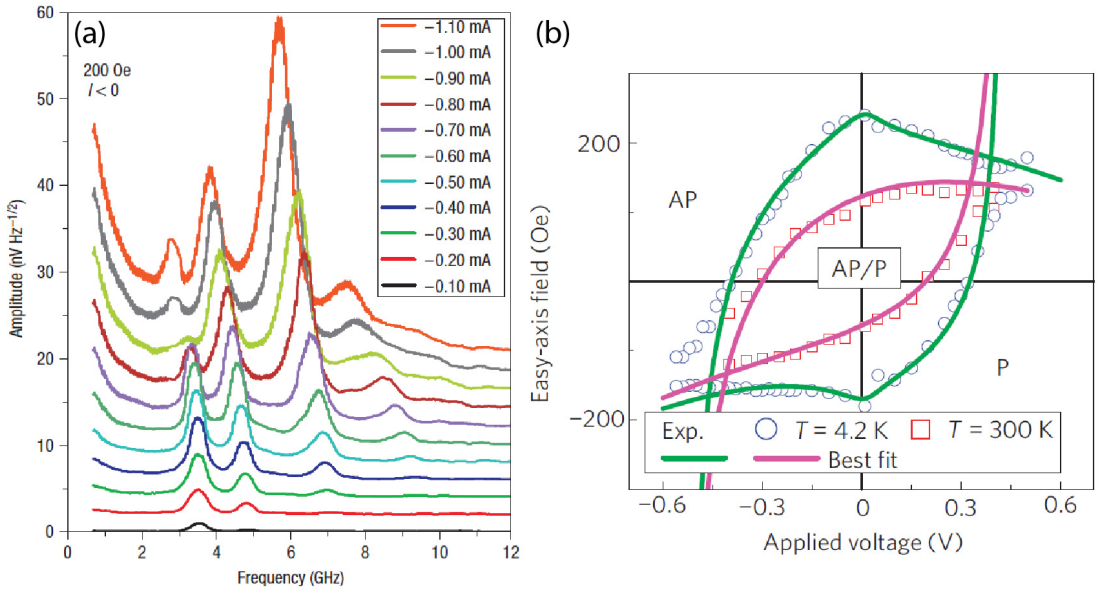

Figure 2.1: Previous methods to measure spin torque. (a) Thermal FMR measurement. Magnetic dynamics is excited thermally, and microwave spectra are measured across a range of frequencies. Adapted from Reference [57]. (b) Fits to switching phase diagram. Adapted from Reference [62].

in some cases are inconsistent with each other. These include measurements of the bias dependence of the magnetic precession frequency and linewidth (Figure 2.1 (a)),[57, 63–67] fits to the statistics of magnetic switching as a function of current and magnetic field (Figure 2.1 (b)),[62, 68] and analyses of the current dependence of magnetic astroids and switching phase diagrams,[69, 70]. Those methods excite magnetic dynamics at all frequencies. They can measure spin transfer torques if used carefully. However, heating and nonuniform dynamics can produce artifacts.

Spin torque ferromagnetic resonance uses a microwave frequency current to drive small angle resonant magnetic dynamics in the linear regime (Figure 2.2 (d)) and produce an oscillating resistance. It can provide information about the device including strength of the spin torque, magnetic damping, and demagne-

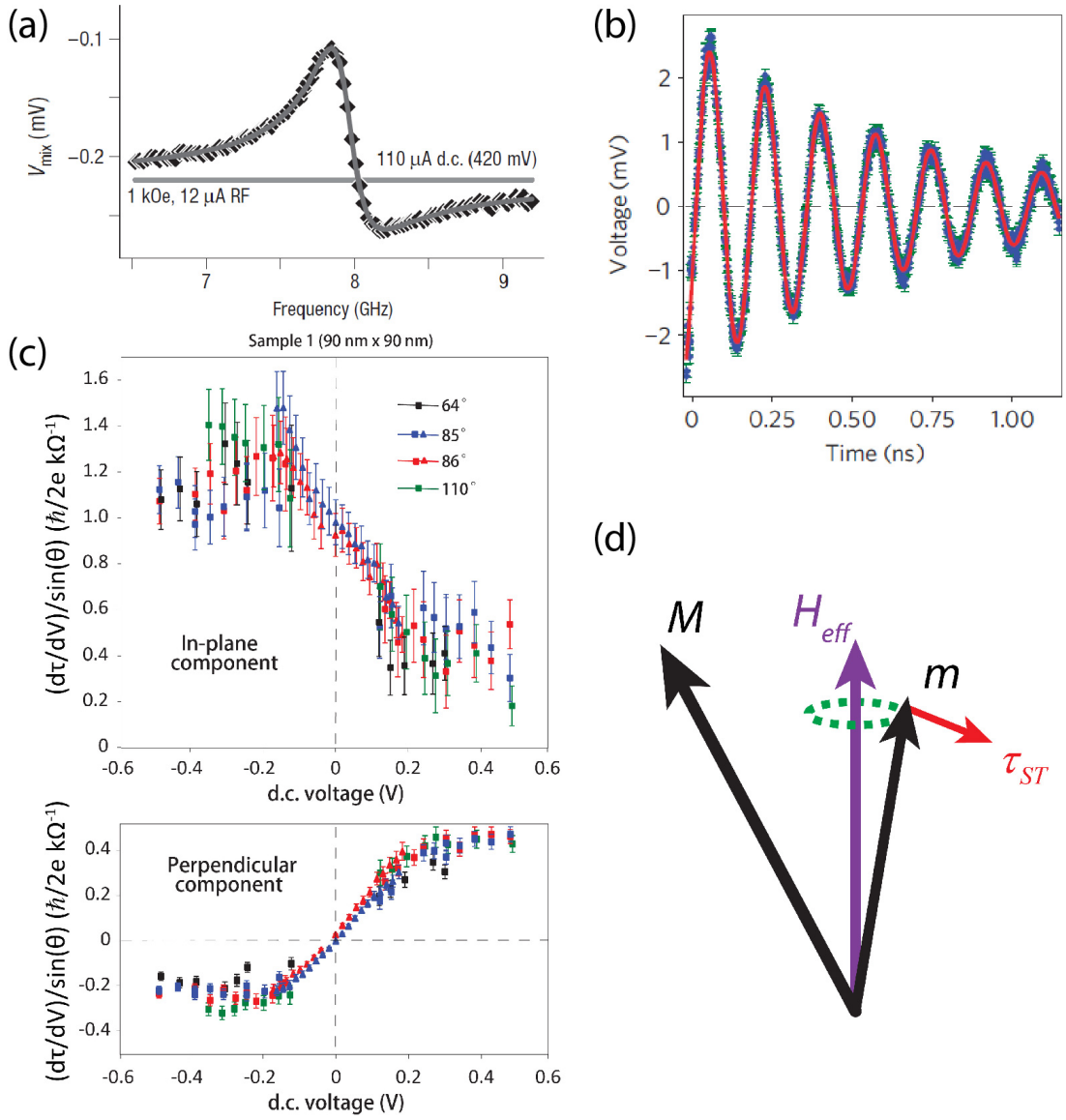

Figure 2.2: ST-FMR measurement. (a) DC-voltage-detected ST-FMR. The DC component of the mixing voltage is measured as a function of the microwave frequency. Adapted from Reference [71]. (b) Time-domain detection of ST-FMR. High frequency voltage signal is measured in the time domain at the scale of about 1 nanosecond. Adapted from Reference [55]. (c) Results in terms of torkance for both in-plane and perpendicular components of the spin torque in a MTJ. Adapted from Reference [55]. (d) Small angle resonant magnetic dynamics driven by a microwave current.

	DC-detected	Time-domain
Equipment	microwave generator, lock-in amplifier	microwave generator, high-bandwidth oscilloscope, pulse generators
Advantage	rapid, easy to implement	can reach high bias beyond DC break-down voltage
Disadvantage	artifacts at middle bias range and above	does not work for zero bias
Voltage Range	low bias	middle and high bias

Table 2.1: Comparison between the two conventional ST-FMR techniques

tization field. DC-voltage-detected spin torque ferromagnetic resonance (Figure 2.2 (a)),[71–73] measures the DC component in the mixing of the microwave current and the oscillating resistance

$$V_{\text{mix}} = (I_{\text{RF}}\cos(\omega t)\Delta R\cos(\omega t))\,|_{\text{DC}}. \tag{2.1}$$

Time-domain detection of ST-FMR (Figure 2.2 (b)) measures the microwave frequency signal from the mixing of an applied DC current and the oscillating resistance [55]

$$V(t) = I_{\text{DC}}\Delta R\cos(\omega t). \tag{2.2}$$

The direct results from ST-FMR are measurements of the derivative of the torque versus the voltage bias, which is often referred to as *torkance* (Figure 2.2 (c)). The value of spin torque can be obtained by doing a numerical integration.

Of all the conventional methods, in the high bias regime that is relevant for applications, we believe that the time-domain ST-FMR technique is the most accurate and trustworthy, since it measures directly the amplitude and phase of small-angle magnetic precession in response to an oscillating spin torque and therefore is least susceptible to artifacts associated with heating, spatially nonuniform magnetic dynamics, and changes in the DC resistance in response

to spin torque.[55, 73] However, time-domain ST-FMR requires expensive, specialized equipment (i.e., a high-bandwidth oscilloscope and multiple pulse generators) (see Table 2.1). It is of great interest to develop a new type of ST-FMR technique that is easy to implement and artifacts-free at a reasonably high bias. In this chapter, we show that it is possible to use a simple network analyzer measurement to determine the bias dependence of the spin torque vector, by studying the resonant response of a magnetic tunnel junction subject to both DC and microwave currents. We find excellent agreement with time-domain ST-FMR measurements[55] made on the same devices.

2.2 Device Information

The MgO-based magnetic tunnel junctions (MTJs) that we study came from the same batches measured in References [55] and [74], with resistance-area products for the tunnel barriers equal to RA = 1.5 $\Omega \cdot \mu m^2$ and 1.0 $\Omega \cdot \mu m^2$. We will present data for one sample with RA = 1.5 $\Omega \cdot \mu m^2$, a resistance of 272 Ω in the parallel state, and a tunneling magnetoresistance (TMR) of 91%, but we found similar behavior in three other samples. The device on which we will focus has the layer structure (in nm): bottom electrode, IrMn pinned synthetic antiferromagnet (SAF) [IrMn(6.1)/CoFe(1.8)/Ru/CoFeB(2.0)], tunnel barrier [MgO_x], magnetic free layer [CoFe(0.5)/CoFeB(3.4)], capping layer [Ru(6.0)/Ta(3.0)/Ru(4.0)]. Both the pinned layer and the free layer were patterned into a circular cross section with a nominal 90 nm diameter. All the measurements were done at room temperature. We confirmed that the device properties did not degrade during the process of measurement[75] by checking that the device resistance and TMR remained unchanged. We will use a sign con-

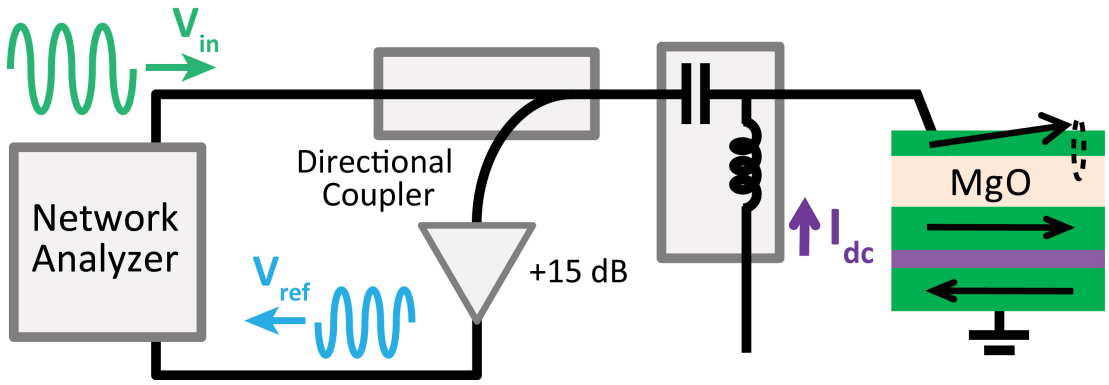

Figure 2.3: The network analyzer circuit used in the measurement.

vention that positive values of current correspond to electron flow from the free layer to the reference layer (giving spin torque favoring antiparallel alignment).

2.3 Methods

We performed measurements with a commercial network analyzer (Agilent 8722ES, 50 MHz – 40 GHz) using the circuit in Figure 2.3. We measured the microwave response in a reflection geometry, using a bias tee to allow simultaneous application of a DC bias to the MTJ. Before routing the reflected microwave signal to the network analyzer, we amplified it using a 15-dB amplifier in combination with a directional coupler. The microwave gain of the amplifier and transmission losses in other circuit components were calibrated by standard methods. Figure 2.4 shows an example of the real and imaginary parts of the reflected signal as a function of frequency, in the frequency range exhibiting spin-torque-driven magnetic resonance. These data correspond to a DC current of -0.4 mA and an applied magnetic field H = 200 Oe oriented 70° from the exchange bias of the SAF reference layer, so that the initial offset angle of the two

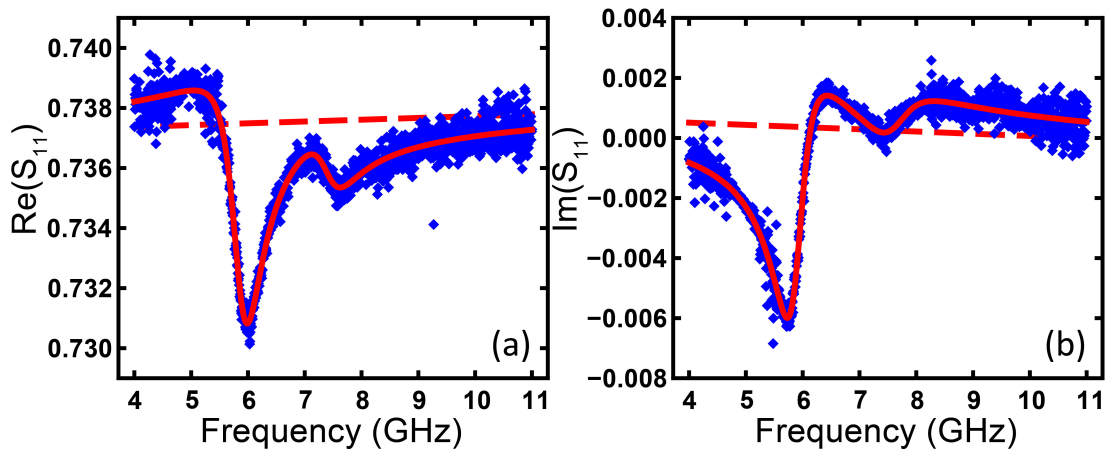

Figure 2.4: The measured reflection signal (S_{11}). (a) real part and (b) imaginary part for I_{DC} = -0.4 mA and a magnetic field H = 200 Oe applied 70° from the exchange bias direction, giving θ = 61°. The solid lines are a fit to eq. (2.3). The dashed lines are the nonresonant backgrounds used in the fits.

magnetic layers is approximately $\theta = 61°$. The microwave excitation signal V_{in} that we applied to the sample had an amplitude always less than 22 mV. Within the model discussed below this results in magnetic precession angles $< 3°$, and we verified that the output signals scaled linearly with V_{in} as expected in the linear-response regime.

To interpret these data, and to use them to measure the strength of the spin transfer torque, we analyze the reflected microwave signal V_{ref} within a macrospin model of the magnetic dynamics, combining the Landau-Lifshitz-Gilbert-Slonczewski equation of motion for a magnetic tunnel junction subject to an oscillating spin torque together with appropriate microwave circuit equations (See Reference [74] for details). The resulting (complex-valued) reflection coefficient corresponding to the resonant magnetic response can be written

$$S_{11} \equiv \frac{V_{ref}}{V_{in}} = \frac{R_0 - (50\Omega)}{R_0 + (50\Omega)} + \frac{(50\Omega)}{R_0 + (50\Omega)} I_{DC}\chi(\omega), \tag{2.3}$$

where

$$\chi(\omega) \equiv \Delta R(\omega)/V_{in} = -\left.\frac{\partial R}{\partial \theta}\right|_I \frac{R_0}{R_0 + (50\Omega)} \frac{\gamma}{M_S Vol} \times \frac{1}{\omega - \omega_m - i\sigma}\left[i \left.\frac{\partial \tau_\parallel}{\partial V}\right|_\theta + \frac{\gamma N_x M_{\text{eff}}}{\omega_m} \left.\frac{\partial \tau_\perp}{\partial V}\right|_\theta \right], \tag{2.4}$$

and the resonance frequency and current-dependent resonant linewidth are

$$\omega_m \approx \gamma M_{\text{eff}} \sqrt{N_x \left[N_y - \frac{1}{M_{\text{eff}} M_S Vol}\left(\left.\frac{\partial \tau_\perp}{\partial \theta}\right|_V + \frac{(50\Omega)}{R_0 + (50\Omega)} I_{\text{DC}} \left.\frac{\partial R}{\partial \theta}\right|_I \left.\frac{\partial \tau_\perp}{\partial V}\right|_\theta \right)\right]}, \tag{2.5}$$

$$\sigma \approx \frac{\alpha\gamma M_{\text{eff}}(N_x + N_y)}{2} - \frac{\gamma}{M_S Vol}\left(\left.\frac{\partial \tau_\parallel}{\partial \theta}\right|_V + \frac{1}{2}\frac{(50\Omega)}{R_0 + (50\Omega)} I_{\text{DC}} \left.\frac{\partial R}{\partial \theta}\right|_I \left.\frac{\partial \tau_\parallel}{\partial V}\right|_\theta \right). \tag{2.6}$$

Here R_0 is the differential resistance of the MTJ, $\Delta R(\omega)$ is the oscillating part of the DC resistance, θ is the angle between the magnetizations of the two electrodes of the MTJ, α is the Gilbert damping parameter, $M_S Vol$ is the total magnetic moment of the free layer, $\tau_\parallel(V,\theta)$ and $\tau_\perp(V,\theta)$ are the in-plane and perpendicular components of the spin torque, V is the voltage across the MTJ including both DC and high-frequency terms, γ is the absolute value of the gyromagnetic ratio, $N_x = 4\pi + H/M_{\text{eff}}$, $N_y \approx H/M_{\text{eff}}$, $4\pi M_{\text{eff}}$ is the strength of the easy-plane anisotropy field, and H is the component of applied magnetic field along the precession axis. When both in-plane and perpendicular components of torque are present, both the real and imaginary parts of the resonant signal consist of a sum of frequency-symmetric and antisymmetric Lorentzian curves. Both torque components can therefore be extracted by fitting the symmetric and antisymmetric parts of either the real or imaginary response.

2.4 Results

The solid lines in Figure 2.4(a) and (b) show an example of the good agreement we find when fitting eq. (2.3) to our resonance measurements. We observe

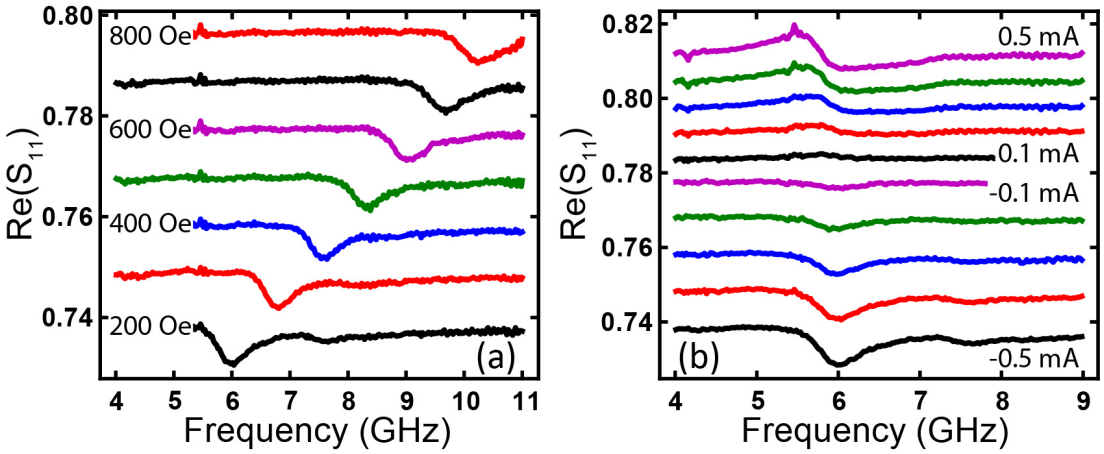

Figure 2.5: The dependences on H and I_{DC} of S_{11}. (a) Measured frequency dependence of the real part of S_{11} for several values of magnetic field applied 70° from the exchange bias direction, with I_{DC} = -0.4 mA. The curves are offset by 0.01 vertically. (b) Measured frequency dependence of the real part of S_{11} for several values of DC current, with H = 200 Oe applied 70° from the exchange bias direction. The curves are offset vertically by 0.01.

two resonances in each panel in Figure 2.4, one with large amplitude near 5.9 GHz and a second with smaller amplitude near 7.5 GHz. We perform separate fits to the real and imaginary curves, employing four free parameters for each resonance in a fit: the center frequency of the resonance, the amplitude of the frequency-symmetric and antisymmetric Lorentzians, and the linewidth (taken to be the same for both the symmetric and antisymmetric components). We allow for a small nonzero constant slope in the non-resonant background signals (dashed lines in Figure 2.4) that may be associated with an imperfect capacitance calibration.

The dependences on H and I_{DC} for the real part of the resonances are shown in Figure 2.5(a) and (b). As in Figure 2.4(a), the spectra contain one primary dip in Re(S_{11}) together with a smaller side resonance at a higher frequency. The primary resonance shifts with H as expected from the Kittel formula [76] while the

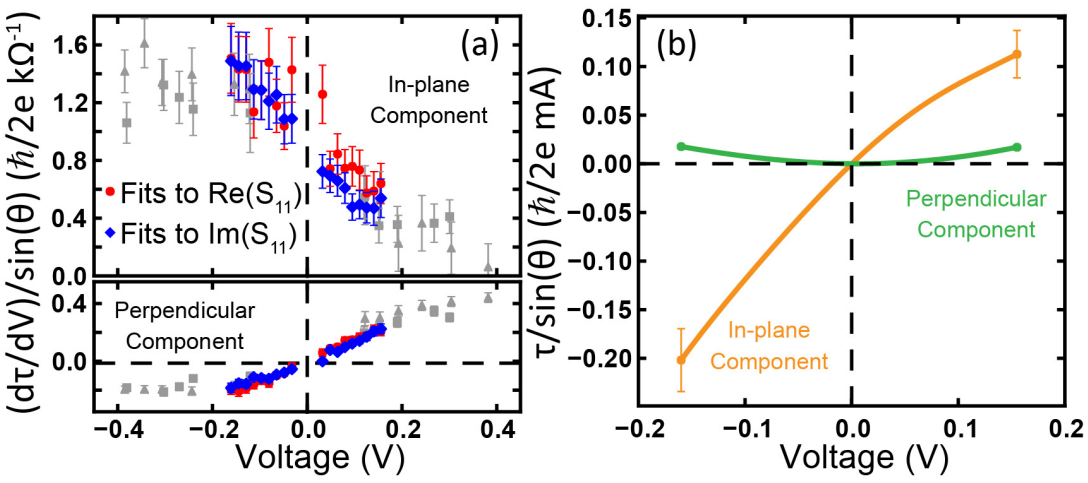

Figure 2.6: Measurement of the spin torque vector. (a) Bias dependence of the in-plane and perpendicular components of the torkance $\partial\tau/\partial V|_\theta$ determined by fitting to the frequency dependence of $\mathrm{Re}(S_{11})$ (red circles) and $\mathrm{Im}(S_{11})$ (blue diamonds) at different values of the DC bias. These data correspond to $H = 200$ Oe applied 70° from the exchange bias direction, giving $\theta = 61°$. For comparison, we also show in gray the results on the same device from time-domain ST-FMR measurements (triangles: for $H = 250$ Oe applied 95° from the exchange bias direction giving $\theta = 85°$; squares: $H = 200$ Oe applied at 68° giving $\theta = 64°$). (b) Integrated in-plane and perpendicular components of the spin torque vector determined by integrating the network-analyzer data in (a), with representative error bars.

secondary signal shifts more slowly and decreases in amplitude with increasing field strength. We suspect that the secondary peak may involve coupled motion of the magnetic layers in the synthetic antiferromagnet polarizing layer. To avoid having this mode interfere with our measurements of spin torque, we select values of magnetic field and magnetic field angle such that the secondary mode has small amplitude and maximum separation in frequency from the primary mode. These are the same selection criteria used in Reference [55].

Based on eqs. (2.3) and (2.4), for any value of bias we can determine the spin transfer torkances $\partial\tau_\parallel/\partial V|_\theta$ and $\partial\tau_\perp/\partial V|_\theta$ from fits to the frequency-symmetric and antisymmetric parts of the primary resonance in either $\mathrm{Re}(S_{11})$ or $\mathrm{Im}(S_{11})$.

In calculating the torkances from the resonant amplitudes we use the following parameters: $M_S Vol = 1.8 \times 10^{-14}$ emu (±15%),[55] $4\pi M_{\text{eff}} = 13 \pm 1$ kOe determined from high-field measurements of the resonance frequency, and $\alpha = 0.016 \pm 0.001$ determined by measuring the resonance linewidth at positive and negative biases and interpolating to zero bias. In Figure 2.6(a), we plot the bias dependence of the resulting torkances as found by the network analyzer technique. We normalize the results by Sin θ since the spin torque of a MTJ is predicted to have this angular dependence.[77] We note that the torkance values determined by independent fits to the real and imaginary parts of the resonance agree, as is required in order that our analysis procedure be self-consistent. Figure 2.6(a) also shows a comparison to measurements on the same sample using the time-domain ST-FMR technique introduced in Reference [55], whereby the magnetic precession driven by a resonant spin torque is detected by a fast oscilloscope. We find excellent agreement between the two types of measurements. The in-plane component of the torkance, $\partial\tau_{\parallel}/\partial V|_{\theta}$, measured by the two techniques agrees in magnitude near zero bias with the same moderate dependence on bias, with no adjustment of parameters for either technique. The perpendicular component $\partial\tau_{\perp}/\partial V|_{\theta}$ displays the same approximately linear bias dependence at low bias. In Figure 2.6(b), we plot the full bias dependent torques $\tau_{\parallel}(V)$ and $\tau_{\perp}(V)$, obtained by numerical integration of the torkances.

2.5 Comparison with Previous Methods

The detailed comparison is shown in Table 2.2. Neither the network-analyzer ST-FMR technique nor the time-domain ST-FMR technique can be used at $V = 0$, because a non-zero DC bias is required to generate the oscillatory voltage signal

	DC-detected	Time-domain	Network Analyzer
Equipment	microwave generator, lock-in amplifier	microwave generator, high-bandwidth oscilloscope, pulse generators	network analyzer
Advantage	rapid, easy to implement	can reach high bias beyond DC break-down voltage	rapid, artifacts free, as sensitive as time-domain
Disadvantage	artifacts at middle bias range and above	does not work for zero bias	does not work for zero bias
Voltage Range	low bias	middle and high bias	middle bias

Table 2.2: Comparison between the ST-FMR techniques including the network analyzer technique.

that is measured (see Figure 2.6(a)). (For measurements near zero bias, DC-voltage-detected ST-FMR can provide accurate torque measurements without artifacts in the mixing signal.[71–73]) The time-domain ST-FMR technique allows measurements to higher biases, because it is naturally implemented using short bias pulses that are less likely to produce dielectric breakdown in the tunnel barrier, compared to the constant DC biases used in our network analyzer technique. However, in the bias range shown in Figure 2.6(a,b) the network analyzer method provides a more convenient approach in that it does not require specialized, expensive equipment, while it yields a sensitivity comparable to time-domain ST-FMR.

2.6 Summary

In summary, we demonstrate that it is possible to use a simple network-analyzer technique to measure the strength and direction of the spin transfer torque vector as a function of bias in magnetic tunnel junctions. This technique provides

roughly similar sensitivity as the time-domain ST-FMR method,[55] making it useful as a simple and rapid means for characterizing spin-torque devices.

CHAPTER 3

CONDITIONS FOR MICROWAVE AMPLIFICATION DUE TO SPIN-TORQUE DYNAMICS IN MAGNETIC TUNNEL JUNCTIONS

Spin torque from a microwave current flowing through a magnetic tunnel junction (MTJ) can excite resonant magnetic dynamics and hence resistance oscillations. When a DC current is also applied, the MTJ produces an oscillating voltage at the frequency of the input signal. This oscillating voltage increases with DC bias and can in principle become larger than the input signal, yielding amplification. In this chapter, we discuss analytically with evidence from experiments on how to design tunnel junction devices to achieve gains larger than one. We find that voltage gains larger than 1 can be achieved in 2-terminal MTJs, but that needs fine-tuning of the magnetic orientation and DC bias to make the effective damping go to zero. Gains larger than 100 are achievable in optimized 3-terminal devices. The work discussed in this chapter was published in Reference [74].

3.1 Introduction

Spin transfer torque allows efficient current-controlled manipulation of the magnetic moment in magnetic devices.[13–15] This mechanism is being applied rapidly for technology: spin-torque-controlled magnetic nonvolatile random access memory is nearing commercialization,[78] and other potentially useful devices have been demonstrated including frequency-tunable microwave sources,[46, 79, 80] frequency modulators,[81, 82] and microwave detectors.[54, 83] Here we analyze another potential application of spin-torque devices, as microwave-frequency amplifiers.

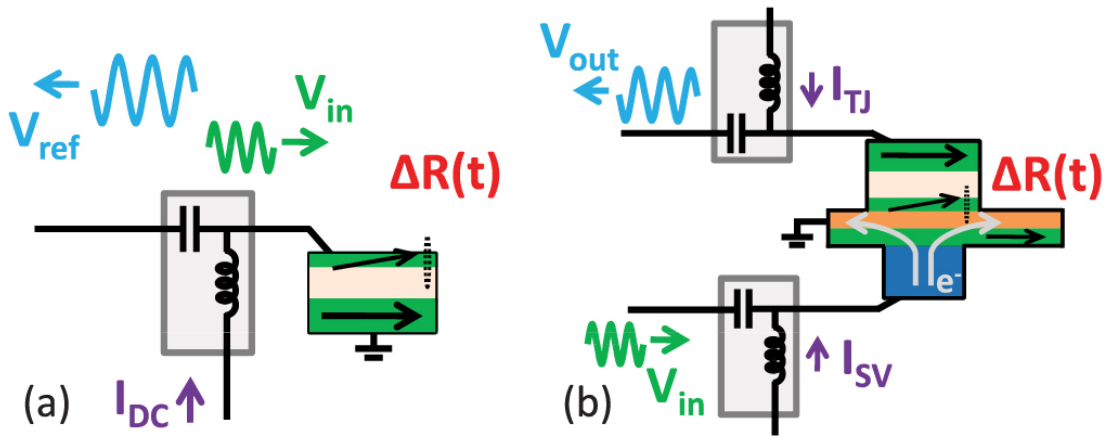

Figure 3.1: Illustration of the mechanism of microwave amplification in two different device structures. (a) For a standard 2-terminal magnetic tunnel junction. (b) Proposed design for a 3-terminal device.

The idea of making a microwave amplifier using spin torque was first proposed by Slonczewski,[84] and other amplification schemes have been proposed using negative differential resistance [85] or magnetic vortex oscillations.[86, 87] The mechanism of gain we will consider is illustrated for a simple 2-terminal magnetic tunnel junction (MTJ) in Figure 3.1(a). An input microwave signal, V_{in}, generates resonant magnetic precession via a spin-transfer torque exerted on one electrode of the MTJ, and thereby produces resistance oscillations. If a DC current is also applied, the oscillating resistance produces an oscillating voltage by Ohm's law that can be transmitted out of the MTJ as a reflected signal V_{ref}. If the applied DC current is sufficiently large, then the reflected signal can be larger than the input signal, yielding amplification. We will analyze the simplest case in which the MTJ magnetic layers are in-plane in equilibrium, and the microwave drive excites small-angle, approximately spatially uniform magnetic precession.

3.2 Analysis

The high-frequency signal generated by a MTJ in response to a microwave-frequency input can be calculated using microwave circuit equations together with methods to analyze the magnetic dynamics similar to those employed for spin-torque ferromagnetic resonance (ST-FMR)[54, 58, 73] and thermally excited ferromagnetic resonance.[63] Assuming that the waveguide contacting the sample has a 50 Ω impedance, the reflected signal arising from an input signal $V_{in}(\omega)$ together with an oscillating resistance is

$$V_{ref}(\omega) = \frac{R_0 - (50\Omega)}{R_0 + (50\Omega)} V_{in}(\omega) + \frac{(50\Omega)}{R_0 + (50\Omega)} I_{DC} \Delta R(\omega), \tag{3.1}$$

where R_0 is the differential resistance of the MTJ and $\Delta R(\omega)$ is the oscillating part of the DC resistance. The first term is the reflection that results from impedance mismatch between the 50 Ω waveguide and the MTJ, and the second term is the signal generated by the oscillating resistance. We assume small angle precession, so that $\Delta R(\omega) = \partial R/\partial\theta|_I \delta\theta(\omega)$, where θ is the angle between the magnetizations of the two electrodes of the MTJ. To calculate the precession angle $\delta\theta(\omega)$, we approximate the magnetization of the free layer in the MTJ (the one that precesses) as a spatially-uniform macrospin with direction $\hat{m}$, we assume that the other magnetic electrode remains fixed, and we use the Landau-Lifshitz-Gilbert-Slonczewski equation of motion:[13, 15]

$$\frac{d\hat{m}}{dt} = -\gamma \hat{m} \times \vec{H}_{\text{eff}} + \alpha \hat{m} \times \frac{d\hat{m}}{dt} + \gamma \frac{\tau_{\parallel}(V,\theta)}{M_S Vol} \hat{m} \times \frac{\hat{m} \times \hat{M}}{|\hat{m} \times \hat{M}|} + \gamma \frac{\tau_{\perp}(V,\theta)}{M_S Vol} \frac{\hat{m} \times \hat{M}}{|\hat{m} \times \hat{M}|}. \tag{3.2}$$

Here $\vec{H}_{\text{eff}}$ is the effective field acting on the free layer including the applied, demagnetization, and exchange fields; α is the Gilbert damping parameter; $M_S Vol$ is the total moment of the free layer; $\tau_{\parallel}(V,\theta)$ and $\tau_{\perp}(V,\theta)$ are the in-plane and perpendicular components of the spin torque;[73] $V = V_{\text{DC}} + \delta V(\omega)$ is the voltage

across the MTJ; and γ is the absolute value of the gyromagnetic ratio. The final ingredient for a closed set of equations is to relate $\delta V(\omega)$, the oscillating part of the voltage across the MTJ, to the input and reflected voltages:

$$\delta V(\omega) = V_{in}(\omega) + V_{ref}(\omega) = \frac{2R_0}{R_0 + (50\Omega)} V_{in} + \frac{(50\Omega) I_{\mathrm{DC}} \Delta R(\omega)}{R_0 + (50\Omega)}. \tag{3.3}$$

This expression takes into account a feedback mechanism,[88] that the oscillating resistance will alter the voltage across the MTJ and will thus affect the spin torque that drives the oscillation.

By solving eqs. (3.1) to (3.3) for a circular 2-terminal MTJ for which the magnetizations of both electrodes lie in the sample plane in equilibrium, we calculate a (complex-valued) voltage gain:

$$S_{11} \equiv \frac{R_0 - (50\Omega)}{R_0 + (50\Omega)} + \frac{(50\Omega)}{R_0 + (50\Omega)} I_{\mathrm{DC}} \chi(\omega), \tag{3.4}$$

where

$$\begin{aligned} \chi(\omega) \equiv \Delta R(\omega)/V_{in} = &- \left.\frac{\partial R}{\partial \theta}\right|_I \frac{R_0}{R_0 + (50\Omega)} \frac{\gamma}{M_{\mathrm{S}} Vol} \\ &\times \frac{1}{\omega - \omega_m - i\sigma} \left[i \left.\frac{\partial \tau_{\parallel}}{\partial V}\right|_\theta + \frac{\gamma N_x M_{\mathrm{eff}}}{\omega_m} \left.\frac{\partial \tau_{\perp}}{\partial V}\right|_\theta \right], \end{aligned} \tag{3.5}$$

$$\omega_m \approx \gamma M_{\mathrm{eff}} \sqrt{N_x \left[N_y - \frac{1}{M_{\mathrm{eff}} M_{\mathrm{S}} Vol} \left(\left.\frac{\partial \tau_{\perp}}{\partial \theta}\right|_V + \frac{(50\Omega)}{R_0 + (50\Omega)} I_{\mathrm{DC}} \left.\frac{\partial R}{\partial \theta}\right|_I \left.\frac{\partial \tau_{\perp}}{\partial V}\right|_\theta \right) \right]}, \tag{3.6}$$

$$\sigma \approx \frac{\alpha \gamma M_{\mathrm{eff}} (N_x + N_y)}{2} - \frac{\gamma}{M_{\mathrm{S}} Vol} \left(\left.\frac{\partial \tau_{\parallel}}{\partial \theta}\right|_V + \frac{1}{2} \frac{(50\Omega)}{R_0 + (50\Omega)} I_{\mathrm{DC}} \left.\frac{\partial R}{\partial \theta}\right|_I \left.\frac{\partial \tau_{\parallel}}{\partial V}\right|_\theta \right). \tag{3.7}$$

Here $N_x = 4\pi + H/M_{\mathrm{eff}}$, $N_y \approx H/M_{\mathrm{eff}}$, $4\pi M_{\mathrm{eff}}$ is the strength of the easy-plane anisotropy field, and H is component of applied magnetic field along the precession axis. The real and imaginary parts of S_{11} correspond to the in-phase and out-of-phase response. This calculation predicts resonance peaks at the ferromagnetic resonance frequency, with line shapes as a function of frequency as plotted in Figure 3.2. We have verified that the calculated signals

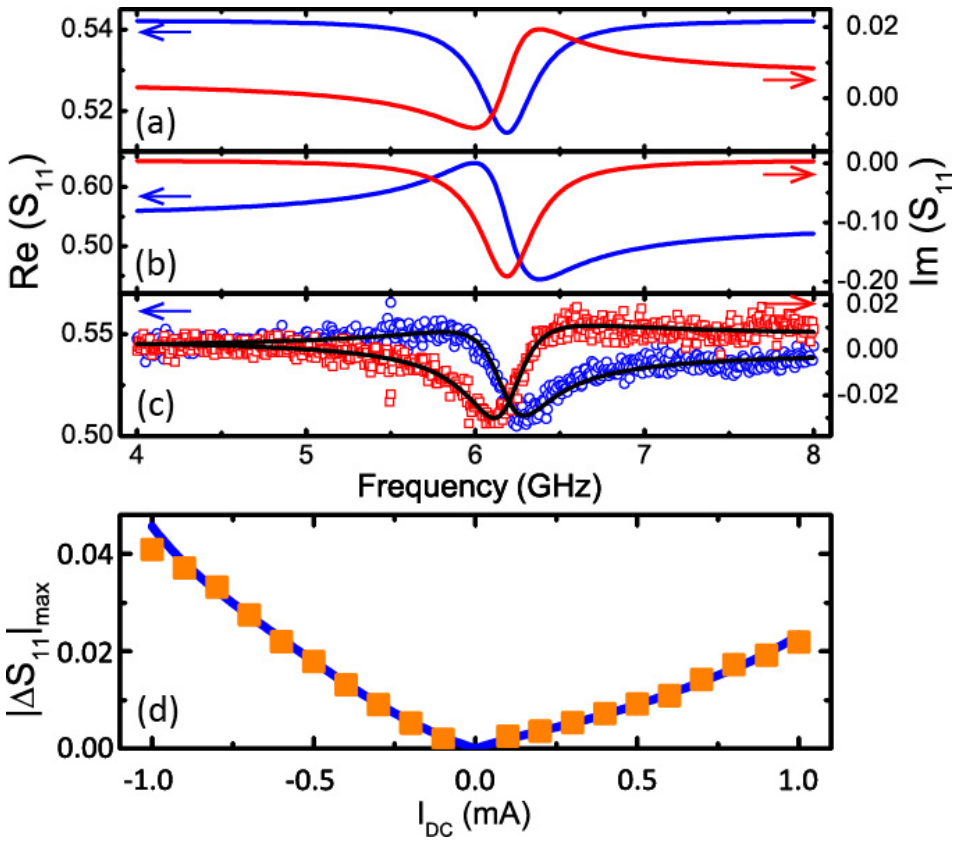

Figure 3.2: The high-frequency response of 2-terminal MTJs. (a,b) Calculated frequency dependence for the real (blue lines, left axes) and imaginary (red lines, right axes) parts of S_{11} for (a) a purely in-plane spin torque and (b) a purely out-of-plane spin torque. When both torque components are present, S_{11} is a weighted sum of the two contributions. (c) Points: real and imaginary parts of the measured S_{11} signal for a CoFeB/MgO/CoFeB MTJ with $R_P = 122\ \Omega$, TMR = 78% and $RA = 1.0\ \Omega\text{m}^2$ for I_{DC} = -1.0 mA and H = 300 Oe applied 145° from the fixed-layers exchange bias direction. The lines are fits to eq. (3.4) with the fit values $\partial\tau_\parallel/\partial V|_\theta = 2.8 \pm 0.5(\hbar/2e)\text{k}\Omega^{-1}$ and $\partial\tau_\perp/\partial V|_\theta = -0.5 \pm 0.1(\hbar/2e)\text{k}\Omega^{-1}$. (d) Points: measured gain for the same unoptimized MTJ and field bias. Line: prediction of eq. (3.4) for $\partial\tau_\parallel/\partial V|_\theta = 1.8(\hbar/2e)\text{k}\Omega^{-1} - 930I(\hbar/2e)\text{kV}^{-1}$ and $\partial\tau_\perp/\partial V|_\theta = -0.06(\hbar/2e)\text{k}\Omega^{-1} + 520I(\hbar/2e)\text{kV}^{-1}$.

are in good agreement with network-analyzer measurements on (unoptimized) CoFeB/MgO/CoFeB MTJs (Figures 3.2(c,d)), although for these samples the gains are much less than 1.

3.3 Calculation of the Gain for a 2-Terminal MTJ

We can estimate what is the maximum possible voltage gain from a simple 2-terminal MTJ by evaluating eq. (3.4) using the following optimistic but reasonable parameters: resistance for parallel electrode magnetizations $R_P = 50\ \Omega$; tunneling magnetoresistance, TMR = 150%; $M_S Vol = 5.8 \times 10^{-15}$ emu; $\alpha = 0.01$; $H = 100$ Oe; $4\pi M_{\text{eff}} = 1.1$ kOe (assuming a reduction by about factor of 10 compared to a typical metal ferromagnet due to the introduction of perpendicular magnetic anisotropy[89]); $\tau_\perp(V,\theta) \approx 3.8\ \text{V}^2\sin\theta(\hbar/2e)\text{k}\Omega^{-1}\text{V}^{-1}$, and $\tau_\parallel(V,\theta) \approx 6.9\ \text{V}\sin\theta(\hbar/2e)\text{k}\Omega^{-1}$. These spin-torque values are determined by scaling the results in Figure 3(b) of Reference [55] inversely by the ratio of the samples' zero-bias parallel resistances and assuming for simplicity that $\tau_\perp \propto V^2$ and $\tau_\parallel \propto V$. In Figures 3.3(a), (c) and (d), we plot the magnitude of the maximum change in S_{11} near resonance. We find that voltage gains greater than one are possible, but they require fine-tuning the offset angle and I_{DC} very precisely to bias the sample near the critical current where the bias-dependent linewidth σ goes to zero, the threshold for exciting DC-driven auto-oscillations. Somewhat better amplification might be achievable using devices biased to generate nonlinear, large-angle precessional dynamics [90] not described within our small-angle approximation, but nevertheless we conclude that this need for fine-tuning near a point of singular dynamics (i.e., adjusting for time-dependent sample variations and thermal fluctuations) likely prohibits the use of simple 2-terminal MTJs for microwave amplifier applications.

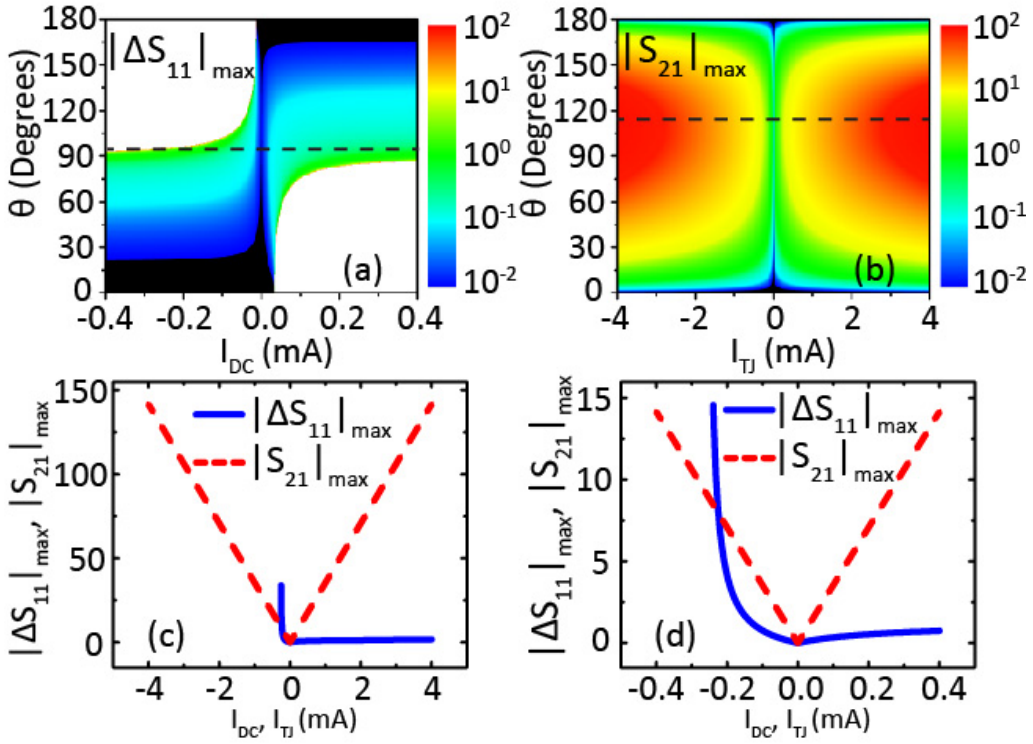

Figure 3.3: Calculations of microwave amplification. (a) Log-scale color plot of the calculated maximum value of ΔS_{11} for an optimized 2-terminal MTJ, as a function of I_{DC} and the offset angle θ between the magnetization directions of the two electrodes. The white regions at the upper left and lower right represent parts of the phase diagram where the DC current generates auto-oscillations with no applied oscillatory current. (b) Log-scale color plot of the calculated maximum value of $|S_{21}|$ for an optimized 3-terminal MTJ, as a function of the DC current through the MTJ and the offset angle θ between the magnetizations of the MTJ electrodes. (c) Comparison of the voltage gain factors for optimized 2-terminal and 3-terminal MTJs, for the values of θ shown by dotted lines in (a) and (b). The current on the horizontal axis corresponds to the DC current applied to the MTJ (not the spin valve in the 3-terminal device). (d) Zoom-in of the data in (c), showing the detailed dependence near zero current.

3.4 Calculation of the Gain for a 3-Terminal Device

Larger, controllable gains should be achievable in 3-terminal devices. This was the approach originally proposed by Slonczewski.[84] We consider a geometry similar to devices recently studied by Sun et al.[43] (Figure 3.1(b)), consisting of a lower CoFe/Cu/CoFeB all-metal, low-resistance spin valve in which the CoFeB free layer (assumed circular) can be manipulated by spin torque via non-local spin injection, together with a MgO/CoFeB tunnel junction cap by which the moving free layer can generate large resistance oscillations. This geometry can facilitate the application of large microwave currents through port 1 to the metal spin valve to generate large free-layer oscillations, with the possibility to use a DC current I_{SV} through the spin valve to control the bias-dependent linewidth to be stably close to zero. The large-TMR MTJ with a separate DC bias I_{TJ} generates the output signal through port 2. We can use an analysis similar to that employed above to estimate the voltage gain (S_{21}). Assuming that the differential resistance for the MTJ is R_0 and for the spin valve is R_{SV}, the DC resistance of the MTJ is R_{TJ}, and the equilibrium orientations of all three magnetic layers are in the sample plane,

$$S_{21} = \frac{V_{out}}{V_{in}} = -\frac{I_{\mathrm{TJ}}}{R_0 + (50\Omega)}\left(\frac{2(50\Omega)}{R_{\mathrm{SV}} + (50\Omega)}\right)\frac{\partial R_{\mathrm{TJ}}}{\partial\theta}\frac{\gamma}{2M_{\mathrm{S}}Vol} \times\left(\frac{1}{\omega - \omega_m - i\sigma}\right) i\left.\frac{\partial\tau_{\parallel}}{\partial I_{\mathrm{SV}}}\right|_{\theta}. \tag{3.8}$$

We have not included a perpendicular component of torque because this component should be absent for all-metal spin valves.[58] For estimation purposes, we use the optimistic parameters: R_{TJ} = 50 Ω in the parallel configuration, TMR = 150%, R_{SV} = 3 Ω, $M_{\mathrm{S}}Vol = 5.8\times10^{-15}$emu, $\partial\tau_{\parallel}/\partial I_{\mathrm{SV}}|_{\theta}$= 0.4 $\sin\theta_{\mathrm{SV}}(\hbar/2e)$,[91] and σ = 3 $\times10^{7}$ rad/s (this is a factor of 100 reduction compared to a typical transition metal ferromagnet; we assume a factor of 10 reduction by using perpendicular

anisotropy to reduce $4\pi M_{\rm eff}$[89] and another factor of 10 by using $I_{\rm SV}$ to reduce the bias-dependent linewidth, and we assume $I_{\rm SV}$ is adjusted as a function of $I_{\rm TJ}$ to keep σ constant at this reduced value). Figures 3.3(b), (c) and (d) show the calculated value of $|S_{21}|$ near resonance as a function of $I_{\rm TJ}$ and θ. This calculation indicates that a voltage gain larger than 100 is achievable using physically reasonable materials parameters. The associated power gain-bandwidth product is $|S_{21}(\omega_m)|^2\sigma/\pi \sim 200$ GHz and scales $\propto 1/\sigma$. Even larger gains may be possible using other sample geometries (e.g., employing a reference layer polarized out of plane, while the free layer remains polarized in plane) or by applying out-of-plane magnetic field to achieve a large-angle, nonlinear magnetic response.[90]

3.5 Discussion and Summary

Our analysis does not yet include consideration of noise.[92] The output noise of the amplifier associated with thermal fluctuations of the free layer will increase as the volume of the free layer is decreased so as to maximize the gain. This will likely constrain the values of $M_{\rm S}Vol$ and H that can be employed when optimizing device properties.

In summary, we have analyzed the conditions under which MTJ-based devices might be used to generate resonant microwave amplification. Gain greater than 1 is possible in principle even in simple 2-terminal tunnel junctions, but is unlikely to be controllable because this requires biasing the sample very close to a point of singular dynamics where the bias-dependent linewidth goes to zero. However, 3-terminal tunnel-junction devices should be able to achieve controllable microwave voltage gains of at least 100.

CHAPTER 4

RESONANCE MEASUREMENT OF NONLOCAL SPIN TORQUE IN A THREE-TERMINAL MAGNETIC DEVICE

A pure spin current generated within a nonlocal spin valve can exert a spin transfer torque on a nanomagnet. This nonlocal torque enables new design schemes for magnetic memory devices that do not require the application of large voltages across tunnel barriers that can suffer electrical breakdown. We report in this chapter a quantitative measurement of this nonlocal spin torque using spin-torque-driven ferromagnetic resonance. Our measurement agrees well with the prediction of an effective circuit model for spin transport. Based on this model, we suggest strategies for optimizing the strength of nonlocal torque. The work discussed in this chapter was published in Reference [93].

4.1 Introduction

Spin transfer torque enables the efficient manipulation of magnetization in nanoscale magnetic devices [13–15]. Spin torque due to the flow of a spin-polarized charge current within conventional two-terminal magnetic tunnel junctions (MTJs) and magnetic multilayer devices has been studied intensively and is being developed for technology. In addition, it has been shown recently that in multiterminal device structures (Figure 4.1 (a)) a spin torque can also be exerted by a *nonlocal* pure spin current (meaning a spin current associated with zero net charge flow, as distinct from a spin-polarized charge current) [43, 94–96], in agreement with predictions [84]. This nonlocal spin torque can be sufficiently strong to cause magnetic reversal (Figure 4.1 (b)) [43, 94–96]. However, thus far the only means of detecting nonlocal spin torques in multitermi-

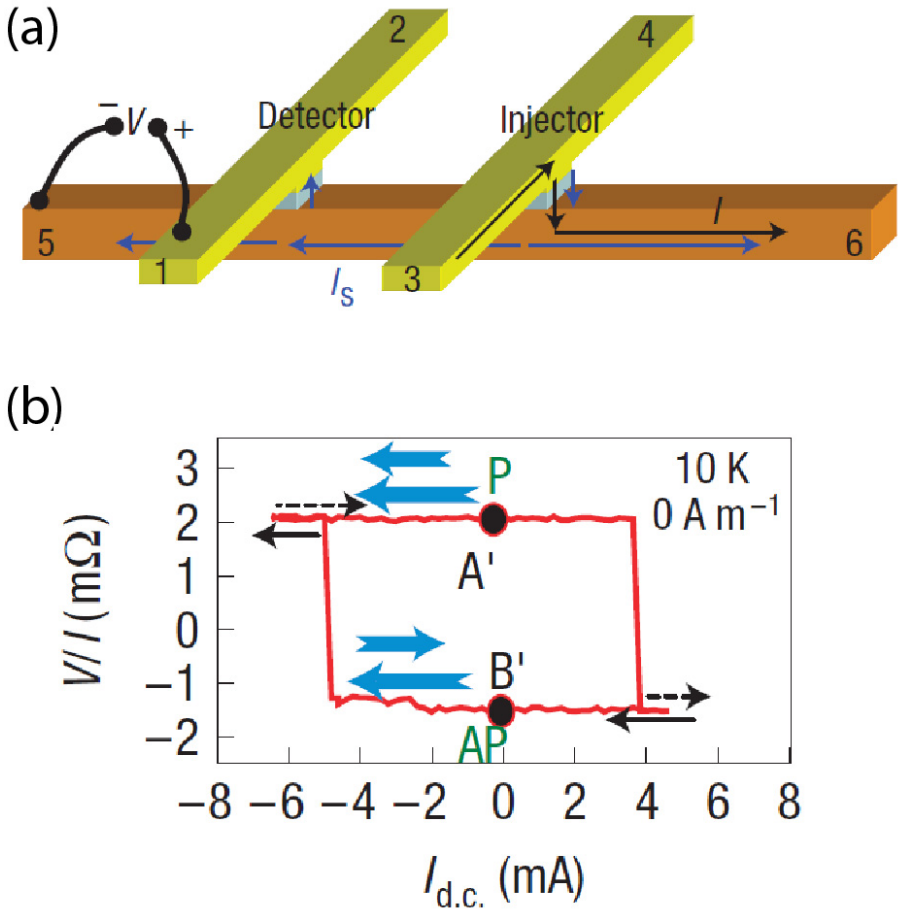

Figure 4.1: Nonlocal spin torque in a multiterminal device. (a) Multiterminal device structure. (b) Magnetic reversal in the device driven by the nonlocal spin torque. Adapted from Reference [94].

nal devices has been to observe full magnetic reversal, which does not provide a quantitative torque measurement and which yields information only in the high bias regime. Here we report measurements of nonlocal spin torque using spin-torque-driven ferromagnetic resonance (ST-FMR) [54, 55, 58, 71–73], a technique that is both quantitative and that operates for any applied bias. We compare the measured nonlocal torque to the prediction of an effective circuit model of spin transport, finding reasonable agreement, and we suggest strategies for further optimization.

4.2 Device

The device geometry we consider is a three-terminal structure consisting of a lower all-metal spin valve with a MTJ on top (Figure 4.2(a)). Nonlocal spin-torque switching has been measured previously by the IBM group in devices with the same design, except for a slightly thicker spin injection layer [43]. An applied charge current passes from a bottom TaN electrode (terminal T1) approximately 100 nm in diameter through an exchange-biased PtMn(17.5 nm)/$Co_{70}Fe_{30}$(3.5 nm) bilayer (magnetic layer F1) and out of the device laterally through a PtMn(17.5 nm)/$Co_{70}Fe_{30}$(3.5 nm)/Cu(N)(30 nm) multilayer (terminal T2), where Cu(N) means nitrogen-doped Cu. This generates spin accumulation in the Cu(N) channel above the TaN contact. A pure spin current can then diffuse to a 2 nm $Co_{60}Fe_{20}B_{20}$ layer (magnetic layer F2) positioned above the Cu(N) channel. This layer F2 will serve as the magnetic free layer in the experiment, reorienting in response to the nonlocal spin torque. The cross section of F2 is approximately an ellipse, 70×150 nm^2, with the long axis parallel to the exchange bias direction of F1. We have also measured 80×120 nm^2 and 90×200 nm^2 devices with similar results. The device structure is completed by an MgO-based MTJ positioned above F2, whose magnetoresistance (measured between terminals T2 and T3) depends on the orientation of F2. We will discuss data for a sample with a MTJ resistance of 30.9 kΩ in the parallel magnetic state with a tunneling magnetoresistance of 39% and with a metallic channel resistance (between the contact pads of terminals T1 and T2) of 23 Ω.

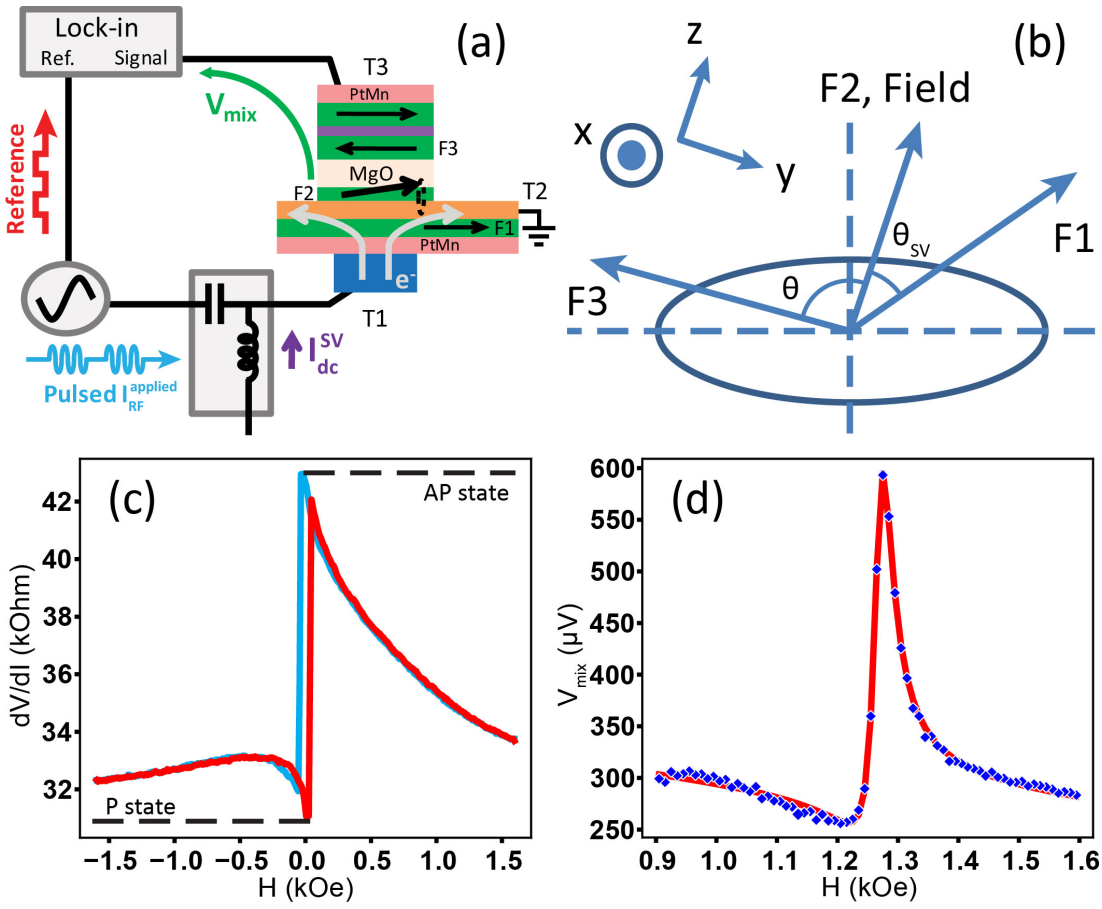

Figure 4.2: Measurement circuit and device information. (a) Illustration of the ST-FMR circuit. (b) Orientations of the magnetic moments of layers F1, F2, and F3 when a magnetic field of 1.3 kOe is applied 75° from the exchange bias direction. (c) Differential resistance vs. external magnetic field applied 75° from the exchange bias direction. The resistances for parallel and antiparallel alignment between F2 and F3 are indicated. (d) (points) Measured ST-FMR signal at 12 GHz for a magnetic field orientation 75° from the exchange bias direction ($\theta_{SV} \approx 35°$ at resonance) with $I_{dc}^{SV} = 5$ mA. (line) Fit to eq. (4.1) assuming a linear dependence on H for the background.

4.3 Methods

To perform an ST-FMR measurement of the nonlocal spin torque, we first apply a magnetic field H in the sample plane approximately perpendicular to the exchange-bias direction so as to turn the magnetization of the free layer F2 away from the magnetization of F1 and F3. Layer F2 has a small coercive field ($\sim$ 30 Oe), so that to a good approximation in a magnetic field of order 1 kOe it aligns to the field direction. Layers F3 and F1 are reoriented by lesser amounts because F3 is part of a synthetic antiferromagnet and F1 is subject to an approximately 1.1 kOe exchange bias through interaction with PtMn (see Figures 4.2(b,c)). The next step of the measurement is to apply a pulsed microwave-frequency current with magnitude $I_{\mathrm{RF}}^{\mathrm{applied}}$ between the contact pads leading to terminals T1 and T2. This produces an oscillatory nonlocal spin torque that causes the magnetization of the free layer to precess. We measure the precession by detecting a dc voltage that results across the MTJ (between terminals T2 and T3) as a consequence of mixing between the oscillating resistance of the MTJ and an oscillating current $I_{\mathrm{RF}}^{\mathrm{leakage}}$ of order $10^{-3} I_{\mathrm{RF}}^{\mathrm{applied}}$ that flows through the MTJ. (If $I_{\mathrm{RF}}^{\mathrm{leakage}}$ had been too small to provide a mixing measurement of the resonance, we could also have applied a separate microwave current directly to the MTJ to give the same effect.) All measurements are performed at room temperature, and we use the convention that negative currents correspond to electron flow in the direction of the arrows in Figure 4.2(a) (giving a torque favoring parallel alignment between F2 and F1).

Figure 4.2(d) shows an example of a nonlocal ST-FMR resonance peak measured for a fixed microwave frequency $\omega/(2\pi)$ = 12 GHz, for a swept magnetic field oriented 75° from the exchange bias direction of layer F1, and for a dc cur-

rent $I_{\mathrm{dc}}^{\mathrm{SV}} = 5$ mA applied between terminals T1 and T2. We used excitation currents $I_{\mathrm{RF}}^{\mathrm{applied}} < 1.9$ mA and verified that the output mixing signal scaled $\propto (I_{\mathrm{RF}}^{\mathrm{applied}})^2$ so that the magnetic response is in the linear regime.

The lineshapes of the nonlocal ST-FMR signals can be understood by modeling the dynamics of the magnetic free layer in a macrospin approximation and adapting the theory used to analyze ST-FMR in a two-terminal MTJ [55], with the result that the resonant part of the signal should have the simple form:

$$\text{resonance} \propto c_S S(\omega, H) + c_A A(\omega, H). \tag{4.1}$$

Here $S(\omega, H) = \{1 + [\omega - \omega_m(H)]^2/\sigma^2\}^{-1} \approx [1 + (H - H_m)^2/(\Delta H)^2]^{-1}$ is a symmetric Lorentzian peak as a function of ω or H, $A(\omega, H) = \{[\omega - \omega_m(H)]/\sigma\} S(\omega, H)$ is an antisymmetric Lorentzian with the same linewidth, ω_m is the resonance frequency at a given value of H (see Section 4.7 below), σ is the frequency linewidth, H_m is the resonance field at a given value of ω, and $\Delta H \approx \sigma/[\mathrm{d}\omega_m/\mathrm{d}H]$ is the field linewidth. The prefactors c_S and c_A are to a good approximation constant as a function of H in the region of the resonance, but they depend on the current and ω. The measurement may also contain a nonresonant background that can depend weakly on H. The linewidth parameter σ is predicted (see Section 4.7) to depend on the magnitude of the in-plane component $\tau_\parallel$ of the spin transfer torque in the form

$$\sigma \approx \frac{\alpha\gamma M_{\mathrm{eff}}(N_x + N_y)}{2} - \frac{\gamma}{M_s \times \mathrm{Vol}} \left.\frac{\partial \tau_\parallel(I_{\mathrm{SV}}, \theta_{\mathrm{SV}})}{\partial \theta_{\mathrm{SV}}}\right|_{I_{\mathrm{SV}}}. \tag{4.2}$$

Here α is the Gilbert damping coefficient, $\gamma = 2\mu_B/\hbar$ is the absolute value of the gyromagnetic ratio, $4\pi M_{\mathrm{eff}}$ is the effective in-plane anisotropy of layer F2, $N_x = 4\pi + H/M_{\mathrm{eff}}$, $N_y \approx H/M_{\mathrm{eff}}$, $M_s \times \mathrm{Vol}$ is the total magnetic moment of F2, I_{SV} is the current in the spin-valve part of the device between terminals T1 and T2, and θ_{SV} is the offset angle between F2 and F1. For an all-metal spin valve,

the spin torque should have only an in-plane component (i.e., in the direction $\hat{m} \times (\hat{m} \times \hat{M})/|\hat{m} \times \hat{M}|$, where $\hat{m}$ is the orientation of the free layer moment and $\hat{M}$ is the orientation of the polarizer layer) [15], so eq. (4.2) allows a measurement of the full nonlocal spin transfer torque.

A fit of eq. (4.1) to a measured resonance lineshape is included in Figure 4.2(d), using the fitting parameters $\sigma = (5.94 \pm 0.08) \times 10^8$ radHz, and $c_S/c_A = -1.33 \pm 0.03$. We allow for a linear dependence on H for the nonresonant background, but ignore the weak dependence of θ_{SV} and σ on H near the resonance. The fit in Figure 4.2(d) is excellent, and we observe a similar quality of agreement for different values of ω, field angle, and I_{SV}. From the measured resonance frequencies, we determine $4\pi M_{\mathrm{eff}} = 13 \pm 1$ kOe (see also Section 4.7).

4.4 Results

The strength of the nonlocal spin torque can be determined most accurately (see more explanation in Section 4.7) from the resonance measurement by using eq. (4.2) to analyze the dependence of the resonance linewidth on I_{SV}. A similar approach has been used previously to measure spin torque in magnetic tunnel junctions [63] and due to the spin Hall effect [2, 97]. We show in Figure 4.3(a) the measured evolution of the resonance as a function of $I_{\mathrm{dc}}^{\mathrm{SV}}$ (the dc component of I_{SV}), for $\omega/(2\pi) = 12$ GHz and a field orientation 75° relative to the exchange bias direction. We observe that the linewidth depends linearly on $I_{\mathrm{dc}}^{\mathrm{SV}}$ (Figure 4.3(b)). By fitting to eq. (4.2) and using as above that $4\pi M_{\mathrm{eff}} = 13 \pm 1$ kOe (with $M_{\mathrm{S}} = 1100$ emu/cm^3 [71] and with the free-layer volume Vol $= 1.7 \times 10^{-17}$ cm^3), we determine $\partial\tau_{\parallel}/\partial I_{\mathrm{SV}}|_{\theta_{\mathrm{SV}}} = 0.05 \pm 0.01(\hbar/2e)$ and $\alpha = 0.012 \pm 0.002$ for these

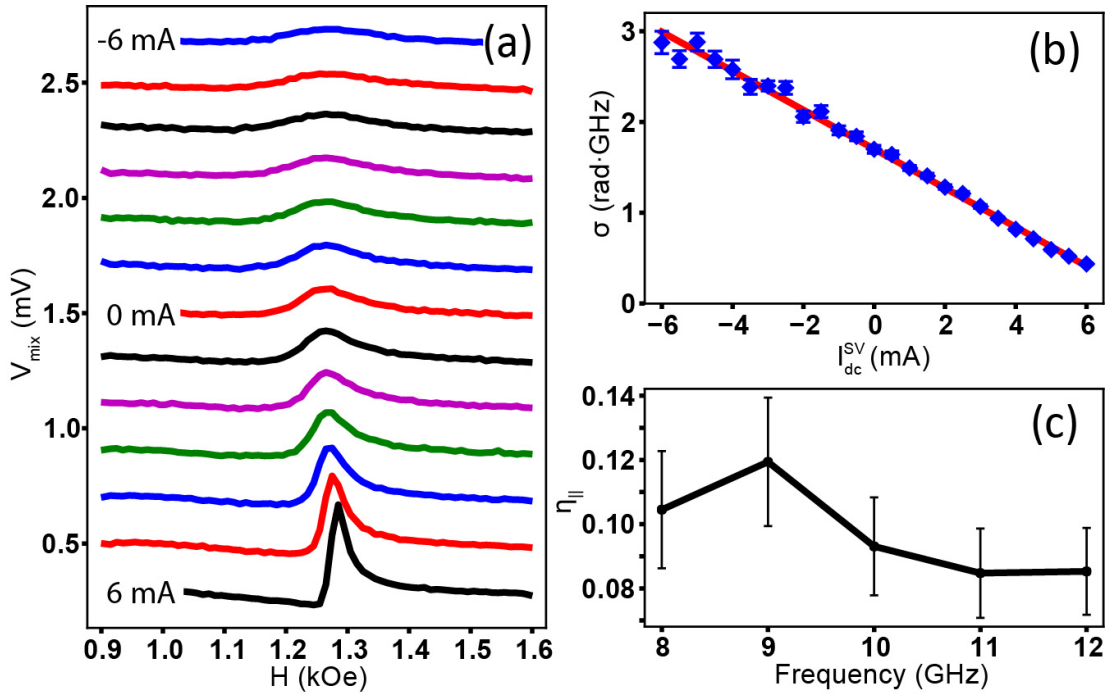

Figure 4.3: Measurement of the nonlocal spin torque. (a) ST-FMR signals measured, for different values of $I_{\rm dc}^{\rm SV}$, at 12 GHz for a magnetic field orientation 75° from the exchange bias direction ($\theta_{\rm SV} \approx 35°$ at resonance). Curves are offset vertically by 0.2 mV. (b) Dependence of resonant linewidth σ on $I_{\rm dc}^{\rm SV}$ for the data in (a). (c) Efficiency of the in-plane spin torque, defined as $\eta_{\parallel} = [2e/(\hbar I_{\rm SV}\cos\theta_{\rm SV})]\partial\tau_{\parallel}/\partial\theta_{\rm SV}|_{I_{\rm SV}}$, determined from ST-FMR measurements of σ vs. $I_{\rm dc}^{\rm SV}$ together with eq. (4.2), for different values of resonant microwave frequency.

experimental conditions.

We have carried out similar measurements of linewidth versus $I_{\rm dc}^{\rm SV}$ for field angles of 60° and 75° and for field magnitudes yielding resonance frequencies from 8 to 12 GHz. When comparing results for different fields, we take into account that the nonlocal spin torque should be proportional to the component of the spin current perpendicular to the free layer magnetization, so that $\tau_{\parallel} = (\hbar/2e)\eta_{\parallel} I_{\rm SV}\sin\theta_{\rm SV}$ (or $\partial\tau_{\parallel}/\partial\theta_{\rm SV}|_{I_{\rm SV}} = (\hbar/2e)\eta_{\parallel} I_{\rm SV}\cos\theta_{\rm SV}$), where $\eta_{\parallel}$ is a dimensionless efficiency. We estimate $\theta_{\rm SV}$ by assuming that the magnetization of F2 aligns with

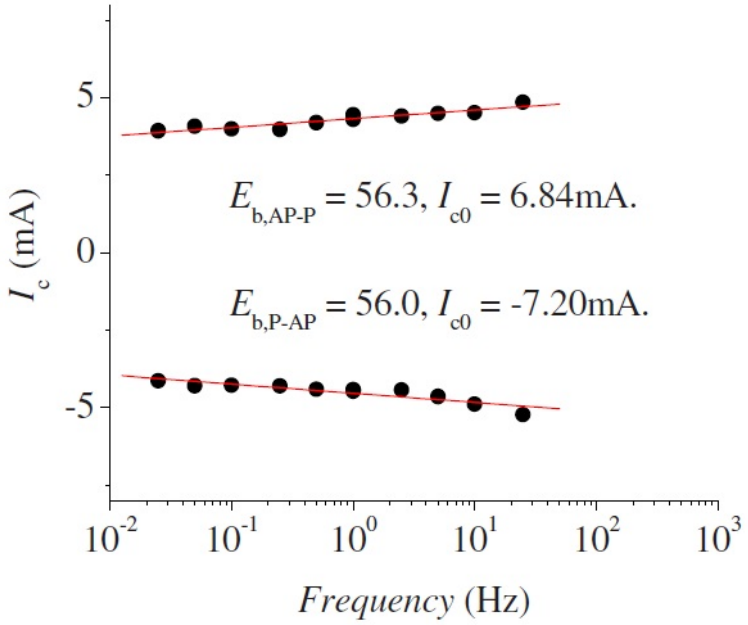

Figure 4.4: Sweep-rate dependence of the critical current from the pulse switching measurement. Adapted from Reference [43].

the applied field and calculating the magnetization angle of F1 by assuming that it responds as a macrospin to the combined action of H and the exchange field H_{ex} = 1.1 ± 0.2 kOe [98]. Figure 4.3(c) shows separate measurements of the spin-torque efficiency $\eta_{\|}$ for a range of field magnitudes (0.6-1.3 kOe at an angle of 75°), that correspond to resonance frequencies of 8-12 GHz and offset angles θ_{SV} between 49° and 35°. Our final overall value for the efficiency of the nonlocal spin torque is $\eta_{\|} = 0.10 \pm 0.02$.

Sun *et al.* [43] performed spin-torque switching experiments with devices of the same structure except with a slightly thicker injection layer F1 and obtained a zero temperature critical switching current I_{c0} = -6.84 mA for θ_{SV} near 180° and I_{c0} = 7.20 mA for θ_{SV} near 0° for a device cross section of 69 × 161 nm^2. (See Figure 4.4.) For an in-plane magnetized free layer in zero external field, $I_{c0} \approx (2e/\hbar) \times (\alpha M_S \times \mathrm{Vol}/\eta_{\|})(2\pi M_{eff})$ [99]. Therefore, the switching measurement can also be

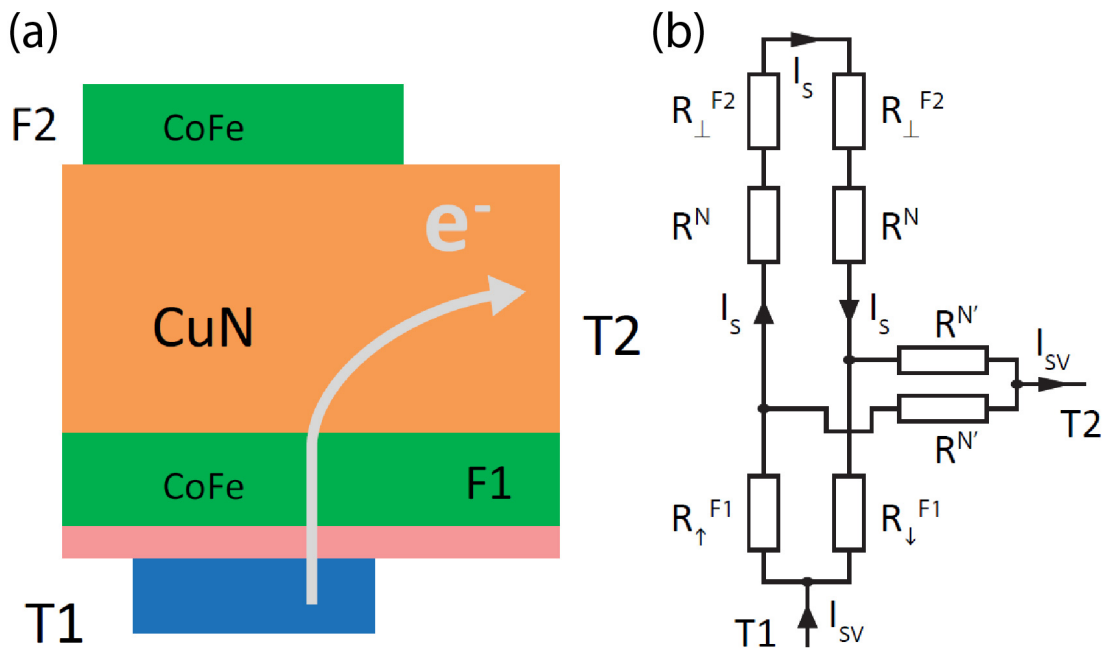

Figure 4.5: Modeling of the spin valve part of the device. (a) The spin valve part of the device. (b) Effective circuit of (a) for modeling spin currents when $\theta_{SV} = 90°$. The total current of spin angular momentum absorbed by layer F2 is $2(\hbar/2e)I_S$.

used to estimate the spin torque efficiency $\eta_{||}$ if α and $4\pi M_{eff}$ are known. By using the values obtained above from our resonance measurements, $\alpha = 0.012 \pm 0.002$ and $4\pi M_{eff} = 13 \pm 1$ kOe, the switching currents from Reference. [43] correspond to an in-plane spin-torque efficiency $\eta_{||} = 0.07 \pm 0.02$, consistent with our ST-FMR result.

4.5 Calculation from Theory

The value of the nonlocal torque that should be expected theoretically can be estimated using an effective circuit model [11, 100–102] for spin transport. For the case $\theta_{SV} = 90°$, the simple effective circuit in Figure 4.5 (b) applies. (For other

angles, as noted above, we expect the spin torque should be proportional to $\sin\theta_{SV}$.) In this circuit model, we assume that the spin accumulation relaxes only by flow to the free layer F2 or by flow through the normal contact N′ toward T2. Using materials parameters appropriate to our sample geometry, we estimate that the spin-dependent resistances appropriate for N′, the spin injector layer F1, the Cu(N) spacer N, and the free layer F2 are approximately $R^{N'} \approx 0.6 \pm 0.2\Omega$, $R_{\uparrow}^{F1} \approx 0.07\Omega$, $R_{\downarrow}^{F1} \approx 0.29 \pm 0.08\Omega$, $R^{N} \approx 0.44\Omega$, and $R_{\perp}^{F2} \approx 0.016\Omega$ (see detailed calculation in Section 4.7). Solving the circuit, the calculated spin torque efficiency is

$$\eta_{circuit} \equiv \frac{2I_S}{I_{SV}} = \frac{R^{N'}(R_{\downarrow}^{F1} - R_{\uparrow}^{F1})}{(R_{\downarrow}^{F1} + R_{\uparrow}^{F1})(R_{\perp}^{F2} + R^{N} + R^{N'}) + 2R^{N'}(R_{\perp}^{F2} + R^{N})} \approx 0.14 \pm 0.04 \quad (4.3)$$

The prediction of the circuit model is therefore in quite reasonable agreement with our measurement.

To achieve optimal efficiency based on eq. (4.3), the device parameters should satisfy three conditions: (i) a large intrinsic injector polarization $P = (R_{\downarrow}^{F1} - R_{\uparrow}^{F1})/(R_{\downarrow}^{F1} + R_{\uparrow}^{F1})$, (ii) a small spin resistance for electrons going from the injector to the magnetic free layer to apply a spin torque, $R_{\perp}^{F2} + R^{N} \ll R_{\downarrow}^{F1} + R_{\uparrow}^{F1}$, and (iii) a large spin resistance for electrons flowing toward terminal T2, $R^{N'} \gg R_{\perp}^{F2} + R^{N}$, so as to prevent spin current from escaping by this path rather than applying a torque to F2. However, in the existing device design, neither conditions (ii) or (iii) are fully satisfied. To improve the spin torque efficiency, the effective resistance of the spin injector (layer F1) can be increased relative to R^{N}, perhaps by using tunnel-barrier injection, by decreasing the thickness of the Cu(N) layer below 30 nm, and/or by reducing the resistivity of the Cu(N) layer. The device performance can also be improved by increasing $R^{N'}$ relative to R^{N} by reducing the thickness of the 30 nm Cu(N) layer and/or by increasing the spin relaxation length $l_{SF}^{N'}$ by eliminating the PtMn/$Co_{70}Fe_{30}$ layers underneath the portion of

the Cu(N) layer not adjacent to the injector region. If conditions (ii) and (iii) are fully met, then the optimum nonlocal spin torque efficiency should equal the injector polarization, $\eta_{circuit} = P$, meaning that the nonlocal spin torque can be made just as efficient as the spin torque in conventional two-terminal devices.

4.6 Summary

In summary, we have performed an ST-FMR measurement of the nonlocal spin torque due to a pure spin current in a three-terminal device. We measure a spin torque efficiency $(\partial\tau_{\parallel}/\partial I_{\mathrm{SV}})[2e/(\hbar \sin\theta_{\mathrm{SV}})] = 0.10 \pm 0.02$. This agrees well with the efficiency expected within an effective circuit model. Based on the circuit analysis, we estimate that the nonlocal device geometry can be optimized so that the strength of the nonlocal torque should reach $\partial\tau_{\parallel}/\partial I_{\mathrm{SV}} = P \sin\theta_{\mathrm{SV}}\hbar/2e$, the same value expected for the local spin torque in two-terminal devices. Because of the low resistance of the spin-valve current channel in the three-terminal devices, the ratio of the spin torque to the applied power is already much greater in the existing three-terminal devices than in two-terminal MTJs. The nonlocal spin torque in three-terminal devices therefore possesses a combination of virtues relative to conventional MTJs – reduced susceptibility to tunnel barrier breakdown and reduced power consumption together with high spin torque efficiency – that can make this device geometry an interesting candidate for applications.

4.7 Appendices

4.7.1 Derivation of the Resonance Line Shape for Nonlocal ST-FMR

To derive the line shapes of the nonlocal ST-FMR signals we adapt the theory used to analyze ST-FMR in a 2-terminal MTJ [55]. We assume the free layer is uniformly magnetized in the direction $\hat{m}(t)$, while the other magnetic layers remain fixed in response to $I_{\mathrm{RF}}^{\mathrm{applied}}$. We use the convention that the z axis lies in the sample plane along the equilibrium direction of $\hat{m}$ in the absence of any applied microwave current, with the x and y axes as shown in Figure 4.2 (b) of the main paper. We assume that all of the magnetic layers have equilibrium orientations in the sample plane, and that the dynamics of $\hat{m}(t)$ are governed by the Landau-Lifshitz-Gilbert-Slonczewski equation of motion:

$$\frac{d\hat{m}}{dt} = -\gamma\hat{m}\times\vec{H}_{\mathrm{eff}} + \alpha\hat{m}\times\frac{d\hat{m}}{dt} + \gamma\frac{\tau_{\parallel}(I_{\mathrm{SV}},\theta_{\mathrm{SV}})}{M_{\mathrm{S}}Vol}\hat{m}\times\frac{\hat{m}\times\hat{M}}{|\hat{m}\times\hat{M}|} + \gamma\frac{\tau_{\perp}(I_{\mathrm{SV}},\theta_{\mathrm{SV}})}{M_{\mathrm{S}}Vol}\frac{\hat{m}\times\hat{M}}{|\hat{m}\times\hat{M}|}. \quad (4.4)$$

Here $\hat{M}$ is the orientation of layer F1; $M_{\mathrm{S}}Vol$ is the total magnetic moment of F2; θ_{SV} is the offset angle between F2 and F1; $I_{\mathrm{SV}} = I_{\mathrm{RF}}^{\mathrm{SV}} + I_{\mathrm{dc}}^{\mathrm{SV}}$ is the charge current between terminals T1 and T2; $\tau_{\parallel}(I_{\mathrm{SV}},\theta_{\mathrm{SV}})$ and $\tau_{\perp}(I_{\mathrm{SV}},\theta_{\mathrm{SV}})$ are the in-plane and perpendicular components of the current-induced torque; $\vec{H}_{\mathrm{eff}} = -N_x M_{\mathrm{eff}} m_x\hat{x} - N_y M_{\mathrm{eff}} m_y\hat{y}$ is the effective field acting on F2, with $N_x = 4\pi + H/M_{\mathrm{eff}}$, $N_y = H/M_{\mathrm{eff}}$, and H the component of external field along $\hat{z}$; $\gamma = 2\mu_{\mathrm{B}}/\hbar$ is the absolute value of the gyromagnetic ratio; and α is the Gilbert damping coefficient. We expect that the spin torque within a nonlocal all-metal spin valve should have only an in-plane component [15], but we include an out-of-plane component as well to account for possible torques due to current-induced Oersted fields. The unit

vectors $\hat{m}\times\hat{M}/|\hat{m}\times\hat{M}|$ and $\hat{m}\times(\hat{m}\times\hat{M})/|\hat{m}\times\hat{M}|$ in eq. (4.4) do not possess any dependence on the magnetic field as long as it is applied in the sample plane.

By solving eq. (4.4) for a small enough $I_{\mathrm{RF}}^{\mathrm{applied}}$ that the magnetic response is in the linear regime we find

$$m_y = \frac{\gamma I_{\mathrm{RF}}^{\mathrm{SV}}}{2M_{\mathrm{S}}Vol}\frac{1}{\omega-\omega_m-i\sigma}\left(i\left.\frac{\partial\tau_{\parallel}(I_{\mathrm{dc}}^{\mathrm{SV}},\theta_{\mathrm{SV}})}{\partial I_{\mathrm{SV}}}\right|_{\theta_{\mathrm{SV}}}+\frac{\gamma N_x M_{\mathrm{eff}}}{\omega_m}\left.\frac{\partial\tau_{\perp}(I_{\mathrm{dc}}^{\mathrm{SV}},\theta_{\mathrm{SV}}))}{\partial I_{\mathrm{SV}}}\right|_{\theta_{\mathrm{SV}}}\right), \quad (4.5)$$

where

$$\omega_m \approx \gamma M_{\mathrm{eff}}\sqrt{N_x\left(N_y-\frac{1}{M_{\mathrm{eff}}M_{\mathrm{S}}Vol}\left.\frac{\partial\tau_{\perp}(I_{\mathrm{dc}}^{\mathrm{SV}},\theta_{\mathrm{SV}})}{\partial\theta_{\mathrm{SV}}}\right|_{I_{\mathrm{SV}}}\right)}, \quad (4.6)$$

$$\sigma \approx \frac{\alpha\gamma M_{\mathrm{eff}}(N_x+N_y)}{2}-\frac{\gamma}{M_{\mathrm{S}}Vol}\left.\frac{\partial\tau_{\parallel}(I_{\mathrm{dc}}^{\mathrm{SV}},\theta_{\mathrm{SV}})}{\partial\theta_{\mathrm{SV}}}\right|_{I_{\mathrm{SV}}}. \quad (4.7)$$

When the magnetization of F2 precesses, the angle between the magnetizations of F2 and F3 changes as $\delta\theta_{\mathrm{TJ}} = \mathrm{Re}(m_y)$. We write that the current through the MTJ can be separated into oscillatory and dc parts as $I_{\mathrm{TJ}}(t) = \delta I_{\mathrm{TJ}}(t)+I_{\mathrm{dc}}^{\mathrm{TJ}}$ where $\delta I_{\mathrm{TJ}}(t) = \mathrm{Re}[I_{\mathrm{RF}}^{\mathrm{leakage}}e^{i\phi+\omega t}]$ and the phase ϕ is defined relative to $I_{\mathrm{RF}}^{\mathrm{SV}}$. (Because of parasitic capacitances and/or inductances in the measurement circuit, this relative phase ϕ between the microwave leakage current through the tunnel junction $\delta I_{\mathrm{TJ}}(t)$ and the microwave current through the spin valve $I_{\mathrm{RF}}^{\mathrm{SV}}$ is in general non-zero.) The dc mixing voltage across the MTJ then takes the form

$$V_{\mathrm{mix}} \approx \frac{1}{4}\frac{\partial^2 V}{\partial I_{\mathrm{TJ}}^2}\left(I_{\mathrm{RF}}^{\mathrm{leakage}}\right)^2+\frac{1}{2}\frac{\partial^2 V}{\partial I_{\mathrm{TJ}}\partial\theta_{\mathrm{TJ}}}\frac{\hbar\gamma\sin\theta_{\mathrm{SV}}}{4eM_{\mathrm{s}}Vol\sigma}I_{\mathrm{RF}}^{\mathrm{leakage}}I_{\mathrm{RF}}^{\mathrm{SV}}\left[c_S S(\omega,H)+c_A A(\omega,H)\right] \quad (4.8)$$

with $c_S = -\xi_{\parallel}\cos\phi+\xi_{\perp}\Omega_{\perp}\sin\phi$, $c_A = \xi_{\perp}\Omega_{\perp}\cos\phi+\xi_{\parallel}\sin\phi$, $S(\omega,H) = \left[1+(\omega-\omega_m(H))^2/\sigma^2\right]^{-1} \approx \left[1+(H-H_m)^2(d\omega_m(H_m)/dH)^2/\sigma^2\right]^{-1}$, $A(\omega,H) = [(\omega-\omega_m(H))/\sigma]\,S(\omega,H)$, and H_m being the field value for which $\omega_m=\omega$. Here $\xi_{\parallel} = [2e/(\hbar\sin\theta_{\mathrm{SV}})]d\tau_{\parallel}/dI_{\mathrm{SV}}$ and $\xi_{\perp} = [2e/(\hbar\sin\theta_{\mathrm{SV}})]d\tau_{\perp}/dI_{\mathrm{SV}}$ represent the in-plane and perpendicular torkances in dimensionless units and $\Omega_{\perp} = \gamma N_x M_{\mathrm{eff}}/\omega_m$. As we noted in the main text, the resonant lineshape [the final term in 4.8] is a

weighted sum of $S(\omega, H)$ (a symmetric Lorentzian peak as a function of ω or H) and $A(\omega, H)$ (an antisymmetric Lorentzian), both with the same frequency linewidth σ. The first term in 4.8 is a nonresonant background that may depend weakly on H.

In order to obtain experimental data to fit to eq. (4.8), we performed the ST-FMR measurements at fixed microwave frequency while sweeping magnetic field, rather than at fixed field while sweeping frequency as in our previous experiments [55, 58, 71, 73], because in a 3-terminal device it is not possible to calibrate the externally-applied microwave current so that both I_{RF}^{SV} and $I_{RF}^{leakage}$ are simultaneously kept flat as the frequency is varied. In our fitting, we allow for a linear dependence on H for the nonresonant background in eq. (4.8), but we assume that I_{RF}^{SV} and $I_{RF}^{leakage}$ are independent of H and we ignore the weak dependence of θ_{SV}, θ_{TJ}, and σ on H near the resonance.

4.7.2 Why do We Determine the Spin Torque Magnitude from the Resonance Linewidth rather than the Resonance Amplitude?

In principle, one can also measure the spin torque by analyzing the amplitude of the ST-FMR resonance peak (see eq. (4.8) above), to reach a separate determination that is independent of our analysis of the resonance linewidth. We have used analyses of resonance amplitudes previously to measure the magnitude of the local spin torque in 2-terminal magnetic tunnel junctions [71, 73]. However, because the 3-terminal devices we analyze here were not designed with

microwave-frequency experiments in mind, parasitic capacitances in the device structure produce current shunting and a non-zero phase shift between I_{RF}^{TJ} and I_{RF}^{SV} that is difficult to quantify accurately. This adds significant uncertainty to an analysis of the resonance amplitudes because it can alter the relative amplitudes of the symmetric and antisymmetric parts of the resonance (see eq. (4.8) and the definitions for c_S and c_A that follow it). For determining the magnitude of the spin torque in our 3-terminal devices, it is therefore more accurate to analyze the current dependence of the resonance linewidth, because this quantity has no dependence on ϕ.

4.7.3 Estimation of Sample Parameters for the Effective Circuit Model of Spin Transport

We estimate the spin resistances for the effective circuit drawn in Figure 4.5 (b) of the main paper as follows:

The spin resistances of the $Co_{70}Fe_{30}$ spin polarizing layer F1 are estimated as $R_{\uparrow}^{F1} = 2\rho_{F1}t_{F1}/[A_{F1}(1+P)]$ and $R_{\downarrow}^{F1} = 2\rho_{F1}t_{F1}/[A_{F1}(1-P)]$, with ρ_{F1}=130 nΩ·m [103] the resistivity of this layer, t_{F1} = 3.5 nm its thickness, A_{F1} = 7900 nm^2 its area, and $P = (R_{\downarrow}^{F1} - R_{\uparrow}^{F1})/(R_{\downarrow}^{F1} + R_{\uparrow}^{F1}) = 0.6 \pm 0.1$ [103, 104] its spin polarization. Here we ignore any additional spin-dependent interface resistance because its effects should be negligible [105]. We also make the rough approximation that $t_{F1} \approx l_{SF}^{F1}$, the spin diffusion length in CoFe. This has been measured to be $l_{SF}^{F1} \approx 9$ nm at 4.2 K and should be smaller at room temperature [105].

For the spin resistance of the Cu(N) spacer layer we use $R^N = 2\rho_N t_N/A_N$, with

ρ_N = 60 nΩ·m [43], t_N = 30 nm, and A_N = 8200 nm^2.

For the spin resistance of that part of the $Co_{60}Fe_{20}B_{20}$ free layer F2 over which an incident spin component with orientation perpendicular to the magnetization of F2 will be reoriented by precession, we estimate $R_{\perp}^{F2} = 2\rho_{F2}l_{ex}/A_{F2}$, with ρ_{F2} = 130 nΩ·m [103] and A_{F2} = 8200 nm^2. The precession length should be of order the lattice spacing, $l_{ex} \sim 0.5$ nm [15].

Finally, for the effective spin resistance corresponding to radial diffusion away from the circular contact toward terminal T2, we estimate $R^{N'} = 2\rho_{N'}\ln[(r_{eff} + l_{SF}^{N'})/r_{eff}]/(2\pi t_{N'})$. Here $\rho_{N'}$ = 60 nΩ·m [43], $r_{eff} \approx 25$ nm is half the injector radius, and $t_{N'} \approx 30$ nm. $l_{SF}^{N'}$ is an effective spin diffusion length for the $Co_{70}Fe_{30}$(3.5 nm)/Cu(N)(30 nm) electrode that we estimate to be $l_{SF}^{N'} \approx 34$ nm ± 50% based on a layer-thickness-weighted average of the relaxation rates in $Co_{70}Fe_{30}$ and Cu [106].

Our final estimates for the resistances in the effective circuit are $R_{\uparrow}^{F1} \approx 0.07\Omega$, $R_{\downarrow}^{F1} \approx 0.29 \pm 0.08\Omega$, $R^{N} \approx 0.44\Omega$, $R_{\perp}^{F2} \approx 0.016\Omega$, and $R^{N'} \approx 0.6 \pm 0.2\Omega$.

CHAPTER 5

X-RAY IMAGING OF MAGNETIC NORMAL MODES DRIVEN BY SPIN TRANSFER TORQUE IN A MAGNETIC NANOPILLAR DEVICE

In this chapter, We will discuss imaging the magnetic dynamics driven by spin transfer torque in a nanopillar device using time-resolved x-ray microscopy. We apply a microwave current to exert an oscillating spin torque near the ferromagnetic resonance frequency of the free layer. This spin torque drives the magnetic dynamics, which is detected by x-ray pulses synchronized to the microwave signal. An analysis of the dynamics reveals different magnetic normal modes which vary as a function of microwave frequency and applied magnetic field. We are able to identify a spatially uniform mode and a non-uniform edge mode. The non-uniformity is affected by the Oersted field of the microwave current. We compare the imaging results with micromagnetic simulations and find good agreement.

5.1 Introduction

Spin transfer torque can drive current-controlled magnetization dynamics in a nanoscale magnetic device.[13–15] Understanding these dynamics is important for applications such as spin transfer torque magnetic random access memory (STT-MRAM) and frequency-tunable microwave oscillators.[35] Early analyses of spin-torque-driven magnetization dynamics assumed for simplicity that the moving magnetization behaves like a single domain as assumed in the Stoner-Wohlfarth model (Figure 5.1 (a)).[99, 107] However, recent experiments on RF excitation spectrum measurements [54, 57, 58, 61, 71, 72] show that non-uniform magnetic excitations at high frequencies exist even in nanoscale magnetic de-

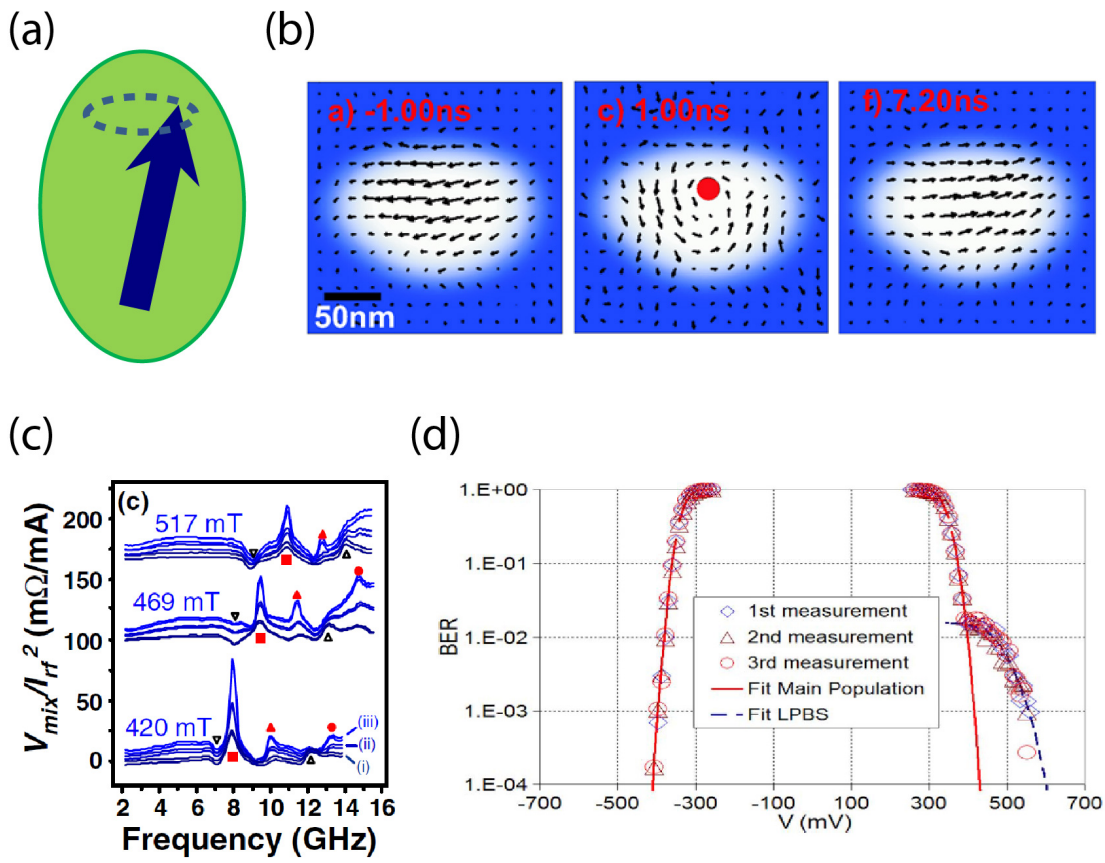

Figure 5.1: Nonuniform dynamics driven by spin torque in nanoscale magnetic devices. (a) Assumption of uniform magnetic dynamics. (b) DC-pulse-driven spin torque switching imaged by x-ray. Adapted from Reference [109]. (c) ST-FMR spectrum showing high frequency modes. Adapted from Reference [58]. (d) Bit error rate measurements of STT-MRAM devices. Adapted from Reference [108].

vices (Figure 5.1 (c)). The non-uniform magnetic dynamics can also complicate the switching behavior for the STT-MRAM application [108] by sometimes inducing abnormal bifurcated switching (Figure 5.1 (d)).

Direct imaging of the spatial structure of spin-torque-driven magnetic dynamics in nanoscale devices has been inaccessible until recently, when x-ray magnetic circular dichroism (XMCD) was used to provide magnetic contrast in soft x-ray microscopy to image spatial nonuniformities in magnetic switching

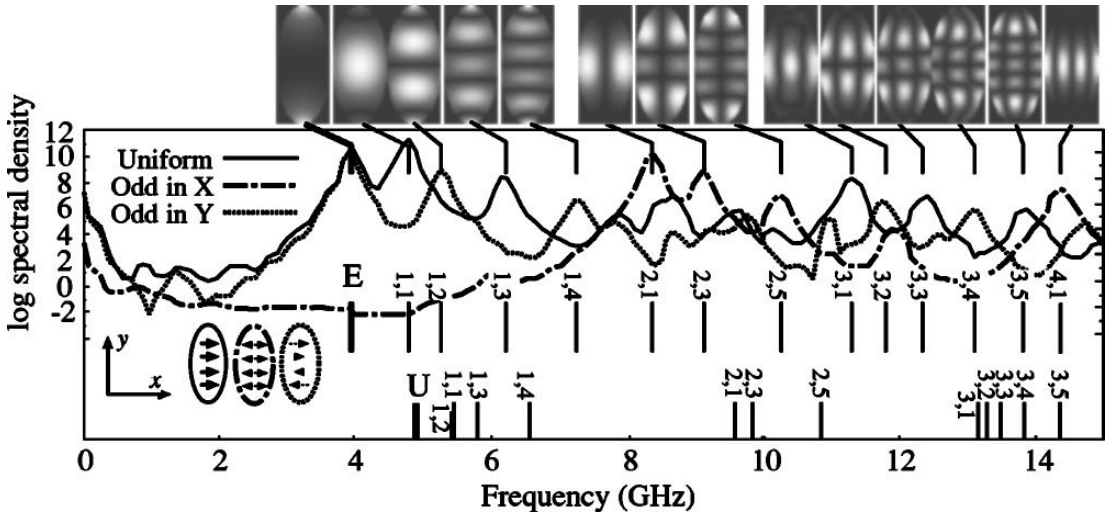

Figure 5.2: Magnetic normal modes and corresponding power spectra excited by external magnetic field. Adapted from Reference [115].

(Figure 5.1 (b)) [59, 109–111] and precession [112, 113] driven by large pulsed currents. However, to understand the fundamental dynamical modes that can be excited by spin torques, pulsed currents are rather complicated because they excite many normal modes simultaneously. In addition to that, switching and precession driven by pulsed currents are typically stochastic [114], while the imaging involves the averaging of multiple current-pulse-controlled traces. The stochastic features in the resulting images are washed out leaving only the repeating features.

The fundamental magnetic modes are called magnetic normal modes. Micromagnetic calculations [115] can predict magnetic normal models and give the spatial distribution of the oscillation amplitude (Figure 5.2). Magnetic normal modes with different symmetry can be excited using either RF magnetic field or RF current and detected by mechanical-FMR measurement.[52] Direct imaging of the magnetic normal modes that are excited by spin torque in nanoscale devices should be able to measure spatially resolved magnetic dynamics and

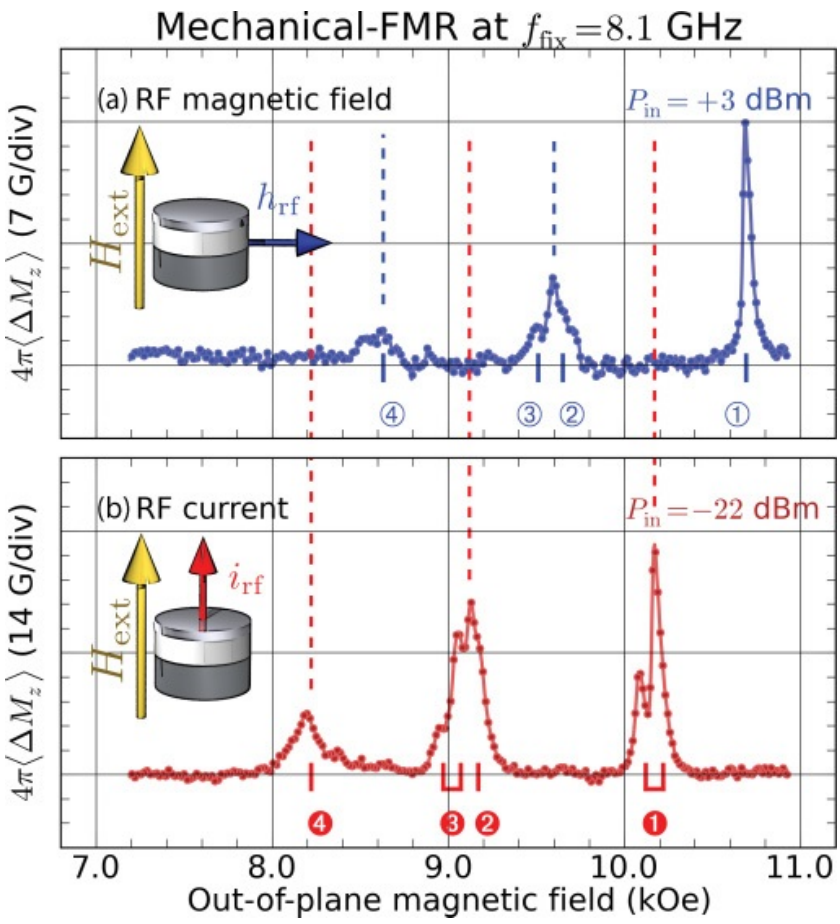

Figure 5.3: Magnetic normal modes with different symmetries. (a) Excited by a uniform in-plane RF magnetic field. (b) Excited by an RF current flowing perpendicularly through the device. Adapted from Reference [52].

differentiate different normal modes.

In order to image magnetic normal modes drive by spin torque, we apply a continuous microwave current to exert an oscillating spin torque near the magnetic resonance frequencies of different device modes [54, 58, 71, 72]. This spin torque excites individual magnetic normal modes selectively, which are then imaged by x-ray pulses synchronized to the microwave current. Similar to magnetic-field-driven ferromagnetic resonance [116], ST-FMR is periodic and repeatable, so that our images still capture the main features of the dynamics

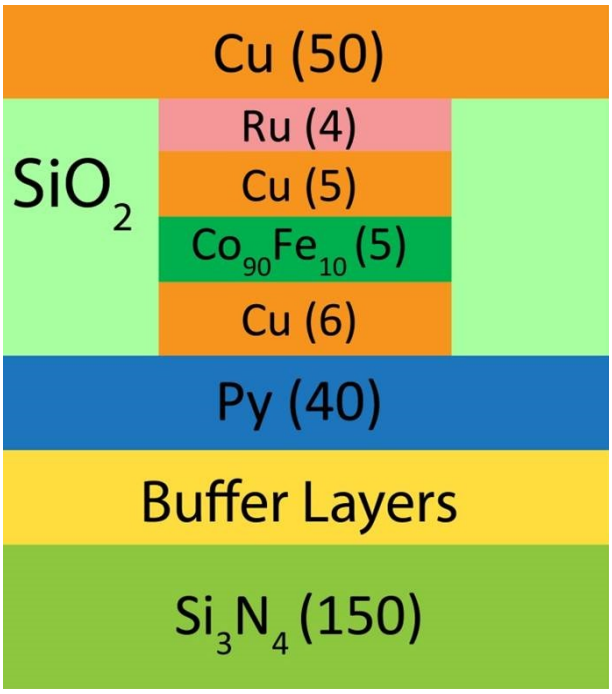

Figure 5.4: Device structure for imaging magnetic normal modes.

even with multiple averages.

5.2 Device Fabrication

We fabricated the nanopillar devices (Figure 5.4) on a Si substrate coated with 150 nm of low stress (film tension < 200 MPa) silicon nitride film on both sides. The devices have a spin valve structure with the following layers (in nm): $\{\text{Ta(3)/CuN(20)}\}_2$/Ta(3)/Cu(2)/Py(40)/Cu(6)/$\text{Co}_{90}\text{Fe}_{10}$(5)/Cu(4)/Ru(4), where $\text{Co}_{90}\text{Fe}_{10}$ and Py serve as the free layer and the fixed layer respectively. The multilayer film was deposited in a DC magnetron sputtering system with a base pressure below 10^{-8} Torr. An elliptical shape of 100×250 nm^2 was defined by e-beam lithography and then etched in an Ar ion mill with an end-point de-

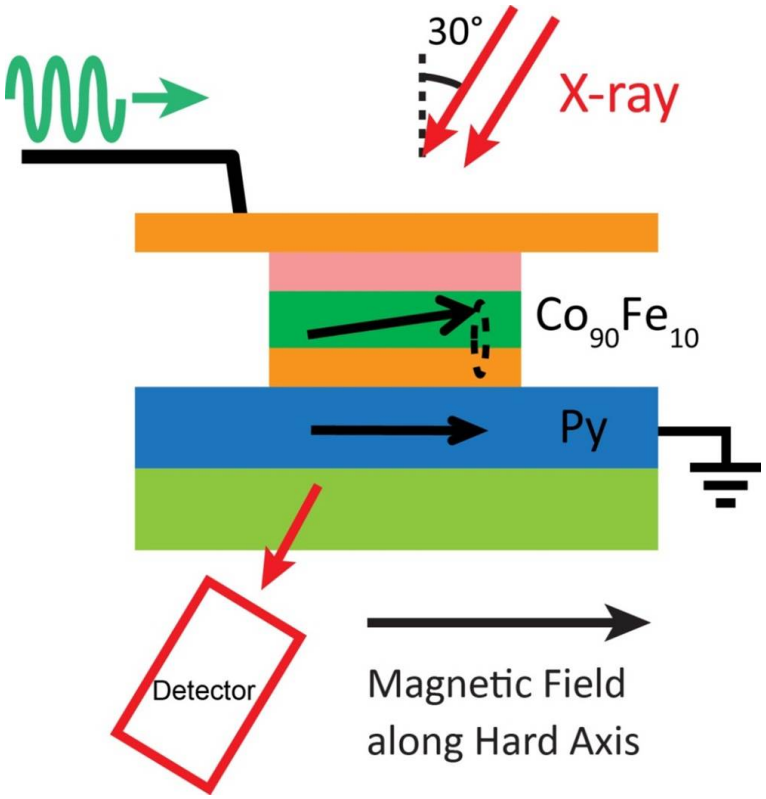

Figure 5.5: Measurement diagram of the x-ray imaging of magnetic normal modes.

tector. The etching was stopped aiming at the Py/Cu interface thus leaving the fixed layer extended with the polarizer defined right underneath the free layer. A 50 nm layer of Cu was deposited to make the top contact to the device. To form the suspended nitride membrane, the Si substrate is etched anisotropically in heated KOH solution (25% at 85 °C), using RIE-patterned silicon nitride on the back side of the substrate as the etch mask.

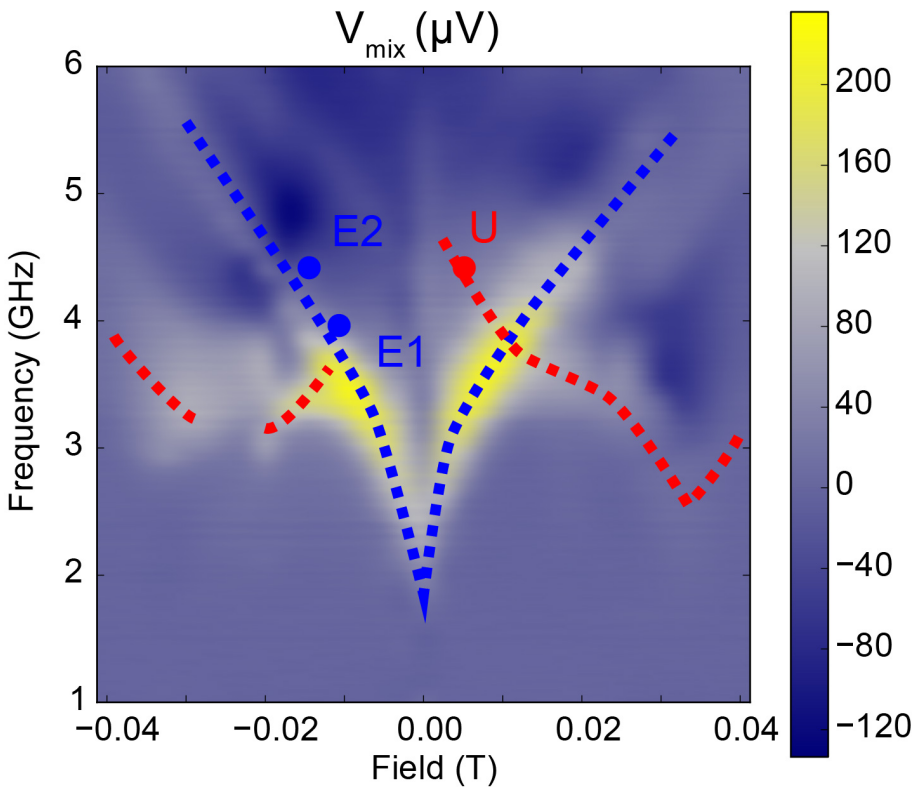

Figure 5.6: ST-FMR measurements with changing microwave frequency and magnetic field to identify different normal modes.

5.3 Methods

We excited the magnetic dynamics using current-induced ST-FMR with an in-plane external magnetic field applied along the hard axis of the elliptical sample (see Figure 5.5). Before the x-ray imaging, the ST-FMR mixing voltage was measured as a function of changing microwave frequency and magnetic field. The measurement results for a device we studied are shown in Figure 5.6. We can see two branches of peaks labeled by the blue and red dotted lines. We then used Scanning Transmission X-ray Microscopy (STXM) to image those different magnetic modes.

We measured the polarization-dependent changes in x-ray absorption on the

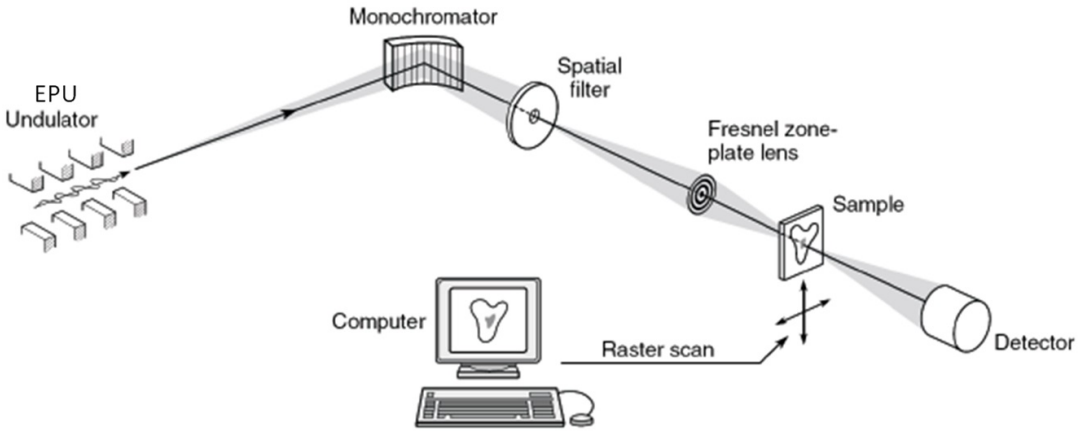

Figure 5.7: Schematic layout of the STXM endstation.

STXM endstation at the Advanced Light Source (Figure 5.7). The x-ray pulses have a pulse width of 70 ps and a frequency of 500 MHz. We adjust the x-ray energy at the Co L_3 edge (778 eV). As shown in Figure 5.5, the sample is aligned with its normal at 30° relative to the incident x-ray, so that the in-plane orientated magnetization projects on the direction of the incident x-ray. Using XMCD, the magnetic contrast of the in-plane magnetization is imaged. The microscope uses a zone plate to focus the x-ray beam into a spot on the sample. The sample is moved in the sample plane during the imaging process to scan across the device area. The scan is controlled by an interferometer to give a precise movement. The spatial resolution on the sample is about 30 nm, and each pixel is 10×10 nm^2. The x-ray pulses were synchronized to the driving microwave current to produce a stroboscopic image using a phase-locked feedback circuit; hence we made a full use of the multi-bunch ultra-fast x-ray source. The x-ray pulse came in only at the desired phases of the dynamics, and we had a correspondence between the electron bunches in the synchrotron storage ring and the dynamical phases. We are able to image eight equally-spaced phase points within the precession period, and the interval between neighboring phases goes

down to 25 ps (at 5 GHz) with some convolution between phases due to the limitation of the pulse width.

5.4 Results

We imaged the magnetic dynamics with a driving microwave frequency from 2 to 5 GHz and an applied magnetic field from -250 to 250 Oe. Modes at higher frequencies require higher applied magnetic field, which will likely diminish the spin torque by decreasing the offset angle between the fixed and free layers and provide worse time resolved signal due to the convolution of phases within a single pulse. The contrast images in Figure 5.8 (a) were made by dividing the images taken at each phase with the average of all phases. The time dependence and spatial nonuniformity of the magnetic dynamics are evident.

For quantitative analysis, we Fourier transformed the time resolved images to get the spatially distributed amplitude and phase of the mode (see Figure 5.8 (b)). For the mode in Figure 5.8, the amplitude exhibits small variations over the device area while there are large and striking variations in phase, with the phase data separating the device into the upper right and lower left halves having opposite phase.

The magnetic normal modes can be better understood with micromagnetic simulations. We performed three-dimensional micromagnetic simulations using a finite element based simulation platform for spintronics, SpinFlow 3D. To simulate the experiment, the magnetic field is set to be along the hard axis with a 7° offset angle. The micromagnetic equilibrium state at a given external magnetic field is first calculated. Then the normal modes are calculated using a

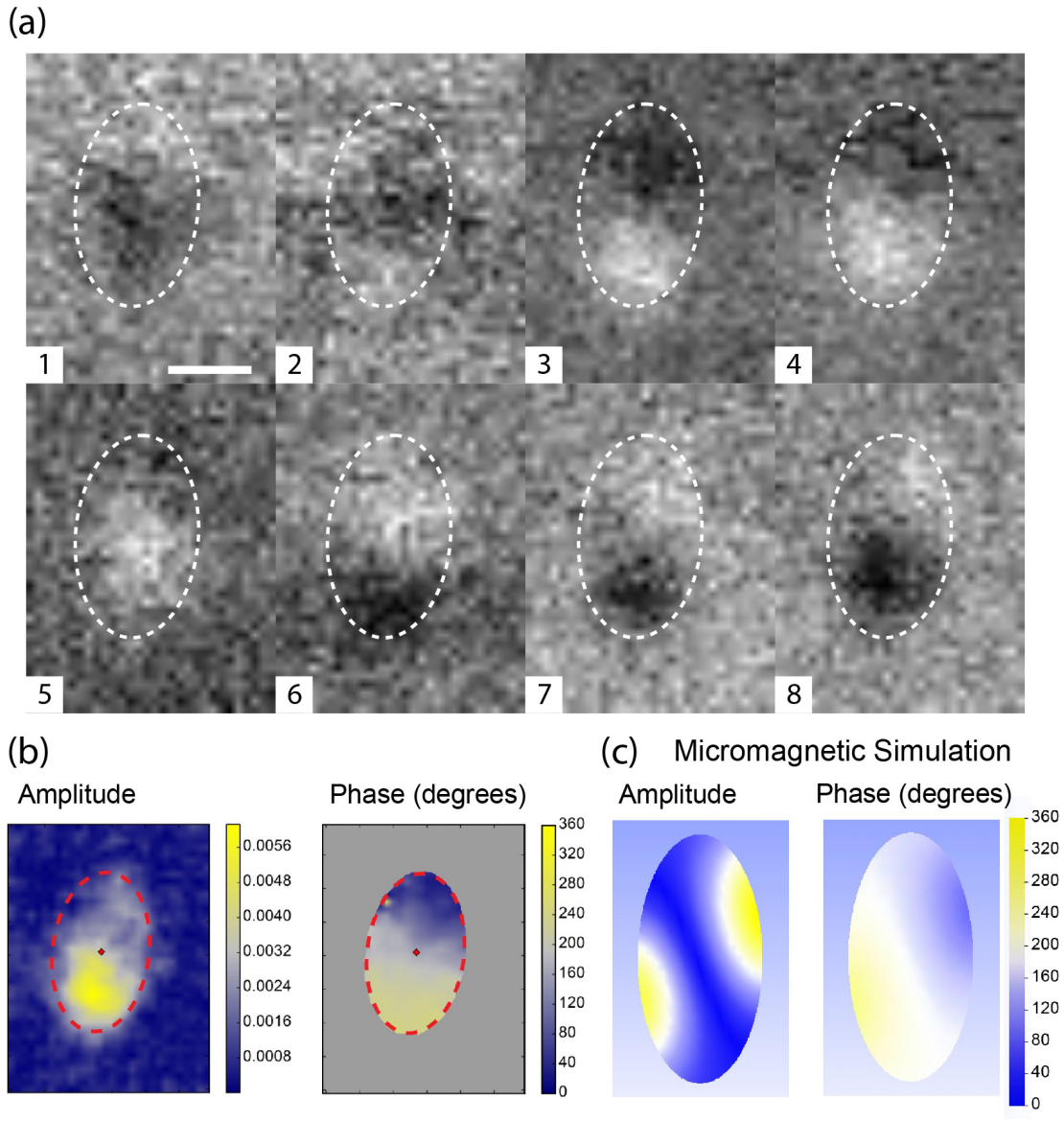

Figure 5.8: X-ray imaging of the E1 labeled in Figure 5.6. (a) Magnetic contrast images for the normal modes labeled as E1 in Figure 5.6. The eight panels correspond to eight phases equally spaced in precession period. (b) Amplitude and phase results by doing Fourier transform in the time domain for the images in (a). (C) Same type of results from micromagnetic simulation using SpinFlow 3D.

micromagnetic eigensolver. In our simulation, we only simulate the dynamics of the free layer and leave the extended fixed layer completely pinned. We set the free layer to have a cross section of $90 \times 180\ \mathrm{nm}^2$ and a thickness of 5 nm similar to the dimensions in the experiment, with magnetic properties appropriate for CoFe. We use a mesh size of 5 nm. We show the results from micromagnetic simulations using the SpinFlow 3D package. The phase distribution of the simulation corresponds very well with the experiment. The amplitude is not as symmetric as in the simulation, because the configuration during the imaging is the slightly off resonance, while the simulation is at resonance.

We imaged two more dots, E2 and U on the spectrum, and we plot out the amplitude and phase of both experiment and simulation for all three dots in Figure 5.9. Again the phase distribution agrees very well between the measurement and the simulation. Dot U has a uniform distributed phase, and E2 is divided into two halves in phase just as E1. The amplitude distribution of E2 shows large amplitude near the upper and lower edges, which agrees with the simulation. We conclude that U corresponds to a uniform mode, and E1 and E2 correspond to a nonuniform edge mode.

5.5 Discussion

To understand the existence of the two kinds of normal modes, we consider a small portion of the free layer. Its magnetic dynamics can be described using the Landau-Lifshitz-Gilbert-Slonczewski equation of motion locally

$$\frac{d\hat{m}}{dt} = -\gamma \hat{m} \times \vec{H}_{\mathrm{eff}} + \alpha \hat{m} \times \frac{d\hat{m}}{dt} + \gamma \frac{\tau(I,\theta)}{M_S Vol} \hat{m} \times \frac{\hat{m} \times \hat{M}}{|\hat{m} \times \hat{M}|}. \tag{5.1}$$

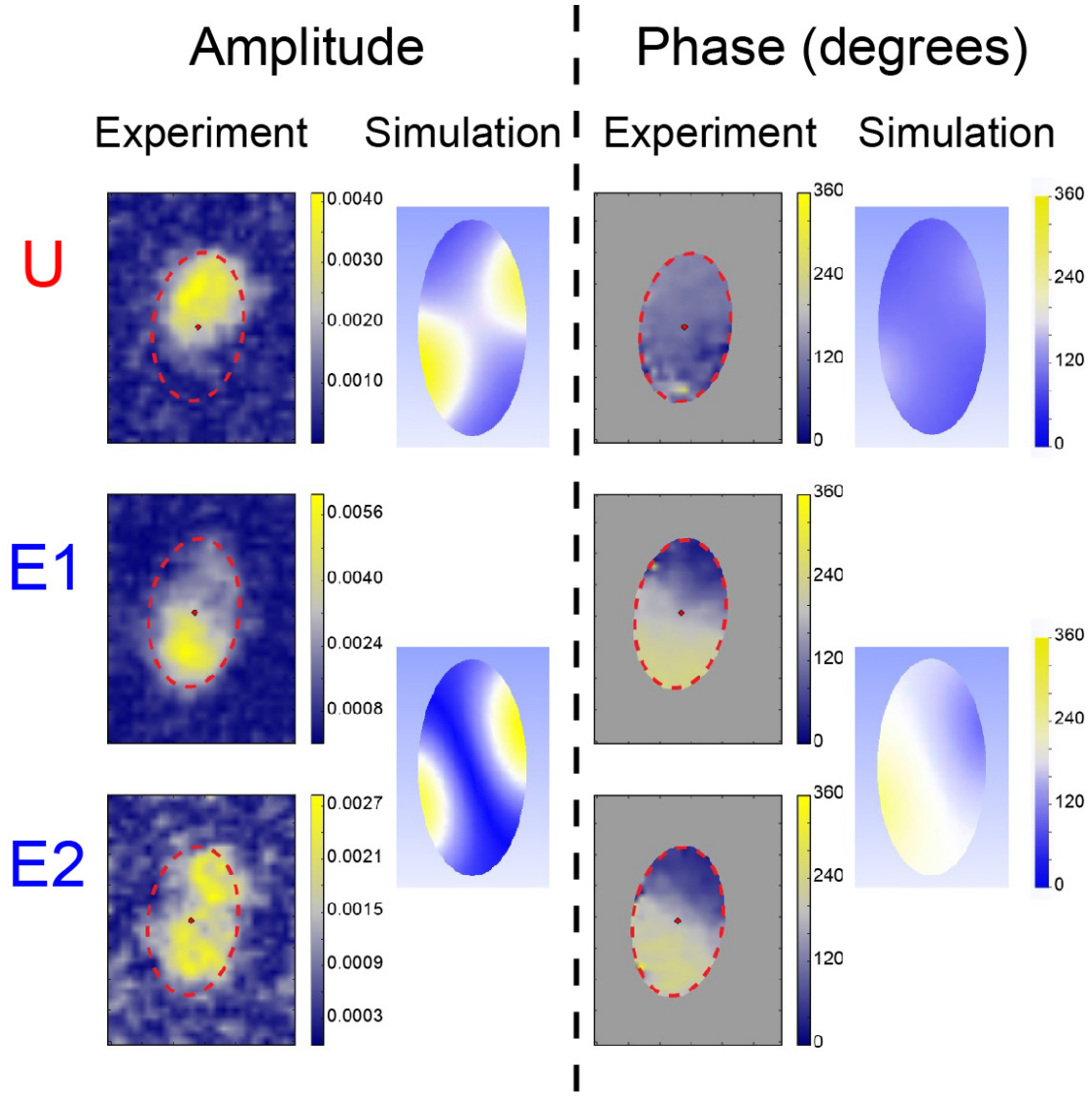

Figure 5.9: Amplitude and phase results of the all the normal modes labeled in Figure 5.6.

Here m and M are the local magnetization of the free layer and fixed layer; $\vec{H}_{\text{eff}}$ is the local effective field including the applied, Oersted, demagnetization, and exchange fields; α is the Gilbert damping parameter; $M_S Vol$ is the local moment; $\tau(I,\theta)$ is the spin torque that lies in the sample plane; I is the current flowing through the small portion of the sample; and γ is the absolute value of the gyromagnetic ratio. The uniform mode is preferred by the spin torque [99]. The

non-uniform mode here is evidently dividing the device into upper and lower halves with opposite phase. The dipole field from the fixed layer often leads to spatial non-uniformity of the free layer [89, 117]; however, the fixed layer of our device is left extended so that the dipole field from the fixed layer is kept small. We were applying a large microwave current through the device, and the microwave current can apply a significant Oersted field on the device. On the upper and lower halves, the Oersted field has opposite signs hence produces opposite torques that lead to opposite signs of contrast.

The micromagnetic simulation also helps understand the evolution of the modes. In Figure 5.10, the resonance frequency of each mode is shown as a function of external magnetic field for positive field values. Three different normal modes are identified from the simulation shown with their amplitude and phase distribution. According to the amplitude and phase information, the red line corresponds to a uniform mode with in-phase precession across the whole device, the blue line corresponds to an edge mode with out-of-phase precession of the two edges, and the black line corresponds to a more complex non-uniform mode. At high field, the frequencies of the modes all increase monotonically with field. At low field, the frequencies of the first two modes show dips as a function of field due to the dipole field from the unsaturated free layer, and different modes cross over. The simulation agrees well with the ST-FMR spectrum except the dip of the blue line positioned at a nonzero field. This is likely due to the dipole field from the finite size fixed layer in the simulation. For negative field values, the simulation shows the same results with an opposite symmetry.

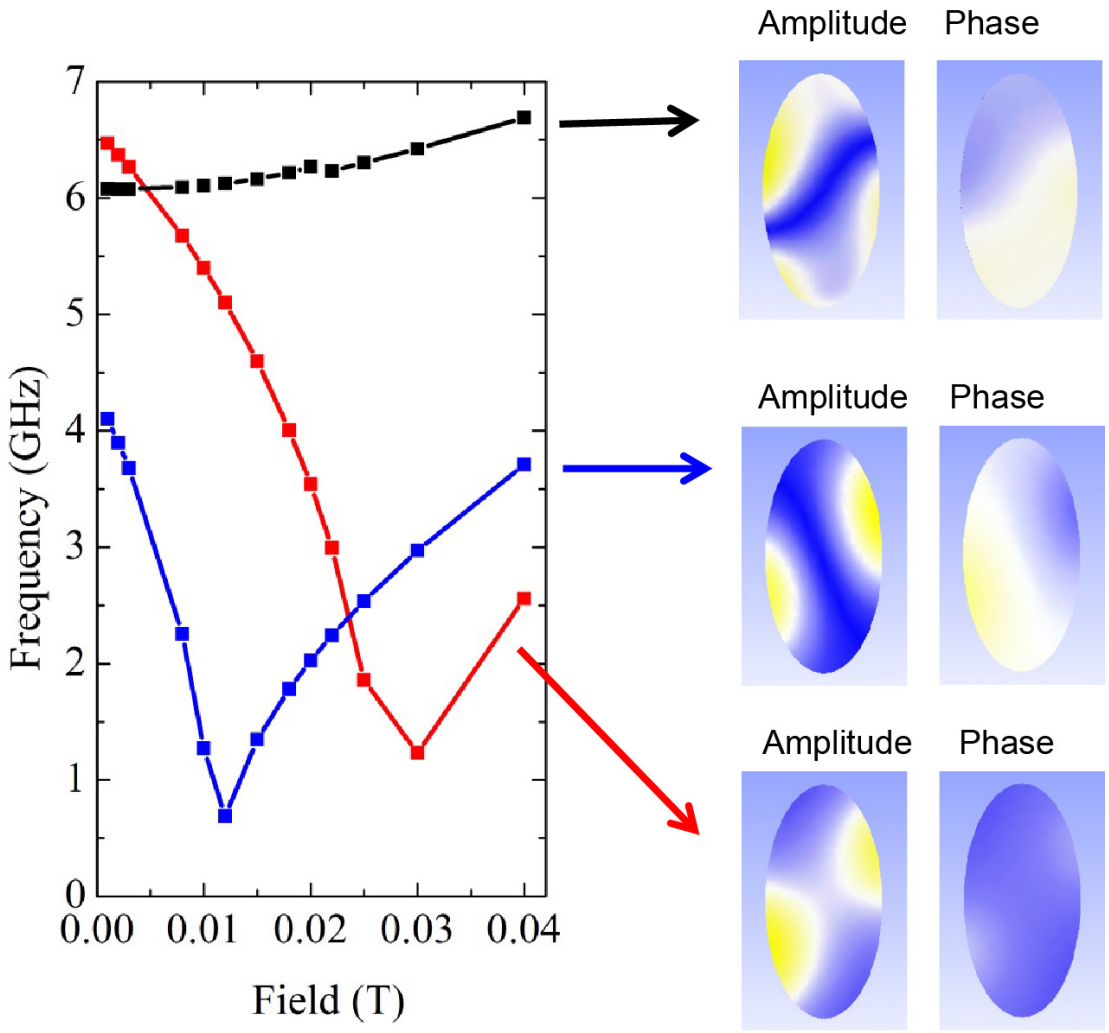

Figure 5.10: Evolution of the normal modes calculated by micromagnetic simulations.

5.6 Summary

We performed x-ray imaging of spin-torque-driven magnetic dynamics in a nanopillar device, and we identified different magnetic normal modes in a spin torque device that have different structures in amplitude and phase. Our results from the time-resolved x-ray microscopy, ST-FMR spectrum measurement, and

micromagnetic simulation are qualitatively consistent with each other. We are working toward a quantitative comparison between the experimental amplitude/phase results and the micromagnetic simulations. Our results are important in understanding the fundamental physics in spin torque devices and in developing applications related to spin torque dynamics.

CHAPTER 6

SPIN TORQUE SWITCHING IN GaMnAs MAGNETIC TUNNEL JUNCTIONS

6.1 Introduction

Spin torque driven magnetic switching has attracted substantial interest for applications such as MRAM. The efficiency of spin torque switching is inversely proportional to the saturation magnetization of the free layer.[99] GaMnAs has diluted saturation magnetization.[118] For spin torque switching, it needs only 1/100 of the current density as needed for a metal device [119]. Since GaMnAs is a ferromagnetic semiconductor, it also provides a way to integrate spin torque device into a semiconductor circuit.

In GaMnAs, Mn ions substitute for Ga ions in the GaAs lattice. The concentration of Mn is around 5%. A Mn dopant has a Mn^{2+} valence state with a half-filled d-shell having spin 5/2. Each Mn dopant acts as an acceptor to localize a valence band hole. The valence band hole near each Mn dopant tends to have an opposite spin orientation to the Mn dopant, because of hybridization and level repulsion between orbitals of the same spin [118]. The valence band holes spread out and can interact with many Mn ions. If the holes have a high enough concentration, they can mediate effective interactions between most of the Mn moments, which induces ferromagnetism as shown in Figure 6.1. The Curie temperature of optimized samples can reach 170 K. Because the Mn moments have a low concentration, the saturation magnetization of GaMnAs is about 1/100 of conventional ferromagnetic metals.

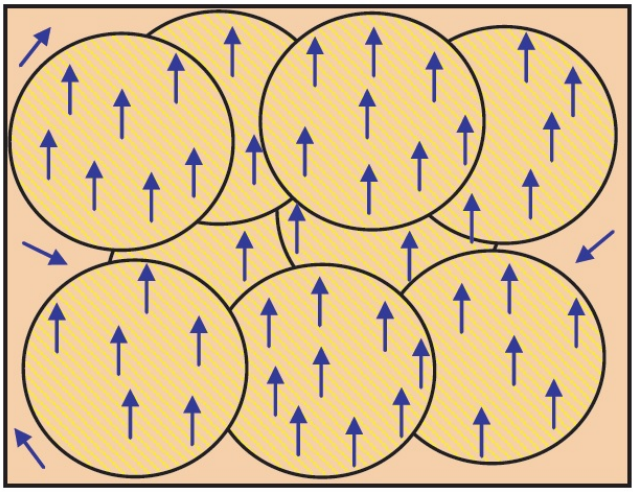

Figure 6.1: Carrier-induced ferromagnetism in GaMnAs. Adapted from Reference [118].

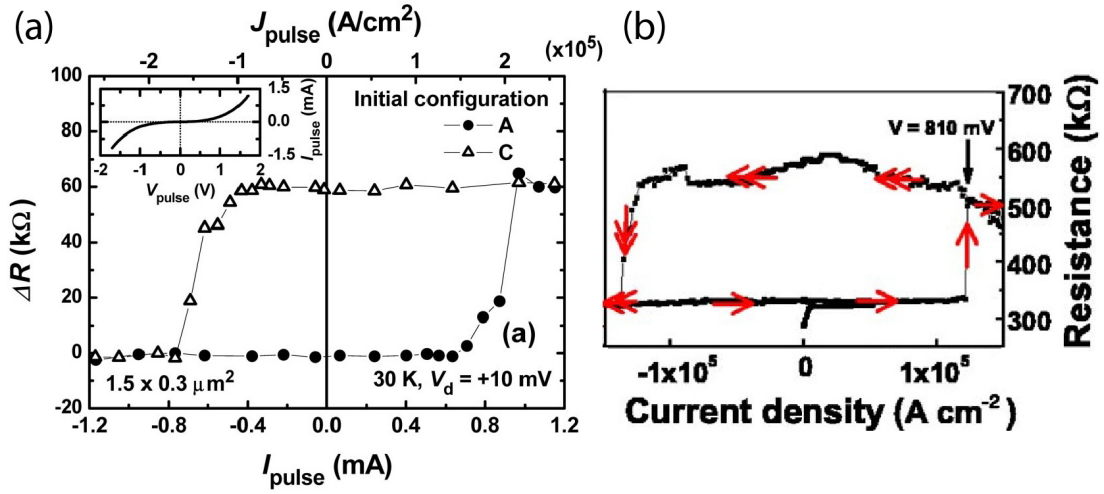

Figure 6.2: Current induced magnetic switching in GaMnAs devices. (a) Adapted from Reference [120]. (b) Adapted from Reference [121].

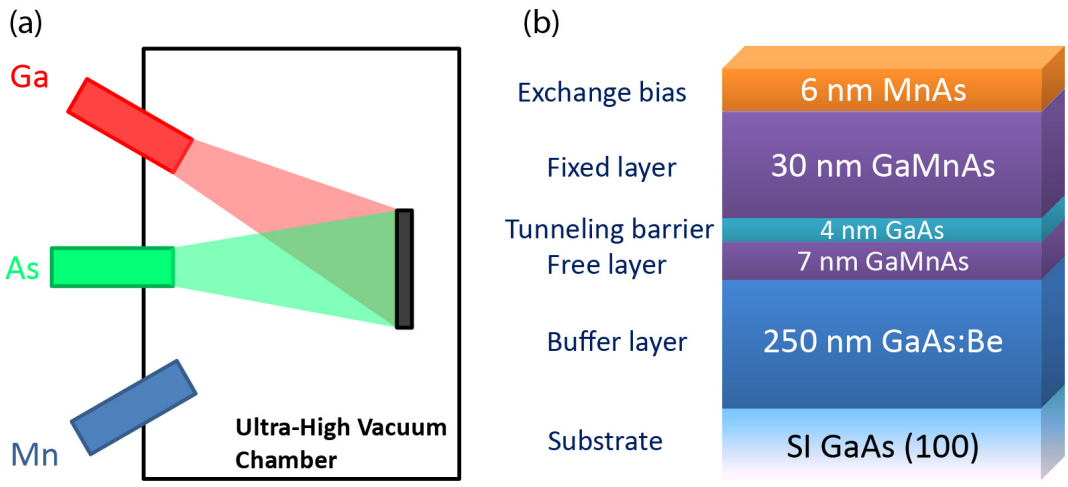

Figure 6.3: GaMnAs multilayers. (a) MBE growth of the multilayers. (b) Multilayers structure and functionality.

Spin torque switching has been demonstrated in previous works [120, 121]. However, the device resistances for these two works were about 300-400 kOhm, which means that Ohmic heating might have affected the switching. In our study, we worked on fabricating low resistance GaMnAs magnetic tunnel junctions and spin-valve samples in order to minimize the heating effect and study the switching purely by spin torque. The measurement of spin torque driven magnetic dynamics also enables us to study the magnetism related physics in GaMnAs.

6.2 Device Fabrication

The GaMnAs multilayers were grown in an ultra-high vacuum chamber with low-temperature molecular beam epitaxy at 250 °C (Figure 6.3)[122]. They had the layer structure (in nm): GaAs substrate/Be doped GaAs (250)/GaMnAs(7)/GaAs(4)/GaMnAs(30)/MnAs(6). The thick Be doped GaAs acts as a

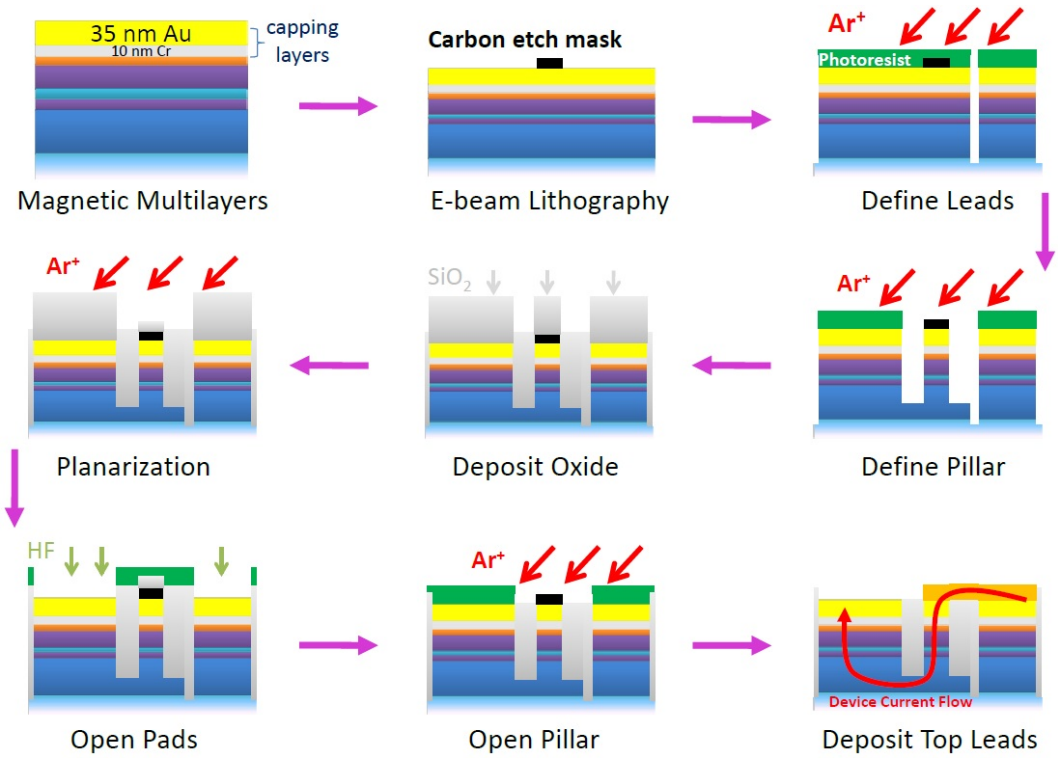

Figure 6.4: GaMnAs device fabrication process.

buffer layer. The thin and thick GaMnAs layers are the free layer and fixed layer respectively. The undoped GaAs layer is the tunnel barrier. It was grown much thinner in our devices than in previous works [120, 121] in order to make low RA devices. MnAs provides an exchange bias to the fixed layer. Since it is a metal, it also provides a good contact with top metal leads, which also helps to minimize the resistance-area product of the devices.

The nanofabrication procedure follows a nanopillar process developed previously at Cornell [123]. The MBE grown thin films are on small chips rather than whole wafers. For e-beam lithography and photolithography, chip carriers are used, and job files are written according to the size and shape of each chip. The fabrication has eight major steps starting from the magnetic multilayers bulk material as shown in Figure 6.4:

1. E-beam lithography. Define a 50 nm thick carbon pattern as etch mask for the nanopillar. The size of the pattern varies from 2×1 μm^2 to 500×250 nm^2.
2. Define leads. Use photolithography to define the bottom leads and contact pads. Then use ion milling to etch the multilayers into the substrate.
3. Define pillar. Use photolithography to cover the contact pads and expose the carbon mask. Then use low power ion mill to etch the nanopillar, stopping in the buffer layer. The ion mill process involves a small angle etch and a large angle side wall clean.
4. Deposit oxide. Use e-gun evaporated and plasma enhanced chemical vapor deposited SiO_2 to protect from oxidation and insulate the nanopillar.
5. Planarization. A large angle ion mill process to thin down the oxide above the pillar.
6. Open pads. Use HF or RIE to etch the oxide above the contact pads.
7. Open pillar. Use ion milling to etch the oxide above the carbon mask until it is exposed. The step involves repeating etch and oxide thickness measurements to ensure an accurate etch depth.
8. Deposit top leads. Use an oxygen plasma to remove the carbon above the nanopillar and deposit copper top leads. The red arrow in the final panel of Figure 6.4 shows the current direction in a finished device.

One of the crucial steps is the e-beam lithography. Since the GaMnAs multilayer is single crystal, the crystal anisotropy axes have to be considered. As shown in Figure 6.5 (a), the GaMnAs cubic easy axes are oriented with a 45° angle from the GaMnAs uniaxial easy axis and MnAs easy axis. Since the exchange bias from MnAs will pin the GaMnAs fixed layer along its uniaxial easy

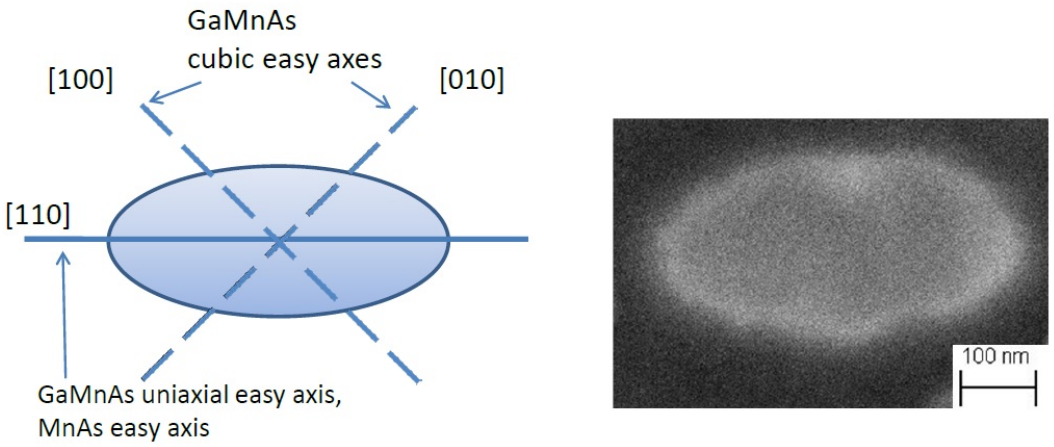

Figure 6.5: GaMnAs device cross section. (a) Orientation of the cross section with respect to GaMnAs multilayers crystal axis. (b) SEM image of the cross section before the "Open Pillar" step.

axis, the elliptical shape is defined to orient along that axis. The cubic crystal anisotropy will pin the magnetization near its local energy minimum that corresponds to steps in the field switching curves shown in the next section. Figure 6.5 (b) shows a SEM image of the cross section for a 500×250 nm^2 sample.

6.3 Electrical Measurement

To characterize the devices, we first measured the differential resistance while sweeping the magnetic field. All the electrical measurements were done in a cryogenic probe station at about 10 K with liquid helium cooling. Figure 6.6 shows the result from a device with a cross section of 1000×500 nm^2. In Figure 6.6 (a), the free layer switches at low field, while the fixed layer switches at a much higher field. The coercive fields of the fixed layer along positive and negative field directions differ for by 150 Oe, which is due to the exchange bias and dipole field from the MnAs layer. The exchange bias observed at the interface

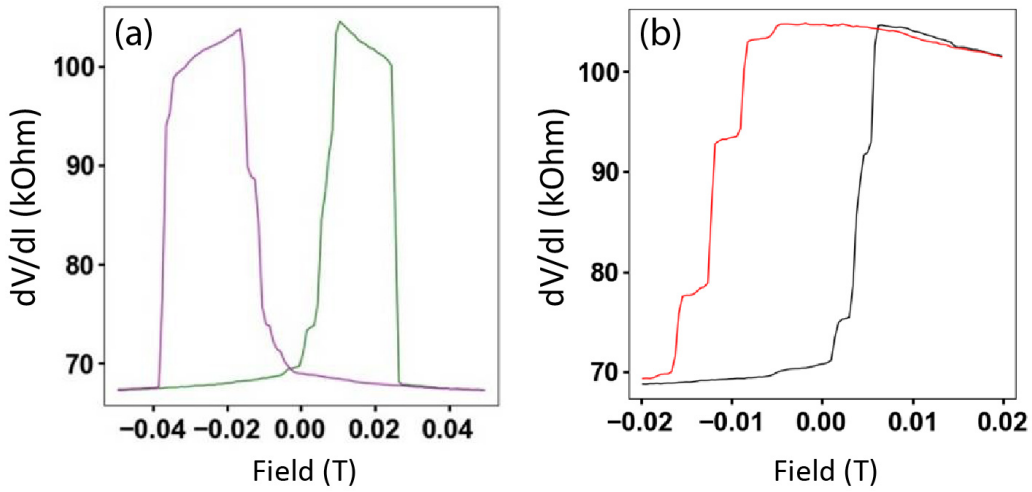

Figure 6.6: Field scan of the differential resistance for a GaMnAs device with a cross section of 1000×500 nm^2. (a) Major loop. (b) Minor loop.

of MnAs/GaMnAs here is weak compared with the IrMn based exchange bias in metal devices.[124] Figure 6.6 (b) is the minor loop measurement. It show clear steps in the free layer switching that corresponds to additional pinnings of the cubic crystal anisotropy. The minor loop is offset by -31 Oe due to the dipole from the fixed layer. The measurements shows a parallel resistance R_P = 68 Ω and TMR = 53%. Our devices therefore have a small RA product while still maintaining a large TMR ratio.

We did the current switching measurement next. The measurement is done by first setting the magnetization configuration by ramping the field then doing the current pulse scan. Each point is taken at zero bias after applying a current pulse. The scan is not a quasi-static scan. The positive current direction shown in Figure 6.7 (a) is from fixed layer to free layer favoring antiparallel configuration. The carriers in GaMnAs are holes, and the holes have opposite spins as of the Mn ions. The sign convention is consistent with hole-mediated ferromagnetism of GaMnAs.

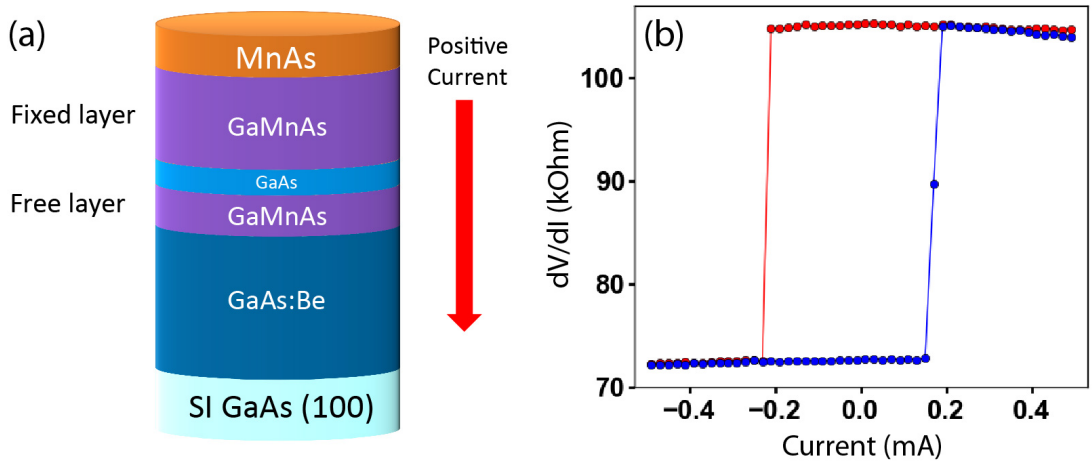

Figure 6.7: Current scan of the differential resistance for the GaMnAs device. (a) Direction of the positive current. (b) Current scan.

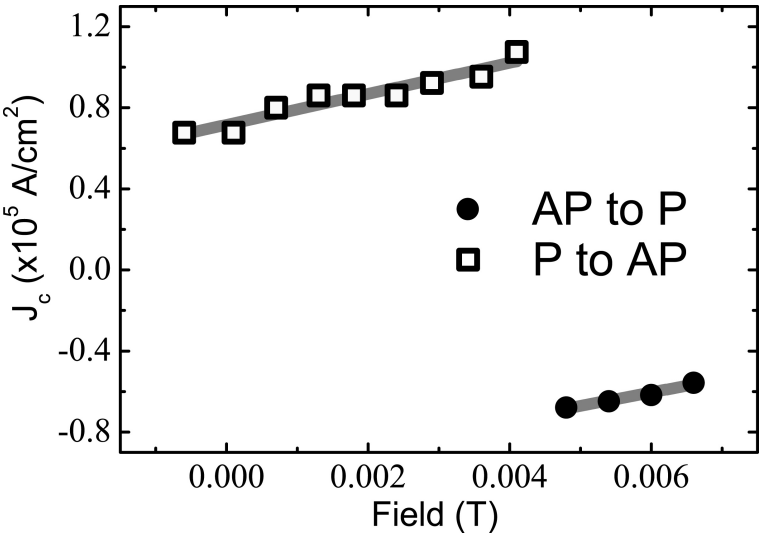

Figure 6.8: Measured partial switching phase diagram.

Figure 6.7 (b) shows a typical current scan of the 1000 × 500 nm^2 device shown in Figure 6.6 at -31 Oe. The critical current of magnetic switching can be read from the current scan, which is about 0.2 mA for this device. From the current scans, the critical current density can be calculated. It is in the 10^5 A/cm^2 range.

We did current scans at different applied field and mapped out the switching phase diagram. We show the switching phase diagram for a 500×250 nm^2 device in Figure 6.8. The squares corresponds to parallel to antiparallel switching, and the dots corresponds to antiparallel to parallel switching. We fit the lines and get the slope of the phase boundaries, Slope$^{\mathrm{APtoP}} = 6.6 \pm 0.9 \times 10^6$ AT^{-1}cm^{-2} and Slope$^{\mathrm{PtoAP}} = 7.6 \pm 0.9 \times 10^6$ AT^{-1}cm^{-2}, which is consistent with the results from Reference [120]. Our results on larger devices with a 1000×500 nm^2 cross section give similar critical current density values.

6.4 Summary

We fabricated GaMnAs MTJs with 10s of kΩ resistance and 50% TMR at 4.2 K. We observed spin torque switching with current density of 10^5 A/cm^2, which is 1/100 of a metal device that is consistent with the hole-mediated ferromagnetism in GaMnAs. Our measured critical current density is similar to Chiba et al.[120] and Elsen et al.[121].

For the future study, to get more quantitative results, ms- and ns-scale pulses can be used to measure spin torque switching. The ST-FMR technique can also be applied to quantitatively measure the spin torque in GaMnAs MTJs. However, with a large steady-state bias the MR becomes small [121], which is a challenge for measurements such as ST-FMR.

CHAPTER 7

CONCLUSION

I have discussed quantitative measurements of spin-torque-induced magnetic dynamics with different device structures. The measurements can provide information including properties of the device and the magnetic dynamics.

I have demonstrated a simple and easy way of using a network analyzer to characterize MTJ devices. The technique can provide information such as the strength of the spin torque and magnetic damping of the free layer. I also discussed the possibility of achieving microwave frequency gain in MTJ based devices. We found that gains larger than 1 can be achieved in 2-terminal MTJs, but the magnetic configuration and applied current are difficult to tune for a controllable amplification. Voltage gains above 100 might be achieved in optimized 3-terminal devices.

In the discussion of the measurement of the nonlocal spin torque, I showed the first quantitative measurement of the nonlocal torque at all biases. Our results agrees with pulse switching experiments at high bias and calculation from theory. Our analysis gives suggestions to optimise the nonlocal spin torque so that it can be as efficient as in a 2-terminal MTJ.

In the X-ray imaging of spin torque driven magnetic normal modes, we have identified and imaged different normal modes with different symmetries that depend on applied magnetic field and microwave frequency. They can be explained using micromagnetic simulations.

I also discussed our progress in fabricating and measuring ferromagnetic semiconductor spin torque devices. We have made low RA MTJs compared

with previous works and achieved magnetic switching using spin torque.

As the development of applications such as STT-MRAM leads to prototype products, the specialized characterization of individual devices becomes more and more important to understanding the device physics and overcoming technical obstacles. For example, a good measurement of the spin torque efficiency and magnetic damping is essential for developing small MTJs beyond the 20 nm node. The techniques developed in this dissertation will be very practical for such characterizations and also characterizations of new material and device structures involving spin torque. The techniques and results in the X-ray imaging chapter can also be very interesting for a better understanding of spin torque driven magnetic dynamics.

BIBLIOGRAPHY

[1] E. B. Myers, D. C. Ralph, J. A. Katine, R. N. Louie, and R. A. Buhrman. Current-induced switching of domains in magnetic multilayer devices. *Science*, 285(5429):867–870, August 1999.

[2] K. Ando, S. Takahashi, K. Harii, K. Sasage, J. Ieda, S. Maekawa, and E. Saitoh. Electric manipulation of spin relaxation using the spin hall effect. *Physical Review Letters*, 101(3):036601–4, July 2008.

[3] Haiming Yu, S. Granville, D. P. Yu, and J.-Ph. Ansermet. Evidence for thermal spin-transfer torque. *Physical Review Letters*, 104(14):146601, April 2010.

[4] M. N. Baibich, J. M. Broto, A. Fert, F. Nguyen Van Dau, F. Petroff, P. Etienne, G. Creuzet, A. Friederich, and J. Chazelas. Giant magnetoresistance of (001)Fe/(001)Cr magnetic superlattices. *Physical Review Letters*, 61(21):2472–2475, November 1988.

[5] G. Binasch, P. Grünberg, F. Saurenbach, and W. Zinn. Enhanced magnetoresistance in layered magnetic structures with antiferromagnetic interlayer exchange. *Physical Review B*, 39(7):4828–4830, March 1989.

[6] http://www.nobelprize.org/nobel_prizes/physics/laureates/2007/.

[7] M. Bowen, V. Cros, F. Petroff, A. Fert, C. Martínez Boubeta, J. L. Costa-Krämer, J. V. Anguita, A. Cebollada, F. Briones, J. M. de Teresa, L. Morellón, M. R. Ibarra, F. Güell, F. Peiró, and A. Cornet. Large magnetoresistance in Fe/MgO/FeCo(001) epitaxial tunnel junctions on GaAs(001). *Applied Physics Letters*, 79(11):1655–1657, September 2001.

[8] Shinji Yuasa, Taro Nagahama, Akio Fukushima, Yoshishige Suzuki, and Koji Ando. Giant room-temperature magnetoresistance in single-crystal Fe/MgO/Fe magnetic tunnel junctions. *Nature Materials*, 3(12):868–871, December 2004.

[9] Stuart S. P. Parkin, Christian Kaiser, Alex Panchula, Philip M. Rice, Brian Hughes, Mahesh Samant, and See-Hun Yang. Giant tunnelling magnetoresistance at room temperature with MgO (100) tunnel barriers. *Nature Materials*, 3(12):862–867, December 2004.

[10] http://en.wikipedia.org/w/index.php?title=Tunnel_magnetoresistance.

[11] T. Valet and A. Fert. Theory of the perpendicular magnetoresistance in magnetic multilayers. *Physical Review B*, 48(10):7099, 1993.

[12] M. Julliere. Tunneling between ferromagnetic films. *Physics Letters A*, 54(3):225–226, September 1975.

[13] J. C. Slonczewski. Current-driven excitation of magnetic multilayers. *Journal of Magnetism and Magnetic Materials*, 159(1-2):L1–L7, June 1996.

[14] L. Berger. Emission of spin waves by a magnetic multilayer traversed by a current. *Physical Review B*, 54(13):9353, October 1996.

[15] D.C. Ralph and M.D. Stiles. Spin transfer torques. *Journal of Magnetism and Magnetic Materials*, 320(7):1190–1216, April 2008.

[16] http://en.wikipedia.org/w/index.php?title=Demagnetizing_field.

[17] Sadamichi Maekawa. Magnetism: A flood of spin current. *Nature Materials*, 8(10):777–778, October 2009.

[18] Tomas Jungwirth, Jörg Wunderlich, and Kamil Olejník. Spin hall effect devices. *Nature Materials*, 11(5):382–390, April 2012.

[19] T. Tanaka, H. Kontani, M. Naito, T. Naito, D. S. Hirashima, K. Yamada, and J. Inoue. Intrinsic spin hall effect and orbital hall effect in 4d and 5d transition metals. *Physical Review B*, 77(16):165117, April 2008.

[20] Martin Gradhand, Dmitry V. Fedorov, Peter Zahn, and Ingrid Mertig. Extrinsic spin hall effect from first principles. *Physical Review Letters*, 104(18):186403, May 2010.

[21] Luqiao Liu, R. A Buhrman, and D. C Ralph. Review and analysis of measurements of the spin hall effect in platinum. *arXiv:1111.3702*, November 2011.

[22] Luqiao Liu, Chi-Feng Pai, Y. Li, H. W. Tseng, D. C. Ralph, and R. A. Buhrman. Spin-torque switching with the giant spin hall effect of tantalum. *Science*, 336(6081):555–558, May 2012.

[23] Chi-Feng Pai, Luqiao Liu, Y. Li, H. W. Tseng, D. C. Ralph, and R. A. Buhrman. Spin transfer torque devices utilizing the giant spin hall effect of tungsten. *Applied Physics Letters*, 101(12):122404–122404–4, September 2012.

[24] Y. Niimi, Y. Kawanishi, D. H. Wei, C. Deranlot, H. X. Yang, M. Chshiev, T. Valet, A. Fert, and Y. Otani. Giant spin hall effect induced by skew scattering from bismuth impurities inside thin film CuBi alloys. *Physical Review Letters*, 109(15):156602, October 2012.

[25] Luqiao Liu, Chi-Feng Pai, D. C. Ralph, and R. A. Buhrman. Magnetic

oscillations driven by the spin hall effect in 3-terminal magnetic tunnel junction devices. *Physical Review Letters*, 109(18):186602, October 2012.

[26] Wei-Gang Wang, Mingen Li, Stephen Hageman, and C. L. Chien. Electric-field-assisted switching in magnetic tunnel junctions. *Nature Materials*, 11(1):64–68, 2012.

[27] D. Chiba, M. Sawicki, Y. Nishitani, Y. Nakatani, F. Matsukura, and H. Ohno. Magnetization vector manipulation by electric fields. *Nature*, 455(7212):515–518, 2008.

[28] Manish K. Niranjan, Chun-Gang Duan, Sitaram S. Jaswal, and Evgeny Y. Tsymbal. Electric field effect on magnetization at the Fe/MgO(001) interface. *Applied Physics Letters*, 96(22):222504–222504–3, June 2010.

[29] Jian Zhu, J. A. Katine, Graham E. Rowlands, Yu-Jin Chen, Zheng Duan, Juan G. Alzate, Pramey Upadhyaya, Juergen Langer, Pedram Khalili Amiri, Kang L. Wang, and Ilya N. Krivorotov. Voltage-induced ferromagnetic resonance in magnetic tunnel junctions. *Physical Review Letters*, 108(19):197203, May 2012.

[30] S. Ikeda, K. Miura, H. Yamamoto, K. Mizunuma, H. D. Gan, M. Endo, S. Kanai, J. Hayakawa, F. Matsukura, and H. Ohno. A perpendicular-anisotropy CoFeBMgO magnetic tunnel junction. *Nature Materials*, 9(9):721–724, September 2010.

[31] A. Slachter, F. L. Bakker, J-P. Adam, and B. J. van Wees. Thermally driven spin injection from a ferromagnet into a non-magnetic metal. *Nat Phys*, 6(11):879–882, November 2010.

[32] J. Flipse, F. L. Bakker, A. Slachter, F. K. Dejene, and B. J. van Wees. Direct observation of the spin-dependent peltier effect. *Nature Nanotechnology*, 7(3):166–168, March 2012.

[33] Gerrit E. W. Bauer, Eiji Saitoh, and Bart J. van Wees. Spin caloritronics. *Nature Materials*, 11(5):391–399, April 2012.

[34] K. Uchida, S. Takahashi, K. Harii, J. Ieda, W. Koshibae, K. Ando, S. Maekawa, and E. Saitoh. Observation of the spin seebeck effect. *Nature*, 455(7214):778–781, October 2008.

[35] J.A. Katine and Eric E. Fullerton. Device implications of spin-transfer torques. *Journal of Magnetism and Magnetic Materials*, 320(7):1217–1226, April 2008.

[36] http://en.wikipedia.org/w/index.php?title=Magnetoresistive_random-access_memory.

[37] Johan Åkerman. Toward a universal memory. *Science*, 308(5721):508–510, April 2005.

[38] Yiming Huai. Spin-Transfer Torque MRAM (STT-MRAM): Challenges and prospects. *AAPPS Bulletin*, 18:33–40, December 2008.

[39] The International Technology Roadmap for Semiconductors. http://www.itrs.net/Links/2012ITRS/Home2012.htm.

[40] Jeong-Heon Park, Chando Park, Taehee Jeong, Matthew T. Moneck, Noel T. Nufer, and Jian-Gang Zhu. Co/Pt multilayer based magnetic tunnel junctions using perpendicular magnetic anisotropy. *Journal of Applied Physics*, 103(7):07A917–07A917–3, March 2008.

[41] Taiebeh Tahmasebi, Seidikkurippu N. Piramanayagam, Rachid Sbiaa, Hang Khume Tan, Randall Law, Sunny Lua, and Tow Chong Chong. Tailoring the growth of l10-FePt for spintronics applications. *Physica Status Solidi (RRL) Rapid Research Letters*, 5(12):426428, 2011.

[42] H. Liu, D. Bedau, D. Backes, J. A. Katine, and A. D. Kent. Precessional reversal in orthogonal spin transfer magnetic random access memory devices. *Applied Physics Letters*, 101(3):032403–032403–4, July 2012.

[43] J. Z. Sun, M. C. Gaidis, E. J. OSullivan, E. A. Joseph, G. Hu, D. W. Abraham, J. J. Nowak, P. L. Trouilloud, Yu Lu, S. L. Brown, D. C. Worledge, and W. J. Gallagher. A three-terminal spin-torque-driven magnetic switch. *Applied Physics Letters*, 95(8):083506, 2009.

[44] A. V. Khvalkovskiy, D. Apalkov, S. Watts, R. Chepulskii, R. S. Beach, A. Ong, X. Tang, A. Driskill-Smith, W. H. Butler, P. B. Visscher, D. Lottis, E. Chen, V. Nikitin, and M. Krounbi. Basic principles of STT-MRAM cell operation in memory arrays. *Journal of Physics D: Applied Physics*, 46(7):074001, February 2013.

[45] I. N. Krivorotov, N. C. Emley, J. C. Sankey, S. I. Kiselev, D. C. Ralph, and R. A. Buhrman. Time-domain measurements of nanomagnet dynamics driven by spin-transfer torques. *Science*, 307(5707):228–231, January 2005.

[46] S. I. Kiselev, J. C. Sankey, I. N. Krivorotov, N. C. Emley, R. J. Schoelkopf, R. A. Buhrman, and D. C. Ralph. Microwave oscillations of a nanomagnet driven by a spin-polarized current. *Nature*, 425(6956):380–383, 2003.

[47] Andrei Slavin. Microwave sources: Spin-torque oscillators get in phase. *Nat Nano*, 4(8):479–480, 2009.

[48] V. S. Pribiag, I. N. Krivorotov, G. D. Fuchs, P. M. Braganca, O. Ozatay, J. C. Sankey, D. C. Ralph, and R. A. Buhrman. Magnetic vortex oscillator driven by d.c. spin-polarized current. *Nat Phys*, 3(7):498–503, July 2007.

[49] A. Ruotolo, V. Cros, B. Georges, A. Dussaux, J. Grollier, C. Deranlot, R. Guillemet, K. Bouzehouane, S. Fusil, and A. Fert. Phase-locking of magnetic vortices mediated by antivortices. *Nature Nanotechnology*, 4(8):528–532, August 2009.

[50] Shehzaad Kaka, Matthew R. Pufall, William H. Rippard, Thomas J. Silva, Stephen E. Russek, and Jordan A. Katine. Mutual phase-locking of microwave spin torque nano-oscillators. *Nature*, 437(7057):389–392, 2005.

[51] P. M. Braganca, B. A. Gurney, B. A. Wilson, J. A. Katine, S. Maat, and J. R. Childress. Nanoscale magnetic field detection using a spin torque oscillator. *Nanotechnology*, 21(23):235202, June 2010.

[52] V. V. Naletov, G. de Loubens, G. Albuquerque, S. Borlenghi, V. Cros, G. Faini, J. Grollier, H. Hurdequint, N. Locatelli, B. Pigeau, A. N. Slavin, V. S. Tiberkevich, C. Ulysse, T. Valet, and O. Klein. Identification and selection rules of the spin-wave eigenmodes in a normally magnetized nanopillar. *Physical Review B*, 84(22):224423, December 2011.

[53] J. A. Katine, F. J. Albert, R. A. Buhrman, E. B. Myers, and D. C. Ralph. Current-driven magnetization reversal and spin-wave excitations in Co /Cu /Co pillars. *Physical Review Letters*, 84(14):3149, April 2000.

[54] A. A. Tulapurkar, Y. Suzuki, A. Fukushima, H. Kubota, H. Maehara, K. Tsunekawa, D. D. Djayaprawira, N. Watanabe, and S. Yuasa. Spin-

torque diode effect in magnetic tunnel junctions. *Nature*, 438(7066):339–342, November 2005.

[55] Chen Wang, Yong-Tao Cui, Jordan A. Katine, Robert A. Buhrman, and Daniel C. Ralph. Time-resolved measurement of spin-transfer-driven ferromagnetic resonance and spin torque in magnetic tunnel junctions. *Nature Physics*, 7(6):496–501, June 2011.

[56] Jun Hayakawa, Shoji Ikeda, Young Min Lee, Ryutaro Sasaki, Toshiyasu Meguro, Fumihiro Matsukura, Hiromasa Takahashi, and Hideo Ohno. Current-driven magnetization switching in CoFeB/MgO/CoFeB magnetic tunnel junctions. *Japanese Journal of Applied Physics*, 44:L1267–L1270, 2005.

[57] Alina M. Deac, Akio Fukushima, Hitoshi Kubota, Hiroki Maehara, Yoshishige Suzuki, Shinji Yuasa, Yoshinori Nagamine, Koji Tsunekawa, David D. Djayaprawira, and Naoki Watanabe. Bias-driven high-power microwave emission from MgO-based tunnel magnetoresistance devices. *Nat Phys*, 4(10):803–809, October 2008.

[58] J. C. Sankey, P. M. Braganca, A. G. F. Garcia, I. N. Krivorotov, R. A. Buhrman, and D. C. Ralph. Spin-transfer-driven ferromagnetic resonance of individual nanomagnets. *Physical Review Letters*, 96(22):227601–4, June 2006.

[59] Y. Acremann, J. P. Strachan, V. Chembrolu, S. D. Andrews, T. Tyliszczak, J. A. Katine, M. J. Carey, B. M. Clemens, H. C. Siegmann, and J. Stӧhr. Time-resolved imaging of spin transfer switching: Beyond the macrospin concept. *Physical Review Letters*, 96(21):217202, May 2006.

[60] G. S. D. Beach, C. Knutson, C. Nistor, M. Tsoi, and J. L. Erskine. Nonlinear domain-wall velocity enhancement by spin-polarized electric current. *Physical Review Letters*, 97(5):057203, August 2006.

[61] Lin Xue, Chen Wang, Yong-Tao Cui, J. A. Katine, R. A. Buhrman, and D. C. Ralph. Network analyzer measurements of spin transfer torques in magnetic tunnel junctions. *Applied Physics Letters*, 101(2):022417–022417–4, July 2012.

[62] Se-Chung Oh, Seung-Young Park, Aurelien Manchon, Mairbek Chshiev, Jae-Ho Han, Hyun-Woo Lee, Jang-Eun Lee, Kyung-Tae Nam, Younghun Jo, Yo-Chan Kong, Bernard Dieny, and Kyung-Jin Lee. Bias-voltage dependence of perpendicular spin-transfer torque in asymmetric MgO-based magnetic tunnel junctions. *Nat Phys*, 5(12):898–902, December 2009.

[63] S. Petit, C. Baraduc, C. Thirion, U. Ebels, Y. Liu, M. Li, P. Wang, and B. Dieny. Spin-torque influence on the high-frequency magnetization fluctuations in magnetic tunnel junctions. *Physical Review Letters*, 98(7):077203, February 2007.

[64] S. Petit, N. de Mestier, C. Baraduc, C. Thirion, Y. Liu, M. Li, P. Wang, and B. Dieny. Influence of spin-transfer torque on thermally activated ferromagnetic resonance excitations in magnetic tunnel junctions. *Physical Review B*, 78(18):184420, November 2008.

[65] M. H. Jung, S. Park, C.-Y. You, and S. Yuasa. Bias dependences of in-plane and out-of-plane spin-transfer torques in symmetric MgO-based magnetic tunnel junctions. *Physical Review B*, 81(13):134419, April 2010.

[66] O. G. Heinonen, S. W. Stokes, and J. Y. Yi. Perpendicular spin torque in magnetic tunnel junctions. *Physical Review Letters*, 105(6):066602, 2010.

[67] P. K. Muduli, O. G. Heinonen, and Johan Åkerman. Bias dependence of perpendicular spin torque and of free- and fixed-layer eigenmodes in MgO-based nanopillars. *Physical Review B*, 83(18):184410, May 2011.

[68] Z. Li, S. Zhang, Z. Diao, Y. Ding, X. Tang, D. M. Apalkov, Z. Yang, K. Kawabata, and Y. Huai. Perpendicular spin torques in magnetic tunnel junctions. *Physical Review Letters*, 100(24):246602, June 2008.

[69] T. Devolder, Joo-Von Kim, C. Chappert, J. Hayakawa, K. Ito, H. Takahashi, S. Ikeda, and H. Ohno. Direct measurement of current-induced fieldlike torque in magnetic tunnel junctions. *Journal of Applied Physics*, 105(11):113924–113924–5, June 2009.

[70] Seung-Young Park, Younghun Jo, and Kyung-Jin Lee. Measurement of perpendicular spin torque at high bias via the pulsed switching phase diagram. *Physical Review B*, 84(21):214417, December 2011.

[71] Jack C. Sankey, Yong-Tao Cui, Jonathan Z. Sun, John C. Slonczewski, Robert A. Buhrman, and Daniel C. Ralph. Measurement of the spin-transfer-torque vector in magnetic tunnel junctions. *Nat Phys*, 4(1):67–71, January 2008.

[72] Hitoshi Kubota, Akio Fukushima, Kay Yakushiji, Taro Nagahama, Shinji Yuasa, Koji Ando, Hiroki Maehara, Yoshinori Nagamine, Koji Tsunekawa, David D. Djayaprawira, Naoki Watanabe, and Yoshishige Suzuki. Quantitative measurement of voltage dependence of spin-transfer torque in MgO-based magnetic tunnel junctions. *Nat Phys*, 4(1):37–41, January 2008.

[73] C. Wang, Y.-T. Cui, J. Z. Sun, J. A. Katine, R. A. Buhrman, and D. C. Ralph. Bias and angular dependence of spin-transfer torque in magnetic tunnel junctions. *Physical Review B*, 79(22):224416, June 2009.

[74] Lin Xue, Chen Wang, Yong-Tao Cui, J. A. Katine, R. A. Buhrman, and D. C. Ralph. Conditions for microwave amplification due to spin-torque dynamics in magnetic tunnel junctions. *Applied Physics Letters*, 99(2):022505, 2011.

[75] D. Houssameddine, S. H. Florez, J. A. Katine, J.-P. Michel, U. Ebels, D. Mauri, O. Ozatay, B. Delaet, B. Viala, L. Folks, B. D. Terris, and M.-C. Cyrille. Spin transfer induced coherent microwave emission with large power from nanoscale MgO tunnel junctions. *Applied Physics Letters*, 93(2):022505–022505–3, July 2008.

[76] Charles Kittel. *Introduction to Solid State Physics*. Wiley, 2005.

[77] J.C. Slonczewski and J.Z. Sun. Theory of voltage-driven current and torque in magnetic tunnel junctions. *Journal of Magnetism and Magnetic Materials*, 310(2, Part 1):169–175, March 2007.

[78] J.M. Slaughter. Materials for magnetoresistive random access memory. *Annual Review of Materials Research*, 39(1):277–296, 2009.

[79] W. H. Rippard, M. R. Pufall, S. Kaka, S. E. Russek, and T. J. Silva. Direct-current induced dynamics in Co_{90}Fe_{10}/Ni_{80}Fe_{20} point contacts. *Physical Review Letters*, 92(2):027201, January 2004.

[80] D. Houssameddine, U. Ebels, B. Dieny, K. Garello, J.-P. Michel, B. Delaet, B. Viala, M.-C. Cyrille, J. A. Katine, and D. Mauri. Temporal coherence

of MgO based magnetic tunnel junction spin torque oscillators. *Physical Review Letters*, 102(25):257202, June 2009.

[81] M. R. Pufall, W. H. Rippard, S. Kaka, T. J. Silva, and S. E. Russek. Frequency modulation of spin-transfer oscillators. *Applied Physics Letters*, 86(8):082506–082506–3, February 2005.

[82] Benoit Georges, Julie Grollier, Akio Fukushima, Vincent Cros, Bruno Marcilhac, Denis-Gérard Crété, Hitoshi Kubota, Kay Yakushiji, Jean-Claude Mage, Albert Fert, Shinji Yuasa, and Koji Ando. Frequency converter based on nanoscale MgO magnetic tunnel junctions. *Applied Physics Express*, 2(12):123003, 2009.

[83] Shota Ishibashi, Takeshi Seki, Takayuki Nozaki, Hitoshi Kubota, Satoshi Yakata, Akio Fukushima, Shinji Yuasa, Hiroki Maehara, Koji Tsunekawa, David D. Djayaprawira, and Yoshishige Suzuki. Large diode sensitivity of CoFeB/MgO/CoFeB magnetic tunnel junctions. *Applied Physics Express*, 3:073001, June 2010.

[84] John Casimir Slonczewski. United states patent: 5695864 - electronic device using magnetic components, December 1997.

[85] Yoshishige Suzuki and Hitoshi Kubota. Spin-torque diode effect and its application. *Journal of the Physical Society of Japan*, 77:031002, 2008.

[86] Shinya Kasai, Kunihiro Nakano, Kouta Kondou, Norikazu Ohshima, Kensuke Kobayashi, and Teruo Ono. Three-terminal device based on the current-induced magnetic vortex dynamics with the magnetic tunnel junction. *Applied Physics Express*, 1:091302, 2008.

[87] T. Nozaki, H. Kubota, S. Yuasa, M. Shiraishi, T. Shinjo, and Y. Suzuki. rf amplification in a three-terminal magnetic tunnel junction with a magnetic vortex structure. *Applied Physics Letters*, 95(2):022513–3, July 2009.

[88] Samir Garzon, Richard A. Webb, Mark Covington, Shehzaad Kaka, and Thomas M. Crawford. Effect of resistance feedback on spin torque-induced switching of nanomagnets. *Journal of Magnetism and Magnetic Materials*, 321(19):3225–3230, October 2009.

[89] Luqiao Liu, Takahiro Moriyama, D. C. Ralph, and R. A. Buhrman. Reduction of the spin-torque critical current by partially canceling the free layer demagnetization field. *Applied Physics Letters*, 94(12):122508–3, March 2009.

[90] Xiao Cheng, Carl T. Boone, Jian Zhu, and Ilya N. Krivorotov. Nonadiabatic stochastic resonance of a nanomagnet excited by spin torque. *Physical Review Letters*, 105(4):047202, July 2010.

[91] Jiang Xiao, A. Zangwill, and M. D. Stiles. Macrospin models of spin transfer dynamics. *Physical Review B*, 72(1):014446, July 2005.

[92] Andrei Slavin and Vasil Tiberkevich. Nonlinear auto-oscillator theory of microwave generation by spin-polarized current. *IEEE Transactions on Magnetics*, 45(4):1875–1918, 2009.

[93] Lin Xue, Chen Wang, Yong-Tao Cui, Luqiao Liu, A. Swander, J. Z. Sun, R. A. Buhrman, and D. C. Ralph. Resonance measurement of nonlocal spin torque in a three-terminal magnetic device. *Physical Review Letters*, 108(14):147201, April 2012.

[94] Tao Yang, Takashi Kimura, and Yoshichika Otani. Giant spin-accumulation signal and pure spin-current-induced reversible magnetization switching. *Nat Phys*, 4(11):851–854, November 2008.

[95] T. Kimura, Y. Otani, and J. Hamrle. Switching magnetization of a nanoscale ferromagnetic particle using nonlocal spin injection. *Physical Review Letters*, 96(3):037201, January 2006.

[96] H. Zou, X. J. Wang, and Y. Ji. Nonlocal spin valves with thin co electrodes for spin-transfer. *Journal of Applied Physics*, 108(3):033905, 2010.

[97] Luqiao Liu, Takahiro Moriyama, D. C. Ralph, and R. A. Buhrman. Spin-torque ferromagnetic resonance induced by the spin hall effect. *Physical Review Letters*, 106(3):036601, January 2011.

[98] D. K. Schreiber, Y-S Choi, Yuzi Liu, Ann N. Chiaramonti, David N. Seidman, and A. K. Petford-Long. Enhanced magnetoresistance in naturally oxidized MgO-based magnetic tunnel junctions with ferromagnetic CoFe/CoFeB bilayers. *Applied Physics Letters*, 98(23):232506, 2011.

[99] J. Z. Sun. Spin-current interaction with a monodomain magnetic body: A model study. *Physical Review B*, 62(1):570, July 2000.

[100] Arne Brataas, Yu. V. Nazarov, and Gerrit E. W. Bauer. Finite-element theory of transport in ferromagnet-normal metal systems. *Physical Review Letters*, 84(11):2481, March 2000.

[101] F. J. Jedema, M. S. Nijboer, Filip, and B. J. van Wees. Spin injection and spin accumulation in all-metal mesoscopic spin valves. *Physical Review B*, 67(8):085319, February 2003.

[102] Yuan Xu, Ke Xia, and Zhongshui Ma. Spin transfer torques in the nonlocal lateral spin valve. *Nanotechnology*, 19(23):235404, June 2008.

[103] H. Yuasa, M. Yoshikawa, Y. Kamiguchi, K. Koi, H. Iwasaki, M. Takagishi, and M. Sahashi. Output enhancement of spin-valve giant magnetoresistance in current-perpendicular-to-plane geometry. *Journal of Applied Physics*, 92(5):2646–2650, September 2002.

[104] C. T. Boone, J. A. Katine, M. Carey, J. R. Childress, X. Cheng, and I. N. Krivorotov. Rapid domain wall motion in permalloy nanowires excited by a spin-polarized current applied perpendicular to the nanowire. *Physical Review Letters*, 104(9):097203, March 2010.

[105] C. Ahn, K.-H. Shin, R. Loloee, J. Bass, and W. P. Pratt. Current-perpendicular-to-plane spin transport properties of CoFe alloys: Spin diffusion length and scattering asymmetry. *Journal of Applied Physics*, 108:023908, 2010.

[106] T. Kimura, J. Hamrle, and Y. Otani. Estimation of spin-diffusion length from the magnitude of spin-current absorption: Multiterminal ferromagnetic/nonferromagnetic hybrid structures. *Physical Review B*, 72(1):014461, July 2005.

[107] E. C. Stoner and E. P. Wohlfarth. A mechanism of magnetic hysteresis in heterogeneous alloys. *Philosophical Transactions of the Royal Society of London. Series A, Mathematical and Physical Sciences*, 240(826):599–642, May 1948.

[108] Tai Min, Qiang Chen, R. Beach, G. Jan, Cheng Horng, W. Kula, T. Torng, R. Tong, T. Zhong, D. Tang, Pokang Wang, Mao-min Chen, J.Z. Sun, J.K.

Debrosse, D.C. Worledge, T.M. Maffitt, and W.J. Gallagher. A study of write margin of spin torque transfer magnetic random access memory technology. *IEEE Transactions on Magnetics*, 46(6):2322 –2327, June 2010.

[109] J. P. Strachan, V. Chembrolu, Y. Acremann, X. W. Yu, A. A. Tulapurkar, T. Tyliszczak, J. A. Katine, M. J. Carey, M. R. Scheinfein, H. C. Siegmann, and J. Stöhr. Direct observation of spin-torque driven magnetization reversal through nonuniform modes. *Physical Review Letters*, 100(24):247201, June 2008.

[110] Peter Fischer, Dong-Hyun Kim, Weilun Chao, J. Alexander Liddle, Erik H. Anderson, and David T. Attwood. Soft x-ray microscopy of nanomagnetism. *Materials Today*, 9(12):26–33, January 2006.

[111] David P. Bernstein, Björn Bräuer, Roopali Kukreja, Joachim Stöhr, Thomas Hauet, Julien Cucchiara, Stéphane Mangin, Jordan A. Katine, Tolek Tyliszczak, Kang W. Chou, and Yves Acremann. Nonuniform switching of the perpendicular magnetization in a spin-torque-driven magnetic nanopillar. *Physical Review B*, 83(18):180410, May 2011.

[112] Markus Bolte, Guido Meier, Benjamin Krger, Andr Drews, Ren Eiselt, Lars Bocklage, Stellan Bohlens, Tolek Tyliszczak, Arne Vansteenkiste, Bartel Van Waeyenberge, Kang Wei Chou, Aleksandar Puzic, and Hermann Stoll. Time-resolved x-ray microscopy of spin-torque-induced magnetic vortex gyration. *Physical Review Letters*, 100(17):176601, April 2008.

[113] X. W. Yu, V. S. Pribiag, Y. Acremann, A. A. Tulapurkar, T. Tyliszczak, K. W. Chou, B. Bruer, Z.-P. Li, O. J. Lee, P. G. Gowtham, D. C. Ralph, R. A. Buhrman, and J. Stöhr. Images of a spin-torque-driven magnetic nanooscillator. *Physical Review Letters*, 106(16):167202, April 2011.

[114] Y.-T. Cui, G. Finocchio, C. Wang, J. A. Katine, R. A. Buhrman, and D. C. Ralph. Single-shot time-domain studies of spin-torque-driven switching in magnetic tunnel junctions. *Physical Review Letters*, 104(9):097201, March 2010.

[115] R. D. McMichael and M. D. Stiles. Magnetic normal modes of nanoelements. *Journal of Applied Physics*, 97(10):10J901–10J901–3, May 2005.

[116] A. Vansteenkiste, K. W. Chou, M. Weigand, M. Curcic, V. Sackmann, H. Stoll, T. Tyliszczak, G. Woltersdorf, C. H. Back, G. Schtz, and B. Van Waeyenberge. X-ray imaging of the dynamic magnetic vortex core deformation. *Nature Physics*, 5(5):332–334, 2009.

[117] P. M. Braganca, O. Ozatay, A. G. F. Garcia, O. J. Lee, D. C. Ralph, and R. A. Buhrman. Enhancement in spin-torque efficiency by nonuniform spin current generated within a tapered nanopillar spin valve. *Physical Review B*, 77(14):144423–6, April 2008.

[118] A. H. MacDonald, P. Schiffer, and N. Samarth. Ferromagnetic semiconductors: moving beyond (Ga,Mn)As. *Nat Mater*, 4(3):195–202, March 2005.

[119] Solomon Assefa, J. Nowak, J. Z. Sun, E. OSullivan, S. Kanakasabapathy, W. J. Gallagher, Y. Nagamine, K. Tsunekawa, D. D. Djayaprawira, and N. Watanabe. Fabrication and characterization of MgO-based magnetic tunnel junctions for spin momentum transfer switching. *Journal of Applied Physics*, 102(6):063901–063901–4, September 2007.

[120] D. Chiba, Y. Sato, T. Kita, F. Matsukura, and H. Ohno. Current-driven magnetization reversal in a ferromagnetic semiconductor

(Ga,Mn)As/GaAs/(Ga,Mn)As tunnel junction. *Physical Review Letters*, 93(21):216602, November 2004.

[121] M. Elsen, O. Boulle, J.-M. George, H. Jaffrs, R. Mattana, V. Cros, A. Fert, A. Lemaitre, R. Giraud, and G. Faini. Spin transfer experiments on (Ga,Mn)As(In,Ga)As(Ga,Mn)As tunnel junctions. *Physical Review B*, 73(3):035303, January 2006.

[122] K. C. Ku, S. J. Potashnik, R. F. Wang, S. H. Chun, P. Schiffer, N. Samarth, M. J. Seong, A. Mascarenhas, E. Johnston-Halperin, R. C. Myers, A. C. Gossard, and D. D. Awschalom. Highly enhanced curie temperature in low-temperature annealed [Ga,Mn]As epilayers. *Applied Physics Letters*, 82(14):2302, 2003.

[123] Nathan Emley. Magnetic multilayer nanopillars for the study of current-induced reversal of a thin magnetic layer. *Ph.D. Dissertation, Cornell University*, 2005.

[124] J. Nogués, J. Sort, V. Langlais, V. Skumryev, S. Suriach, J.S. Muñoz, and M.D. Baró. Exchange bias in nanostructures. *Physics Reports*, 422(3):65–117, December 2005.